

University of Alberta

Signal processing techniques for radar based subsurface and through wall
imaging

by

Jorge Mario Morales

A thesis submitted to the Faculty of Graduate Studies and Research
in partial fulfillment of the requirements for the degree of

Master of Science
in
Biomedical Engineering

Department of Electrical and Computer Engineering

©Jorge Mario Morales
Fall 2012
Edmonton, Alberta

Permission is hereby granted to the University of Alberta Libraries to reproduce single copies of this thesis and to lend or sell such copies for private, scholarly or scientific research purposes only. Where the thesis is converted to, or otherwise made available in digital form, the University of Alberta will advise potential users of the thesis of these terms.

The author reserves all other publication and other rights in association with the copyright in the thesis and, except as herein before provided, neither the thesis nor any substantial portion thereof may be printed or otherwise reproduced in any material form whatsoever without the author's prior written permission.

Abstract

The ground penetrating radar (GPR) and through-wall radar detect and identify a target, by transmitting electromagnetic signals and processing the reflected signal. Migration had been a common method used in radar signal processing to obtain geophysical images and sketch the reflected data in the correct scattering position. In this thesis a study about different imaging and migration techniques, is performed. An improved radar migration imaging technique is then proposed by taking into account the effect of a two media environment in the signal velocity and signal path. The signal reflected coefficients are refocused on a possible target location or locations, ensuring a strong reflection in the presence of a target and a low reflection otherwise. The F-K migration is the baseline technique in our image generation. The F-K will migrate the focused data and obtain a 2-D matrix with the approximate scattering coefficients locations with respect to the depth. This focusing, windowing and F-K process are repeated several times along a grid, allowing us to reconstruct a sectional image which will be filtered using the filtering after backprojection process obtaining a deblurred reconstructed image.

Acknowledgements

I would like to thank Dr. Mrinal Mandal and Dr. Rambabu Karamundi for all their help and support throughout this research. I would like to thank my family and friends who helped me in many ways to bring this thesis to a successful completion. I would like to thank Adrian Tan and Kevin Chan for all their help and explanations during the thesis development. I want to thank COLFUTURO for all their financial support during my period of studies.

Table of Contents

Chapter 1	1
Introduction.....	1
1.1 Objective and Major Contributions.....	3
1.2 Organization of the Thesis	4
Chapter 2.....	5
Background Review	5
2.1 Radar History	5
2.2 Radar Principles	6
2.3 Wave Propagation Principles	7
2.4 Radar Image Formation.....	8
2.4.1 Signal Transmission and Acquisition.....	8
2.4.2 Vector Network Analyzer (VNA) S-parameters	11
2.4.3 Acquired Signal Pre-processing	17
2.4.4 Recorded Data Interpretation.....	21
2.4.4.1 VNA Data and Scattering Distance Relation.....	22
2.4.4.2 A-scan Signal Processing.....	26
2.4.4.3 B-Scan Imaging	39
2.4.5 GPR Depth Estimation	41
2.4.6 Migration Imaging.....	44
2.4.6.1 Basic Migration Principle	44
2.4.6.2 Wavefield Migration Description	45

2.4.6.3 Kirchhoff Migration.....	47
2.5 Ground Penetrating Radar Signal Processing	48
2.6 Backprojection Filtering.....	55
2.6.1 Image Filtering	56
2.6.2 Backprojection in Radar applications.....	57
2.7 Summary	59
Chapter 3.....	61
Proposed Modified F-K (MFK) focusing technique.....	61
3.1 Schematic of the focusing technique.....	62
3.2 Signal Focusing	63
3.3 Windowed Data Estimation	66
3.4 F-K migration.....	67
3.5 2-D Image Generation.....	74
3.6 Filtered backprojection.....	75
3.7 Summary	77
Chapter 4.....	79
Performance Evaluation.....	79
4.1 Experimental Set-up.....	79
4.1.1 Scenario 1	80
4.1.2 Scenario 2	82
4.2 Developed Software	83
4.3 Reconstructed Images	84
4.3.1 Image reconstruction process	85

4.3.1.1 Effect of Backprojection Filtering	87
4.4 Comparison of the MFK technique with other techniques	90
4.5 Evaluation of the Proposed Technique.....	96
4.6 Summary	96
Chapter 5.....	98
Conclusions and Future Work	98
References.....	100
Apendix A- Matlab Codes	104

List of Tables

Table 2.1:	Distance calculation for VNA obtained phases of a free space propagation	26
Table 2.2:	DFT index and DTFT frequency values in x direction.....	51
Table 4.1:	List of MATLAB codes	83
Table 4.2:	Elapsed time per code	96

List of Figures

Figure 2.1:	Radar transmitter and receiver (a) Monostatic Radar, (b) Bistatic Radar.....	6
Figure 2.2:	Ray refraction at the transition of two media.....	7
Figure 2.3:	(a) Transmitted signal, (b) Transmitted Step frequency, and (c) Received signal.....	9
Figure 2.4:	Transmitted (TX) and received (RX) signals for a two target scenario.....	10
Figure 2.5:	Schematic of a two-port network and the S-parameters.....	12
Figure 2.6:	Wave performance over a target [24]	13
Figure 2.7:	(a) Experimental set-up using a two-port VNA, (b) Target over a sand layer	13
Figure 2.8:	Variation of the magnitude of all S-parameters over transmitted frequency	15
Figure 2.9:	Phase variation of reflection coefficient over transmitted frequency_(a) S_{11} and S_{21} phase parameters, (b) S_{12} and S_{22} phase parameters.....	16
Figure 2.10:	Obtained reflection coefficients representation	16
Figure 2.11:	Signal pre-processing.....	17
Figure 2.12:	(a) Acquired S-parameter values, (b) Zero padding from $f=0$ to f_{start} .(c) Complex conjugate signal, (d) Reconstructed time domain signal.....	19
Figure 2.13:	Reconstructed impulse response function $\gamma(t)$ after Hermitian signal processing	21
Figure 2.14:	TX/RX position.....	22

Figure 2.15:	LTI system diagram	22
Figure 2.16:	Three scattering simulation results	24
Figure 2.17:	Free space propagation scenario	25
Figure 2.18:	Impulse response reconstruction.....	27
Figure 2.19:	Input data spectrum of open space signal and signal with target corresponding to locations 03 and 10 in Fig. 2.17.....	28
Figure 2.20:	Signal spectrum after Hermitian signal processing.	29
Figure 2.21:	Difference of VNA signals with target and without target	30
Figure 2.22:	Difference of VNA signals with target and without target scattering_with respect to distance	30
Figure 2.23:	VNA impulse signal processing.....	31
Figure 2.24:	Signal difference spectrum	32
Figure 2.25:	(a) The impulse response, (b) The magnitude response_of the designed bandpass filter and (c) Signal spectrum after BPF.....	33
Figure 2.26:	Signal after bandpass filter.....	34
Figure 2.27:	Demodulator (a) Cosine value, and (b) Sine value. (c) Signal after cosine and (d) Signal after sine.	35
Figure 2.28:	(a) The impulse response and (b) The magnitude response of the designed low pass filter	36
Figure 2.29:	(a) Signal after LPF (cosine), and (b) Signal after LPF (sine).....	37
Figure 2.30:	A-scan scattering images free space experiment (a) Data 1-12 antenna position, (b) Data 2-11 antenna position, (c) Data 3-10 antenna position, (d)	

	Data 4-9 antenna position, (e) Data 5-8 antenna position, and (f) Data antenna 6-7 position.....	39
Figure 2.31:	Unfocused B-scan image (obtained with schematic shown in Fig. 2.17)..	40
Figure 2.32:	Resampled B-scan image (obtained with schematic shown in Fig. 2.17) ..	41
Figure 2.33:	The imaging environment. x_n ($1 \leq n \leq N$) represents the TX/RX location. y_{min} and y_{max} are the minimum and maximum depth, respectively	43
Figure 2.34:	$r'z, x_1, fq$ spectrum post-windowing.....	43
Figure 2.35:	Wavefield extrapolation.....	45
Figure 2.36:	Kirchhoff scattering point scenario.....	48
Figure 2.37:	Existing SAR imaging technique.....	50
Figure 2.38:	Backprojection image reconstruction	55
Figure 2.39:	(a) Flat region showing a simple object. (b-e) Reconstruction using 1,2,3, and 4 backprojections 45° apart. (f) Blurred reconstruction with 32 backprojections 5.625° apart.	55
Figure 2.40:	(a) Radar to target distance scenario, (b) Radar to target distance as function of time	58
Figure 2.41:	Image reconstruction.....	58
Figure 3.1:	Schematic of the proposed Modified F-K (MFK) focusing technique .	62
Figure 3.2:	Two-media signal refraction point geometry.....	64
Figure 3.3:	Block schematic for F-K migration technique.....	67
Figure 3.4:	Matrix illustration of $\Pi pz, kx, fq$ with respect (ω, kx) , where $\omega q = 2\pi fq$	69

Figure 3.5:	(a) The space (kx, ky) with contours of ωqvm as given in Eq.3.7. (b) Mapping process from $(-kx_{max} + \Delta kx, \omega qvm)$ to $(-kx_{max} + \Delta kx, ky)$ [40].	70
Figure 3.6:	(a) Mapped data for $kymax$ and $kymax - 1$ in the (kx, ky) domain (b) Interpolated data for $kymax$ and $kymax - 1$ in the (kx, ky) domain.	71
Figure 3.7:	Image reconstruction before filtering.	75
Figure 3.8:	Filter frequency response	76
Figure 3.9:	Filter frequency response for different ΔM values (with $M = 550, N = 600$).	77
Figure 4.1:	Vivaldi antenna (a) side 1 and (b) side 2.	80
Figure 4.2:	Laboratory setup scenario 1.	81
Figure 4.3:	Target dimensions scenario 1 (a) Rectangle, (b) Pipe and (c) Letter A.	81
Figure 4.4:	Scenario 2 dimensions and target (bottle) location.	82
Figure 4.5:	Target dimension scenario 2.	82
Figure 4.6:	Collected data at $x = 3.6$ cm with $z = 13.5$ cm antenna location (a) Magnitude and (b) Phase.	85
Figure 4.7:	Focused data at $x = 3.6$ cm with $z = 13.5$ cm antenna location (a) Magnitude and (b) Phase.	86
Figure 4.8:	B-scan image for pipe scenario at $z = 13.5$ cm.	87
Figure 4.9:	(a) "Rectangular" object (b) "Pipe" object (c) "A" object and (d) "bottle" object.	88
Figure 4.10:	Rectangular object (a) before filtering, (b) after filtering. Filter value was set with $\Delta M=837, M=673$ and $N=837$.	88

Figure 4.11:	Pipe object (a) before filtering, (b) after filtering. Filter value was set with $\Delta M=450$, $M=673$ and $N=837$	88
Figure 4.12:	Object “A” (a) before filtering, (b) after filtering. Filter value was set with $\Delta M=850$, $M=673$ and $N=837$	89
Figure 4.13:	Object “bottle” (a) before filtering, (b) after filtering. Filter value was set with $\Delta M=107$, $M=406$ and $N=837$	89
Figure 4.14:	Object “pipe” reconstructed image (a) with $\Delta M=0$, (b) with $\Delta M=100$ and (c) with $\Delta M=300$. $M=406$ and $N=837$ for all the examples.	90
Figure 4.15:	(a) Original rectangle object. Rectangle image obtained using (b) F-K migration, (c) Kirchhoff migration, (d) Modified F-K focusing technique excluding the antenna length, (e) Modified F-K focusing technique including the antenna length. Filter value was set with $\Delta M=835$, $M=673$ and $N=837$	91
Figure 4.16:	(a) Original pipe object. Pipe image obtained using (b) F-K migration, (c) Kirchhoff migration, (d) Modified F-K focusing technique excluding the antenna length, (e) Modified F-K focusing technique including the antenna length. Filter value was set with $\Delta M=450$, $M=673$ and $N=837$	92
Figure 4.17:	(a) Original A object. “A” image obtained using (b) F-K migration, (c) Kirchhoff migration, (d) Modified F-K focusing technique excluding the antenna length, (e) Modified F-K focusing technique including the antenna length. Filter value was set with $\Delta M=850$, $M=673$ and $N=837$	94

Figure 4.18: (a) Original bottle object. Bottle image obtained using (b) F-K migration, (c) Kirchhoff migration, (d) Modified F-K focusing technique excluding the antenna length, (e) Modified F-K focusing technique including the antenna length. Filter value was set at $\Delta M=550$, $M=406$ and $N=837$ 95

List of Abbreviations

GPR- Ground penetrating radar

TWI- Through-wall imaging

TWR-Through-wall radar

UWB-Ultra wideband

SAR- Synthetic Aperture Radar

SLAR- Side looking airborne radar

EM- Electro magnetic

DUT- Device under test

VNA- Vector network analyzer

BPF- Band pass filter

LPF- Low pass filter

IFFT- Inverse fast Fourier transform

FFT- Fast Fourier transform

IFT- Inverse Fourier transform

F-K- Frequency wavenumber

MFK- Modified frequency wavenumber

List of Symbols

ϵ_r	- Dielectric constant of the material
v	- Wave speed
$\sqrt{\epsilon_r}$	- Approximation of the refraction index
n	- Refraction index of the material
$S_t(f_m, t)$	- Transmitted frequency modulated signal
f_m	- m-th frequency
Δf	- Step frequency
A	- Transmitted signal amplitude
A_p	- Reflected signal amplitude from target p
t	- Time
L_n	- Monostatic antenna at n-th position
$\tau_{n,p}$	- Round trip propagation delay between the n-th TX/RX location (L_n) and a target p
$E_{p_k}(f_m)$	- Reflected signal from target p_k at f_m
P	- Number of targets in the scenario
$I(L_n, f_m)$	- Received signal at L_n for f_m
$[f_{start}, f_{end}]$	- Frequency bandwidth
Γ	- Reflection coefficient
$ \Gamma $	- Magnitude of the reflection coefficient
$\angle\Gamma$	- Phase of the reflection coefficient
V_R	- Reflected voltage
V_{INC}	- Incident voltage

$r(L_n, f_m)$	- Reflection coefficient at L_n for f_m
$\gamma(t)$	- Impulse response of the channel
Δt	- Time resolution
$\gamma_s(t)$	- Impulse response of the transmitted signal
$\gamma_{at}(t)$	- Impulse response of the transmitter
$\gamma_{ar}(t)$	- Impulse response of the receiver
$\gamma_c(t)$	- Antenna cross coupling response
$\gamma_{mt}(t)$	- Transmitted medium response
$\gamma_{mr}(t)$	- Reflected medium response
$\gamma_t(t)$	- Target impulse response
$n(t)$	- Noise
$X(e^{j\omega})$	- Input of an LTI system
$H(e^{j\omega})$	- Frequency response of an LTI system
$Y(e^{j\omega})$	- Output of the LTI system
c	- Speed of light
d	- One-way target distance from the measurement point
$\Gamma_{wt}^H(f)$	- Zero padded and complex conjugated data with target
$\Gamma_{wot}^H(f)$	- Zero padded and complex conjugated data without target
$\gamma_{wt}(t)$	- Impulse response of the system with target
$\gamma_{wot}(t)$	- Impulse response of the system without target
$\gamma_d(t)$	- Difference of $\gamma_{wt} - \gamma_{wot}$
$\gamma_{bpf}(t)$	- Impulse response after band pass filter
f_c	- Center frequency of the bandpass filter
y_{min}	- Minimum target depth

y_{max}	- Maximum target depth
Δy	- Depth resolution
y	- Depth vector
x_n	- Antenna position number along the B-scan
$r(z, x_n, f_m)$	- Collected B- scan data assuming a fixed z , at N different antenna locations and at M different frequencies.
$M(x, y)$	- Reflectivity
$P(x, y, t)$	- Wavefield
k_x	- Horizontal wavenumber
k_y	- Vertical wavenumber
Δk_x	- Horizontal wavenumber resolution
ω	- Angular frequency
λ	- Wavelength
λ_x	- Wavelength along horizontal axis
$\psi(r', t')$	- Scalar wavefield
$g(r, t; r', t')$	- Green function
v_m	- Wave velocity in the media
R	- Distance between the TX/RX location to a point (x,y)
S	- Surface that contains all the sources or targets
$\theta_n(x, y)$	- n-th B-scan image
$r_{s_n}(z, x_n, f_m)$	- Focused data
$r_{wd_n}(z, x_n, f_q)$	- Windowed data
$\Delta_p(z, k_x, k_y)$	- Interpolated matrix
$\Delta_s(z, k_x, k_y)$	- Scaled matrix
$f_y(x, z)$	- Horizontal image

- $H(u, v)$ - Filter in the pixel domain
- ΔM - Scaling filter value
- Δx - Sampling interval along the x axis
- Δz - Sampling interval along the z axis

Chapter 1

Introduction

Imaging techniques such as through-wall imaging or subsurface imaging can provide information about areas where humans do not have access. These techniques are widely used for many applications such as geological studies (e.g., pipe detection, geologic hazards), and military applications (e.g, mine detection, hostage-rescue situations) [1-2].

Subsurface imaging has been a research topic for many years. One of its first applications was in the oil industry, where the initial purpose was to detect the location of any mineral deposits. Over time, this technique has been used in many other applications such as pipe detection and archaeological excavations [3]. Recently, it has been extended to security applications such as landmine detection. This application is important as approximately 110 million land mines are buried in 68 different countries [4], and many civilians die from landmines every year.

Different methods have been developed to determine the location and type of subsurface objects. These techniques can be broadly divided into five categories [3]. The first category is based on magnetometry [5], which measures changes in the magnetic field of the earth caused by the change of materials below the surface. The second category is based on resistivity [6], which induces an electrical current into the soil and locates objects based on the differences in voltage between the transmitter and receiver. The third category is based on electromagnetic conductivity [7], where a geometrically complex electromagnetic field is induced, the effect on

the subsoil is measured, and the object is located. The fourth category is based on thermal imaging [8], which measures the heat from the ground and locates the object. The fifth category is based on radar, which transmits a signal and receives a reflection from the object. By analyzing the echo, the object's location and properties can be determined. Radar was used for subsurface imaging [9] in the 1970s as its properties are perfectly suited for material penetration and target detection. This radar was commercially known as ground-penetrating radar (GPR) [10], and later this principle was extended to through-wall imaging (TWI) applications.

Through-wall imaging has been an important security application in recent times, especially for military applications (e.g., hostage situations) and safety purposes (e.g., fire rescues) [1-2]. In the last few years, several TWI techniques have been proposed in the literature. These techniques can be divided into three categories [11]. The first category is based on the acoustic principle, where an ultrasonic signal is transmitted and the objects are located by processing the received echo. The second category is based on X-rays [12], which radiate high-energy X-rays through the area to be studied, and the image is captured with a photographic film or detector. The third category is based on radar [13], which is the principle of GPR. These technologies have been shown to satisfy the requirements of TWI, but have some limitations such as safety issues and detection ranges.

Radar has been shown to be very efficient in object detection and has been used in many applications since World War II. In a radar system, a transmitter sends an electromagnetic signal and detects the echo of the reflected signal from a target. From this reflected signal, important information about the object can be extracted. The reflected signal power is directly proportional to the transmitted power and the antenna gain [14]. The different types of radar include Doppler radar and synthetic aperture radar. Doppler radar [15] has been used by the police to detect

speeding automobiles. The synthetic aperture radar [16] is used for surface imaging, and remote sensing from airplanes or satellites. Recently, ultra wideband (UWB) radars have been proposed [17, 18] to further improve the detection performance. UWB radar has many advantages over other radar. For example, the bandwidth of UWB radars from 1 to 10 GHz provides both the penetration capability, due to lower frequencies, and good resolution due to higher frequencies. UWB radar is very robust to noise, because of the large bandwidth of the transmitted signal.

In TWR and GPR, the transmitted wave generally travels through a multilayer environment, where the layers are typically, air, wall and ground. The wave speed and wave direction change from medium to medium, making the processing complex. Careful processing that accounts for all the details mentioned above is required to be able to extract the right information.

1.1 Objective and Major Contributions

The objective of this thesis is to develop an efficient imaging technique suitable for a multilayer environment. The developed technique should detect a target and provide an image showing important features about the target (e.g., shape and size).

The major contribution of this thesis in the area of radar signal and image processing is the development of an efficient modified migration technique using a two-dimensional Synthetic Aperture Radar (SAR) principle for a two-layer environment. This modified technique can be considered as a generic technique because it can be used in TWR and GPR imaging applications. An efficient filtering technique used in the backprojection reconstruction is implemented in the

modified technique in order to improve the generated image by reducing the blurring generated in the reconstruction and focusing on the high-energy components of the image.

1.2 Organization of the Thesis

This thesis is organized as follows. Chapter 2 provides a literature survey about radar principles, including signal processing and existing radar imaging techniques such as Kirchhoff migration. This survey is followed by the description of an existing GPR signal processing technique based on F-K migration principles, and an image reconstruction technique based on backprojection. Chapter 3 presents the proposed migration and filtering technique. In Chapter 4, the experimental set-up and resulting images are discussed. Chapter 5 presents conclusions and suggestions for future work.

Chapter 2

Background Review

In the published studies of radar imaging, multiple imaging approaches have been developed for security and military applications. The desire to identify objects, human positions, and building or geophysical layouts [19] has increased the interest in developing an efficient imaging technique. Different conventional imaging techniques, such as migration techniques [20], make use of the wave equation to calculate the phase and the time from where and when, respectively, the data were collected. The collected data is then analyzed, and the image is reconstructed. In an imaging environment, free space propagation typically does not exist, so that the signal speed and direction change due to the change of media. In order to obtain good results, one must compensate for the effects of a multi-layer environment in the signal. In this chapter, we first present a brief introduction to radar and its main principles. We then present a brief review of a few selected radar imaging techniques.

2.1 Radar History

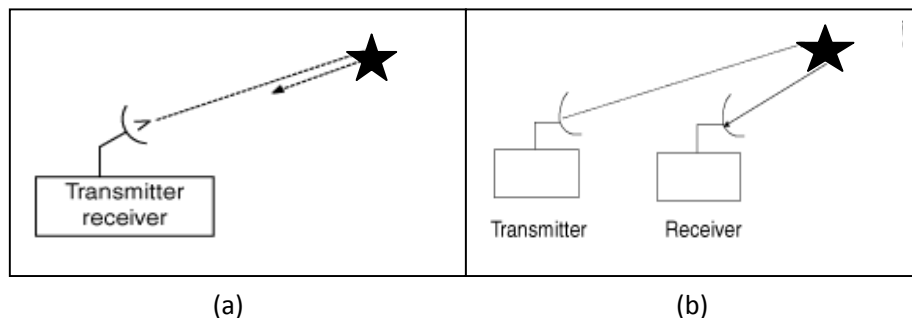
In the late nineteenth century, Heinrich Hertz demonstrated that radio waves could go through different type of materials, reflecting part of the transmitted signal. In the early twentieth century, radio waves became an interesting research topic, and scientists tried to find a practical

use for radio waves for object detection. Several researchers focused on developing an innovative system to transmit and receive radio waves that would provide useful information about an object.

Radar theory became very important during the World War II, when ships and airplanes were navigated by using radars. Radars were also used to detect enemy objects. In the 1950's, after the war was over, a new application for radar systems was found. Imaging radar was initially developed for military purposes and was known as Side Looking Airborne Radar (SLAR). A few years after the data acquisition, civilians were allowed to access the classified data for geological and natural resource studies.

2.2 Radar Principles

A radar system includes a transmitter and a receiver. The transmitter sends a radio wave signal. When this signal encounters an object, some portion of it is reflected back to the radar. From the reflected energy of the signal, important information about the target can be extracted. The two types of radar are monostatic radar and bistatic radar [21]. In monostatic radar, the transmitters and receivers are physically very close, while in bistatic radar, the transmitter and receiver are separated by a longer distance (see Fig. 2.1).



(a) (b)
Figure 2.1: Radar transmitter and receiver (a) Monostatic Radar, (b) Bistatic Radar.

2.3 Wave Propagation Principles

The radar principle is based on the correct interpretation of the wave reflected by a target. For this reason, many wave properties such as speed, frequency and power have become important.

The speed of an electromagnetic wave depends on the dielectric constant (ϵ_r) of the material through which the wave is traveling. In a vacuum, the wave speed (c) is approximately 3×10^8 m/s. If the wave is traveling through matter, the wave speed (v) can be calculated as follows:

$$v = \frac{c}{\sqrt{\epsilon_r}} = \frac{c}{n}, \quad (2.1)$$

where $\sqrt{\epsilon_r}$ is an approximation of the refraction index (n) of the material.

When an EM wave passes through multiple media, a relationship exists between the wave speed for each medium and the angles of incidence and refraction. This relationship is shown in Fig. 2.2 and is known as Snell's law, which is described as follows:

$$\frac{\sin\theta_1}{\sin\theta_2} = \frac{v_1}{v_2} = \frac{n_2}{n_1}. \quad (2.2)$$

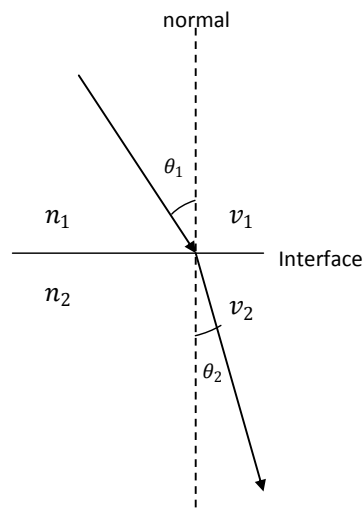


Figure 2.2: Ray refraction at the transition of two media

2.4 Radar Image Formation

Radar imaging techniques were initially developed for GPR, aeroplane or satellite imaging, and later, such applications were extended for TWR. These techniques have been part of many studies over the years. In the following, we explain the process of data acquisition, pre-processing, and interpreting. The section concludes by explaining in detail a few popular techniques used for radar imaging.

2.4.1 Signal Transmission and Acquisition

In order to explain radar signal acquisition, the transmission and reflection process will be described. Let the transmitted signal be a frequency modulated signal [22] represented as

$$S_t(f_m, t) = Ae^{-j2\pi f_m t}, \quad (2.3)$$

where $f_m = f_0 + m\Delta f$, Δf is the step frequency, and A is the transmitted signal amplitude.

Examples of a transmitted signal waveform and its frequency are shown in Fig. 2.3(a) for a fixed antenna location. In Fig. 2.3(a), a pulse of a continuous wave is transmitted at t_0, t_1, \dots, t_{M-1} , respectively, at a fixed amplitude. The frequency at each of these pulses changes from f_0 to f_{M-1} , respectively, as shown in Fig. 2.3(b).

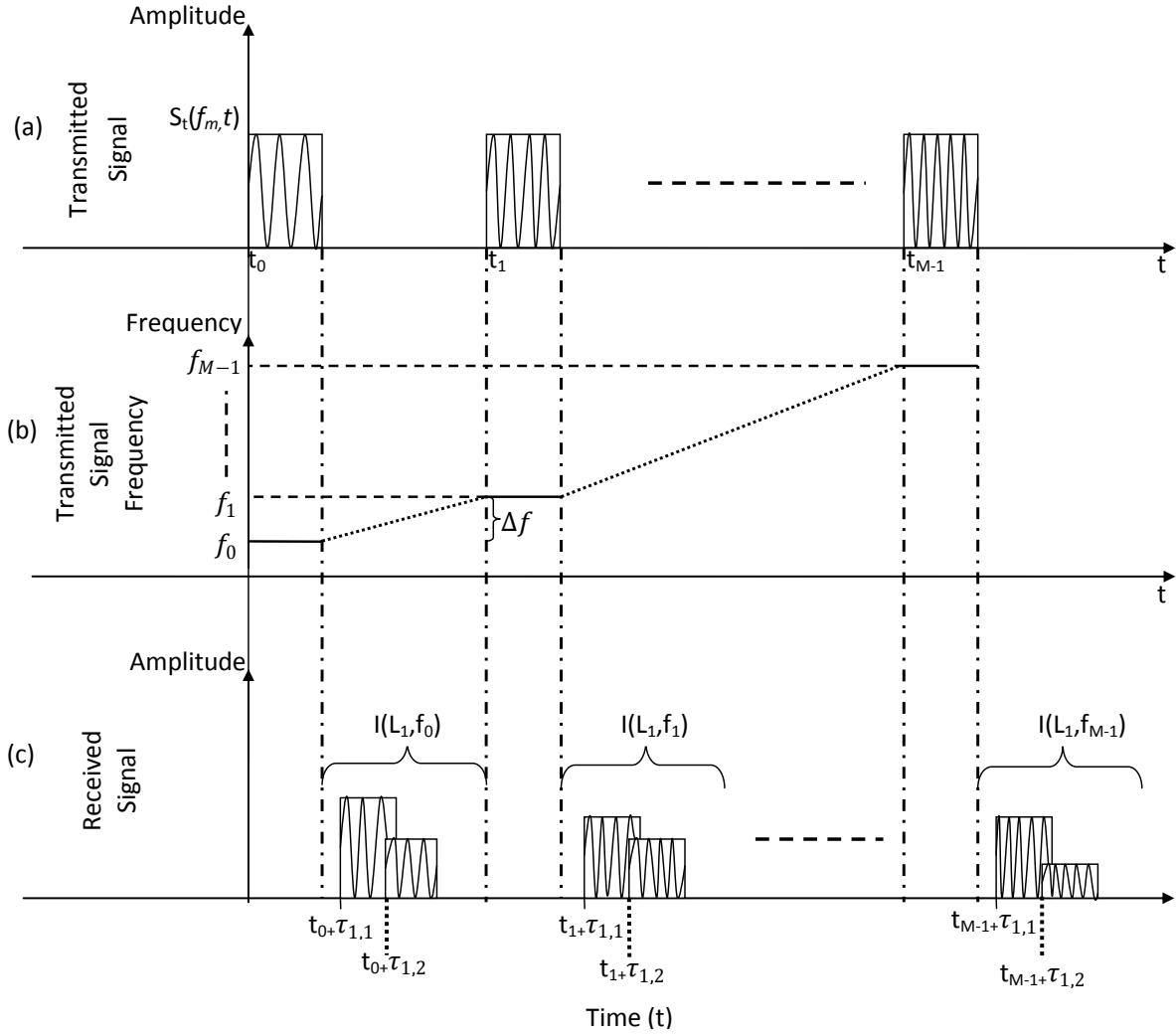


Figure 2.3: (a) Transmitted signal, (b) Transmitted Step frequency, and (c) Received signal.

Consider a monostatic antenna at a position L_1 and the two targets p_1 and p_2 as shown in Fig. 2.4. Assume that the antenna is in one medium (e.g., air) and that the targets are in another medium (e.g., sand). Let the antenna position be denoted by (x,y) . Assume that the antenna moves along the x -axis to n different locations. Let the round trip propagation delay between the n -th TX/RX location (L_n) and a target p be denoted by $\tau_{n,p}$ (e.g., $\tau_{n,1}$ and $\tau_{n,2}$ in Fig. 2.4). Assume that the TX pulse width is less than the round trip $\tau_{n,p}$ and no overlap occurs between the transmitted and received signals.

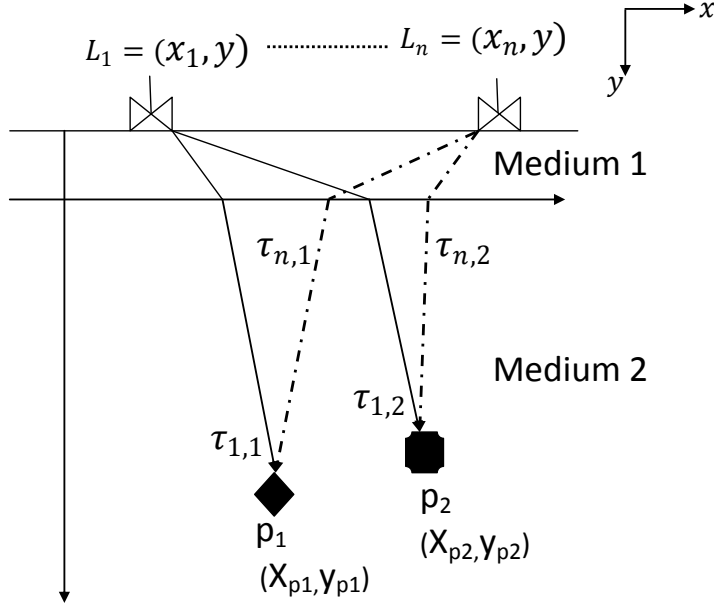


Figure 2.4: Transmitted (TX) and received (RX) signals for a two target scenario

In the case of this two target scenario, the receiver will receive two reflected signals with propagation delays $\tau_{1,1}$ and $\tau_{1,2}$ as shown in Fig. 2.3(c). Assuming $n=1$, these two signals can be expressed in the following form:

$$E_{p_1}(f_m) = A_1 e^{-j(2\pi f_m(t+\tau_{1,1}))} \quad ; \quad E_{p_2}(f_m) = A_2 e^{-j(2\pi f_m(t+\tau_{1,2}))}, \quad (2.4)$$

where E_{p_1} is the reflected signal from target p_1 , and E_{p_2} is the reflected signal from p_2 . The received signal $I(L_1, f_m)$ can be obtained by adding these two signals as follows:

$$I(L_1, f_m) = \sum_{k=1}^P E_{p_k}(f_m), \quad (2.5)$$

where P refers to the number of targets in the scenario, and p_k is the received signal of a specific target.

In general, when there are P targets, the acquired signal can be obtained as

$$I(L_1, f_m) = \sum_{p=1}^P A_p \exp \{-j2\pi f_m (t + \tau_{n,p})\}. \quad (2.6)$$

Fig. 2.4 reveals that the first received signal is the reflection from p_1 followed by the reflection from p_2 . The amplitude A_p of each received signal will depend on the target position with respect to the receiver, and also on the target size and material. The overall acquired signal $I'(L_1, f)$ for the TX/RX position L_1 will be the $M \times 1$ vector given below:

$$I'(L_1, f) = \begin{bmatrix} I(L_1, f_0) \\ I(L_1, f_1) \\ \vdots \\ I(L_1, f_{M-1}) \end{bmatrix}. \quad (2.7)$$

2.4.2 Vector Network Analyzer (VNA) S-parameters

A Vector Network Analyzer is a test instrument used in the RF measurements to characterize electrical components and circuits. It measures the magnitude and phase of a scattered signal, allowing the characterization of a device under test (DUT) in the time domain. The VNA accurately calculates and stores the scattering parameters by observing and comparing the transmitted and reflected signals. This device is used to simulate transmitted and received radar signals in a lab environment. The VNA can have multiple ports, but in this section, only a two-port VNA is explained. In order to characterize the RF networks, the S-parameters are defined in terms of the incident and reflected signal voltage. A k -port device has k^2 S-parameters;

for example, a two-port network has four S-parameters: S_{11} , S_{12} , S_{21} , and S_{22} . Fig. 2.5 shows the schematic of a two-port network.

The terms (a_1, a_2) and (b_1, b_2) represent the incident and output terms, respectively, for the two-port network. By using this information, a network is characterized in the following way: The first subscript is the port where the signal emerges, and the second subscript is the port where the RF signal enters. If the subscripts are the same, a reflection measurement is taken from the respective subscript port number as shown in Fig. 2.5.

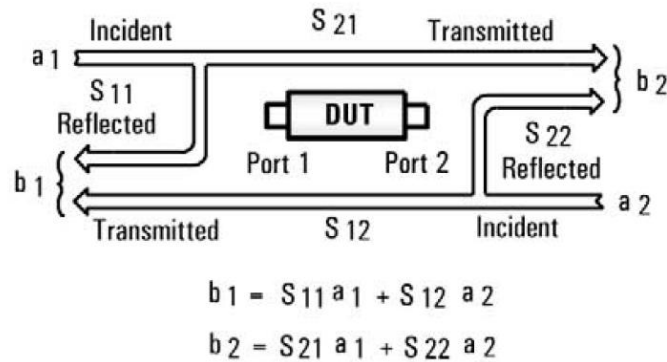


Figure 2.5: Schematic of a two-port network and the S-parameters. The DUT is the device under test [23]

Fig. 2.6 shows the calculation of S-parameters that will involve the measurements of the incident (I), reflected (R) and transmitted (T) signals. This scenario clearly explains the performance of an ideal system where the device under test is placed between port 1 and port 2 and obtains these three different values. S_{21} is the ratio between the transmitted signal at port 2 and the incident signal at port 1, S_{12} is the ratio of the transmitted signal measured at port 1 and the incident signal at port 2, S_{11} is the ratio of the incident and reflected signal at port 1, and S_{22} uses the incident and reflected signals at port 2. S-parameters have both the magnitude and phase information of the RF scattered signal.

In this work, one antenna is connected at each port. One of these antennas acts as a transmitter and the other acts as a receiver. Fig. 2.7(a) shows the experimental set-up, showing the locations of VNA, the transmitting and receiving antennas, and the target inside a box. Fig. 2.7(b) shows the cross-section of the target. In this case, the target is a metal pipe buried in sand. The antenna is moved along a plane above the sand layer. The distance between the antenna and the sand layer is 29 cm, and the target is buried between two 6 cm layers of sand as shown in Fig. 2.7 (b).

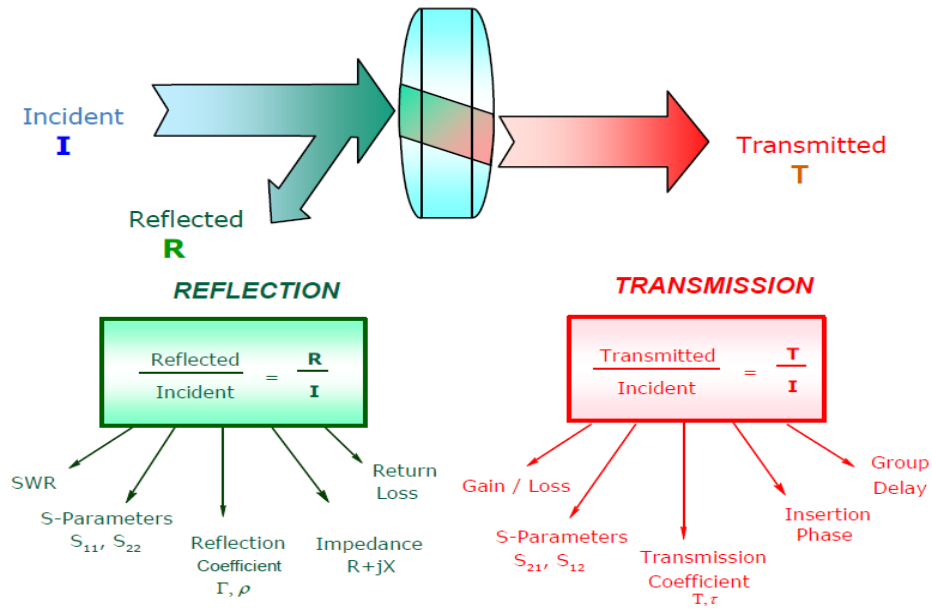


Figure 2.6: Wave performance over a target [24]

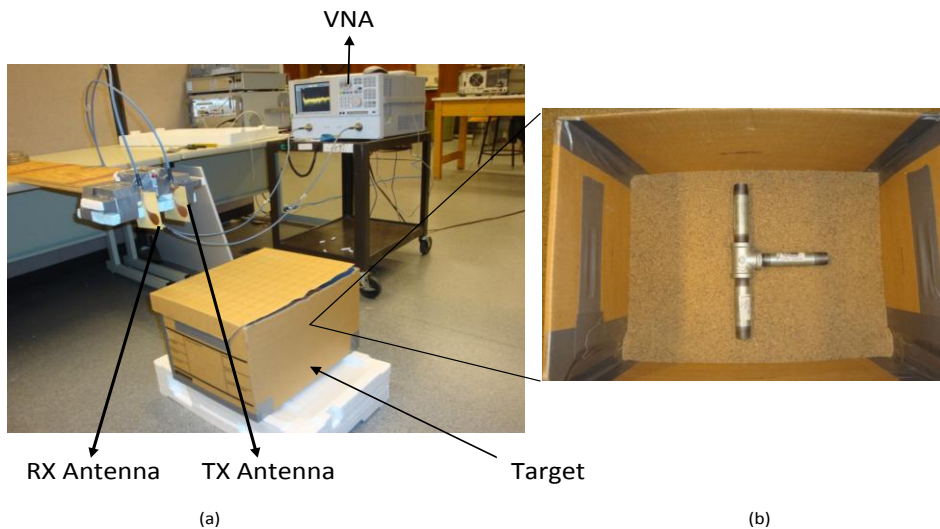


Figure 2.7: (a) Experimental set-up using a two-port VNA, (b) Target over a sand layer

In order to obtain the S-parameters to characterize a DUT, the user must to define a desired transmitted signal, a specific bandwidth $[f_{start}, f_{end}]$ and the desired step frequency Δf . The source power is constant over the desired frequency band and transmits a sinusoidal signal at a certain frequency. The received signal can be found by calculating the reflection coefficient. The reflection coefficient Γ is defined as the amplitude of a reflected wave to an incident wave, and can be calculated by using the following formula:

$$\Gamma(f) = \frac{V_R}{V_{INC}} = |\Gamma(f)|\angle\Gamma(f), \quad (2.8)$$

where V_R is the reflected voltage and V_{INC} is the incident voltage. The reflected voltage V_R represents the addition of the reflected power of the different scattering elements covered by the beamforming. The magnitude of the reflection and transmitted coefficient can also be expressed in the dB scale as

$$|\Gamma|(in\ dB) = -20 \log(|\Gamma|). \quad (2.9)$$

The phase $\angle\Gamma$ is obtained after comparing the phase of the incident and the reflected signal. These values are obtained for different frequency values from the VNA, and the acquired signal is represented as (L_1, f_m) , where L_1 represents the antenna location, and f_m is the transmitted signal frequency.

Each of four S-parameters is expressed as a complex coefficient (magnitude and phase). Fig 2.9 shows the variation in the magnitude of the four S-parameters for different frequencies when using the experimental set-up shown in Fig. 2.7 for a one-antenna location. The phases obtained by using the same S-parameters in Fig. 2.8 are shown in Fig. 2.9. The way this reflected signal is generated is explained as the reflection of a transmitted EM wave that finds discontinuity in the material properties. The VNA gets only one reflected signal back, which contains the reflected energy from all the possible targets in the area. This reflected energy does not isolate individual

targets. Therefore, signal processing is required in order to determine the number of targets and their position in the area of study.

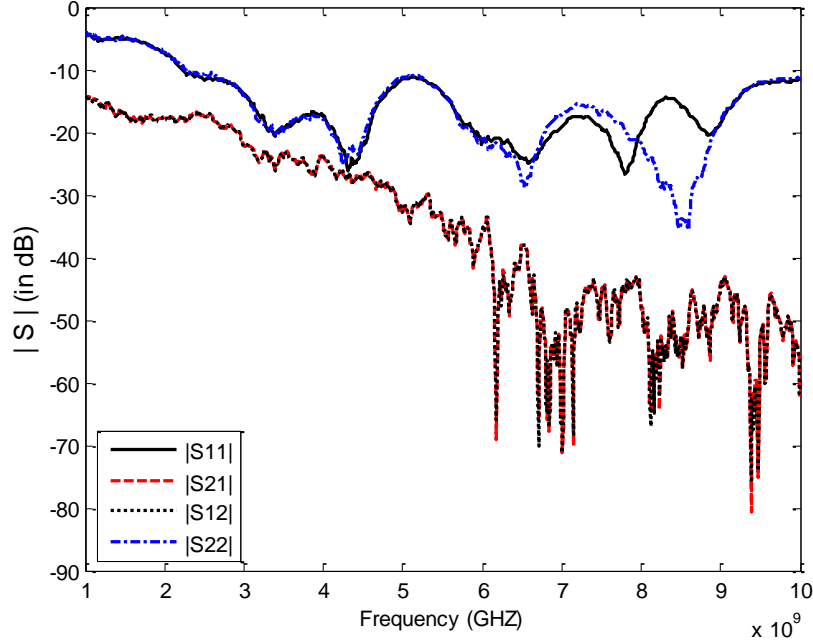


Figure 2.8: Variation of the magnitude of all S-parameters over transmitted frequency

VNA data (L_1, f) is represented as a $M \times 1$ vector for each S-parameter (magnitude and phase) and each frequency, assuming an antenna position L_1 :

$$(L_1, f) = \begin{bmatrix} '(L_1, f_0) \\ '(L_1, f_1) \\ \vdots \\ '(L_1, f_{M-1}) \end{bmatrix}. \quad (2.10)$$

(L_1, f) will store the frequency response of the channel for different frequency values, and each of these values can be expressed as $||e^{j\theta}$. Fig. 2.10 shows a typical discrete plot of values for different frequencies.

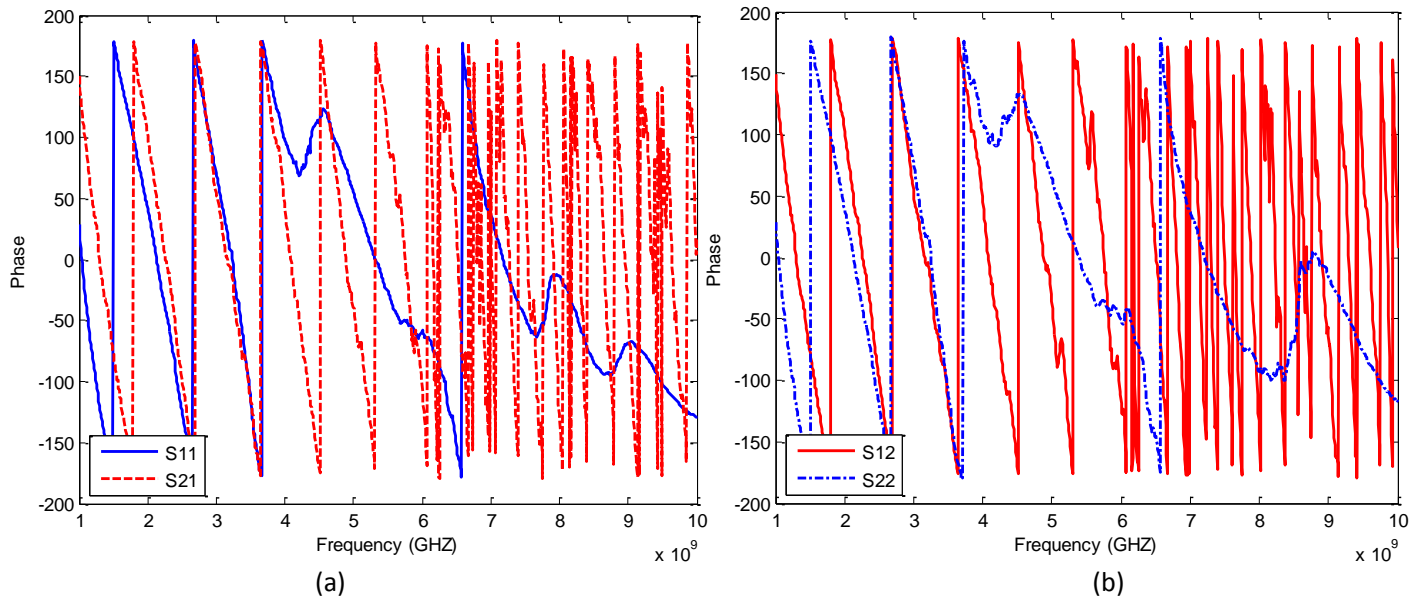


Figure 2.9: Phase variation of reflection coefficient over transmitted frequency
 (a) S₁₁ and S₂₁ phase parameters, (b) S₁₂ and S₂₂ phase parameters.

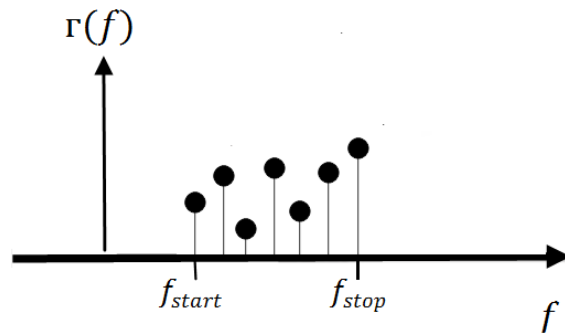


Figure 2.10: Obtained reflection coefficients representation

2.4.3 Acquired Signal Pre-processing

It was shown in section 2.4.2 that the S_{21} parameter of the VNA measures the reflection coefficient of the object at the VNA 2nd port, which can be considered as the transfer function of the channel as follows:

$$\Gamma(f) = \frac{V_R}{V_{INC}} \Leftrightarrow \frac{\mathcal{F}\{v_R\}}{\mathcal{F}\{v_{INC}\}} = \Gamma(f) = \mathcal{F}\{\gamma(t)\}, \quad (2.11)$$

where $\gamma(t)$ is the impulse response of the channel.

For radar signal processing, the data in the time domain must be characterized. As VNA collects only the data for positive frequencies, a VNA data pre-processing must be performed to be able to carry out the inverse Fourier transform and obtain the impulse response of the collected data. The pre-processing steps are shown in Fig. 2.11, which presents the four steps discussed below.

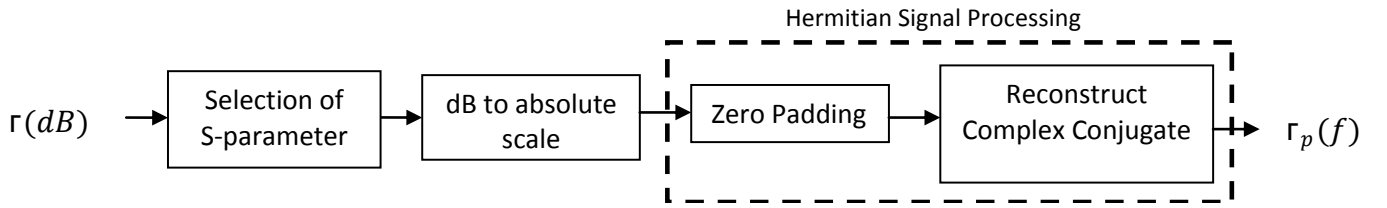


Figure 2.11: Signal pre-processing

Selection of S-parameter: In this step, a suitable S-parameter is chosen. In this thesis, we have chosen S_{21} , because we want to use the channel where the incident signal goes through port 1, and the received signal is obtained through port 2. The reflection coefficients ($|\Gamma(f)| \neq \Gamma(f)$) corresponding to S_{21} are considered for further processing.

dB to absolute scale: The VNA provides the reflection coefficients in polar form $|Γ(f)|∠Γ(f)$. Therefore, for further processing, these values expressions must be transformed back to an absolute scale and Cartesian form ($z = |Γ(f)|e^{j∠Γ(f)} = a + bj$).

Hermitian Signal Processing: The Hermitian symmetry property states that the Fourier transform of a real valued function is Hermitian symmetric. As the channel impulse response function $γ(t)$ is real valued, the $Γ(f)$ will be Hermitian symmetric; i.e., $Γ(-f) = Γ^*(f)$. Although the complete frequency range of $Γ(f)$ is $[-f_{stop}, f_{stop}]$, the VNA produces the corresponding to only the positive frequency as the for negative frequencies is redundant. In order to calculate $γ(t)$, $Γ(f)$ between $[-f_{stop}, f_{stop}]$ must be generated. This process is shown in Fig. 2.12. Fig. 2.12 (a) shows $Γ(f)$, for $f = [f_{start}, f_{stop}]$. The first step is shown in Fig. 2.12 (b) where zero padding has been done for the frequency between $[0, f_{start}]$. The number of zeros to be padded is calculated as follows:

$$\text{Number of zeros} = \frac{f_{start}}{\Delta f} - 1, \quad (2.12)$$

where Δf is the step frequency.

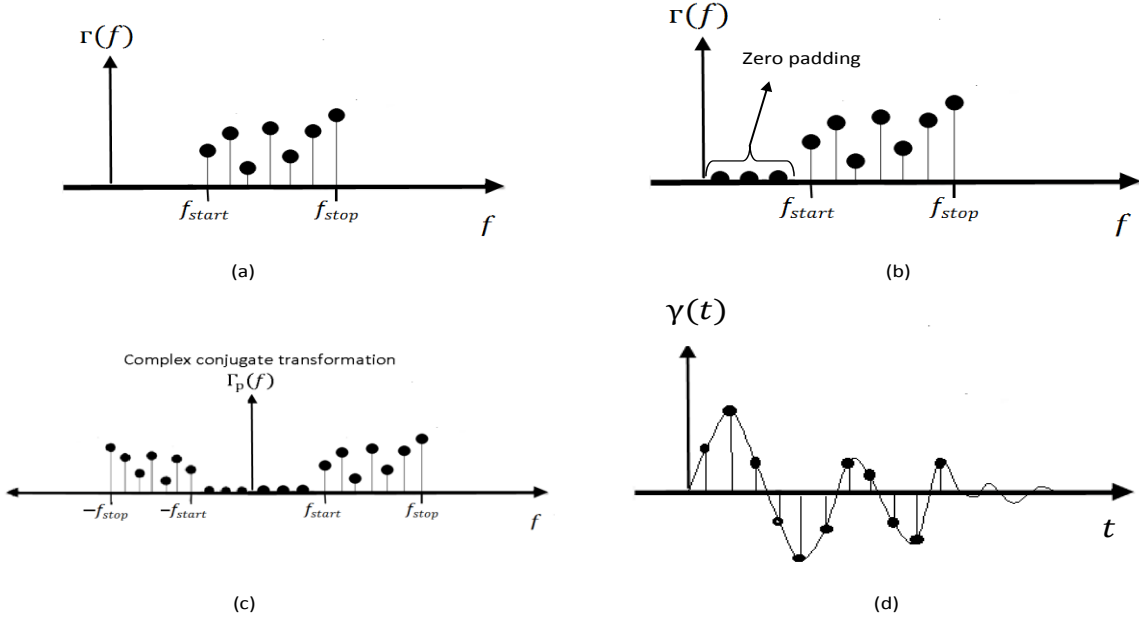


Figure 2.12: (a) Acquired S-parameter values, (b) Zero padding from $f=0$ to f_{start}
 (c) Complex conjugate signal, (d) Reconstructed time domain signal

After Zero padding, we obtain $\Gamma(f)$ for $f = [0, f_{stop}]$. The next step is to generate $\Gamma(f)$ for $f = [-f_{stop}, 0]$. This process can be easily done by using the Hermitian property of $\Gamma(f)$ and generating $\Gamma_p(f)$, as shown in Fig. 2.12 (c). The time domain channel impulse response function $\gamma(t)$ can be calculated as $\gamma(t) = \mathfrak{F}^{-1}\{\Gamma_p(f)\}$, which is shown in Fig. 2.12(d). Both f and $\gamma(t)$ are discrete, and the time resolution Δt of $\gamma(t)$ can be calculated as follows:

$$\Delta t = \frac{1}{f_{stop} - f_{start}} . \quad (2.13)$$

All four S-parameters can provide an impulse response, but the one shown in Fig. 2.13 was obtained by using the S_{21} parameter for one antenna location by using the experimental set-up shown in Fig. 2.7. This process was repeated for each antenna position.

We now explain the channel impulse response estimation process by using an experiment conducted in the lab as shown in Fig. 2.7 (a). The frequency bandwidth was set between 1 GHz

and 10 GHz, and the step frequency $\Delta f = 10 \text{ MHz}$. For each antenna location, the number of samples produced by the VNA $= \left(\frac{10 \times 10^9 - 10^9}{10^7}\right) = 901$ samples. The number of zeros to be padded for frequencies between 0 and 1 GHz $= \left(\frac{10^9}{10^7}\right) = 100$. After zero padding, and Hermitian extension in the negative frequency axis, the number of coefficients in $(f) = 1001 * 2 = 2002$. The IFFT produces 2002 samples of $\gamma(t)$. As the time resolution in the resulting impulse response is $0.11 = \left(\frac{1}{9 \times 10^9}\right) \text{ ns}$, the 2002 samples correspond to a duration of 200.2 ns. Fig. 2.13 shows the $\gamma(t)$ corresponding to the S_{21} function shown in Fig. 2.8 and 2.10(a).

The computed time domain waveform is the result of the convolution of the different impulse responses generated by different sources belonging to the radar system, in addition to the noise contribution from different sources in the environment [25]. The received impulse response $\gamma(t)$ can be represented as

$$\gamma(t) = [\gamma_s(t) \otimes \gamma_{at}(t) \otimes \gamma_{mt}(t) \otimes \gamma_t(t) \otimes \gamma_{mr}(t) \otimes \gamma_{ar}(t)] + \gamma_c(t) + n(t), \quad (2.14)$$

where $\gamma_s(t)$ is the transmitted signal, $\gamma_{at}(t)$ and $\gamma_{ar}(t)$ are the impulse responses of the transmitter and receiver antennas, $\gamma_c(t)$ is the antenna cross coupling response, $\gamma_{mt}(t)$ and $\gamma_{mr}(t)$ are the transmitted and reflected medium responses, respectively, when one of the mediums is typically air. $\gamma_t(t)$ is the target impulse response, and $n(t)$ is the noise.

The antenna impulse response will contribute to the radar resolution. If the impulse response of the antenna is very short, it will not distort the transmitted signal and will not generate sidelobes, which degrade the images and obscure the targets. The antenna cross-coupling response is composed of the transmitted signal that goes straight to the receiver antenna. The medium response is the effect that the medium reflection (wall or sand) has on the signal. The target

impulse response is composed of the contribution of the target and other scatters buried in the sand that might not be desired in our detection.

The time of arrival is related to the distance between the antenna and scatters, and also to the velocity of propagation.

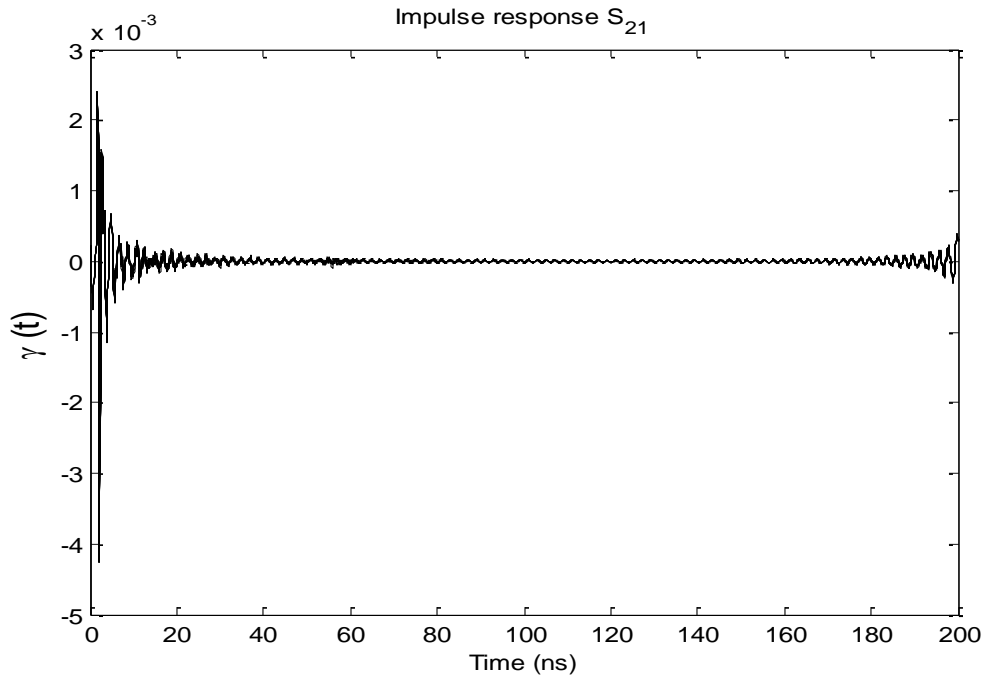


Figure 2.13: Reconstructed impulse response function $\gamma(t)$ after Hermitian signal processing

2.4.4 Recorded Data Interpretation

In order to obtain a high-resolution image, the radar data need to be collected at different antenna locations. Fig. 2.14 shows the locations of the antenna positions used during the experiment. The collected data is an $N \times N \times M$ 3-D matrix. Let this matrix be denoted by (z, x, f) . Consider a 1-D part of the 3-D matrix (z, x, f) for a (z, x) value. This 1-D value can be interpreted as the impulse response corresponding to that specific (z, x) antenna position. This 1-D response is known as an A-scan [26]. From each A-scan, limited information about the target

such as the target location can be extracted. In order to obtain more information about the target, the collected data along one of the axis (x-axis or z-axis) must be used to generate a 2-D image. For this purpose, for the matrix (z, x, f) , assume that the z value is kept fixed, and x is varied ($x=\{x_1, x_2, \dots, x_N\}$) and f is varied ($f=\{f_1, f_2, \dots, f_M\}$). In other words, for a given z value, we obtain a 2-D image which is a B-scan. From one B-scan, the position (horizontal location on x -axis and the depth of the object in the y axis) of the object can be calculated. If the objective is to extract a full target description (location along x, y and z axis), we need to use all the collected data (z, x, f) and generate a 3-D image. From this image, information such as the 3-D target location and target size can be estimated. This type of data collection is known as a C-scan.

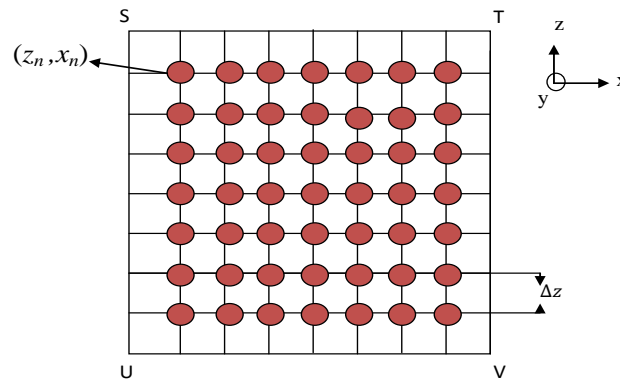


Figure 2.14: TX/RX position

2.4.4.1 VNA Data and Scattering Distance Relation

The VNA system can be explained as a linear time invariant (LTI) system as shown in Fig. 2.15.

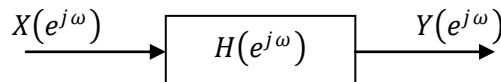


Figure 2.15: LTI system diagram

In Fig. 2.15, $X(e^{j\omega})$ represents the input of an LTI system with frequency response $H(e^{j\omega})$, and $Y(e^{j\omega})$ is the output of the LTI system. They all can be related in the following equation:

$$Y(e^{j\omega}) = H(e^{j\omega})X(e^{j\omega}) \quad (2.15)$$

$$|Y(e^{j\omega})| = |H(e^{j\omega})||X(e^{j\omega})| \quad (2.16)$$

and

$$\angle Y(e^{j\omega}) = \angle H(e^{j\omega}) + \angle X(e^{j\omega}). \quad (2.17)$$

As shown in Eq. 2.16, the input magnitude is scaled by the magnitude of $|H(e^{j\omega})|$. For this reason, $|H(e^{j\omega})|$ is commonly known as the system amplitude gain. Eq. 2.17 shows that the input phase $\angle X(e^{j\omega})$ is modified by the LTI system by adding the phase $\angle H(e^{j\omega})$. The $\angle H(e^{j\omega})$ is commonly known as the system phase gain.

The phase becomes a very important aspect of signal processing because the phase is directly related to the target distance from the measurement point as shown as follows:

$$\Gamma(f) = Ae^{-j\left(\frac{2\pi f}{c}\right)2d}, \quad (2.18)$$

where A is the target scattering amplitude, f is the transmitted signal frequency, c is the speed of light, and d is the one-way target distance from the measurement point.

If P scattering points are located at different positions, the reflected signal can be expressed as follows:

$$\Gamma(f) = \sum_{i=1}^P Ae^{-j\left(\frac{2\pi f}{c}\right)2d_i}. \quad (2.19)$$

In order to verify the Eq. 2.19, a test scenario was simulated by using MATLAB. It was assumed that 3 different targets were in the scenario. The three targets were located at 1, 2 and 3 meter distances from the measurement point, and the scattered amplitude of each target was 5, 3

and 1, respectively. The signal was processed by using a range of frequencies from 1 to 6 GHz with a step frequency of 6.25 MHz, generating 801 samples.

The impulse response shown in Fig 2.17 was obtained after the reflected signal from the proposed scenario was processed by using the Hermitian signal processing explained in section 2.4.3. The range resolution of Fig. 2.16 was calculated as follows:

$$d = \frac{t}{2} * c. \quad (2.20)$$

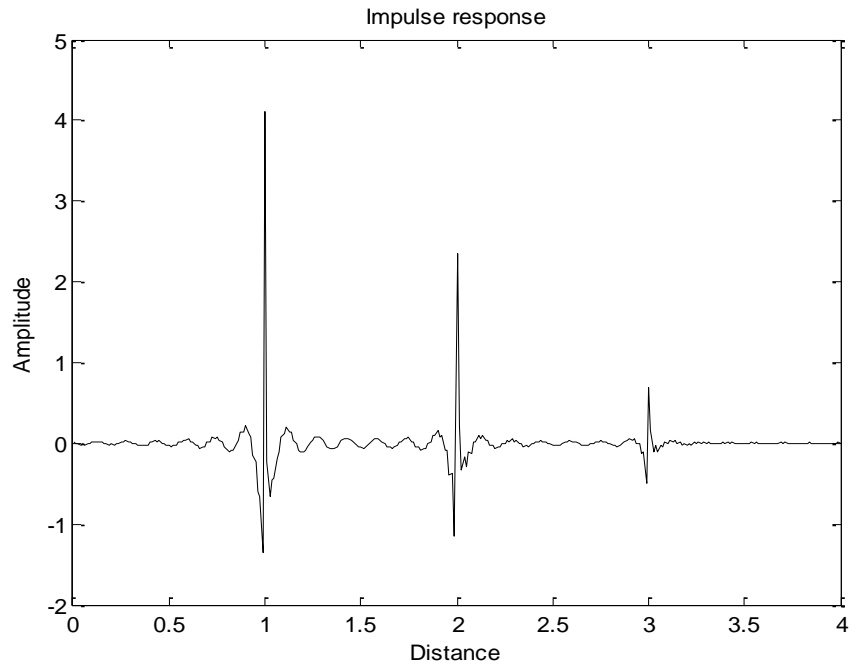


Figure 2.16: Three scattering simulation results

The phase difference between the transmitter and the received signal can be expressed as follows:

$$\phi = \frac{f(2 * 360)}{c} \left\{ d - \left[\frac{m * \lambda}{2} \right] \right\} - 180, \quad (2.21)$$

where ϕ is the VNA measured phase, $c = 3 \times 10^8$ m/s is the wave velocity, f is frequency, d is the one-way distance between the TX/RX and scattering source, $\lambda = c/f$ is the wavelength, and m is the number of cycles or periods.

By rearranging the terms in Eq. 2.21, the distance d can be expressed as

$$d = \left[\frac{\phi + 180}{2 * 360} * \frac{c}{f} \right] + \left[\frac{m * \lambda}{2} \right]. \quad (2.22)$$

From Eq. 2.22, the scattering distance at a certain frequency and certain period can be calculated. In order to verify Eq. 2.22, an experiment was proposed. A metal target was placed at 1 meter horizontally and 2 meters away from the VNA location. Twelve different measurements were taken during this experiment. The target dimensions were 73cm length and 65 cm width as shown in Fig. 2.17.

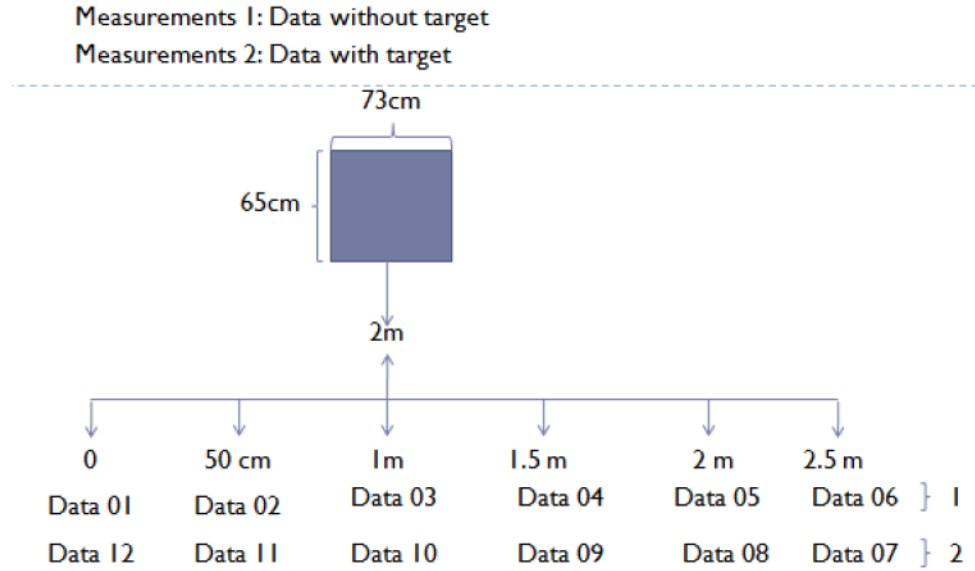


Figure 2.17: Free space propagation scenario

Consider the set-up in Fig. 2.17 and the phases collected at different frequencies by using the VNA at different locations.

Table 1 shows the distance d calculated for different frequencies and periods. As Table 1 shows, the target was detected in period (m) 14, 16, 17, 19 and 23.

Table 2.1: Distance calculation for VNA obtained phases of a free space propagation

Frequency (f)	1.00E+09	1.0063E+09	1.14375E+09	1.1875E+09	1.3188E+09	1.6125E+09
Wavelength (λ)	0.300000	0.29813665	0.26229508	0.25263158	0.22748815	0.18604651
Measured phase(\emptyset)	113.805944	111.285059	61.6826608	43.3953913	-38.5914634	-136.898951
m	Distance (meters)					
1	0.12241914	0.12061493	0.08804469	0.07838435	0.04467884	0.01113722
2	0.27241914	0.26968325	0.21919223	0.20470014	0.15842292	0.10416048
⋮	⋮	⋮	⋮	⋮	⋮	⋮
⋮	⋮	⋮	⋮	⋮	⋮	⋮
13	1.92241914	1.90943481	1.66181518	1.59417382	1.40960775	1.12741629
14	2.07241914	2.05850313	1.79296272	1.72048961	1.52335183	1.22043955
15			1.92411026	1.8468054	1.6370959	1.3134628
16			2.0552578	1.97312119	1.75083998	1.40648606
17				2.09943698	1.86458406	1.49950932
18					1.97832813	1.59253257
19					2.09207221	1.68555583
20						1.77857908
21						1.87160234
22						1.96462559
23						2.05764885

2.4.4.2 A-scan Signal Processing

The VNA output can be easily converted from the frequency domain to the time domain by using the inverse Fourier Transform. The main idea is to process the existing data and determine the exact location of each scattering source. Fig. 2.18 explains the steps commonly followed to reconstruct the impulse response signal from the VNA data.

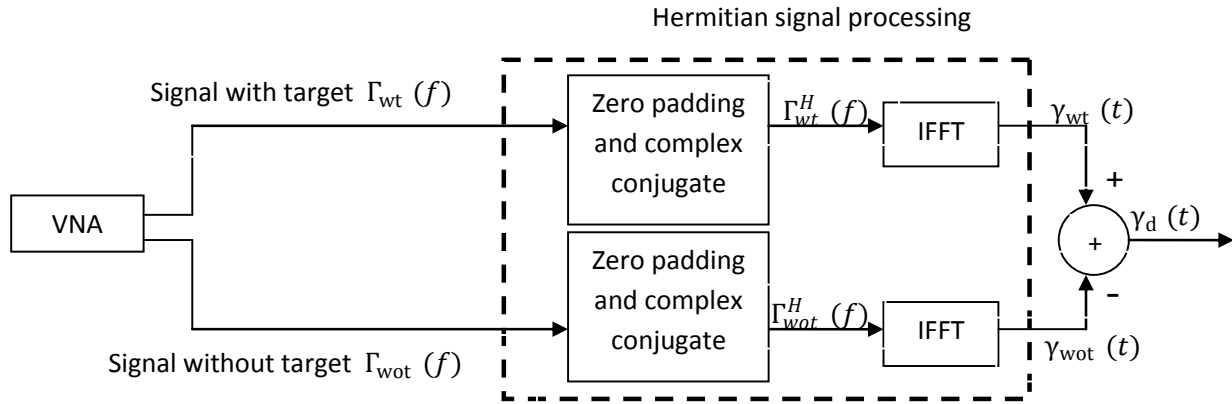


Figure 2.18: Impulse response reconstruction

For purpose of this processing and by using the scenario shown in Fig. 2.17, two different measurements must be taken: one in the open space, and one with a fixed target. The first sets of measurements were taken along a line of 2.5 meters. The VNA was moved every 50 centimeters along the 2.5 meters to collect a set of data labeled as Data 01 to Data 06. These data were taken by using an open space scenario without a target. The second set of measurements was taken again every 50 centimeters along the same 2.5 meters. These new data were labeled as Data 07 to Data 12 and were taken with the target in place, as shown in Fig. 2.17. Each measurement was taken over a bandwidth from 1 GHz to 6 GHz with 801 sample points in between. In other words, the frequency spacing between two consecutive sample points was $\Delta f = \frac{5 \times 10^9}{800} \approx 6.25 \text{ MHz}$. Fig. 2.19 shows two examples of spectra corresponding to location Data 03 (open space) and Data 10 (with a fixed target) of the experimental set-up.

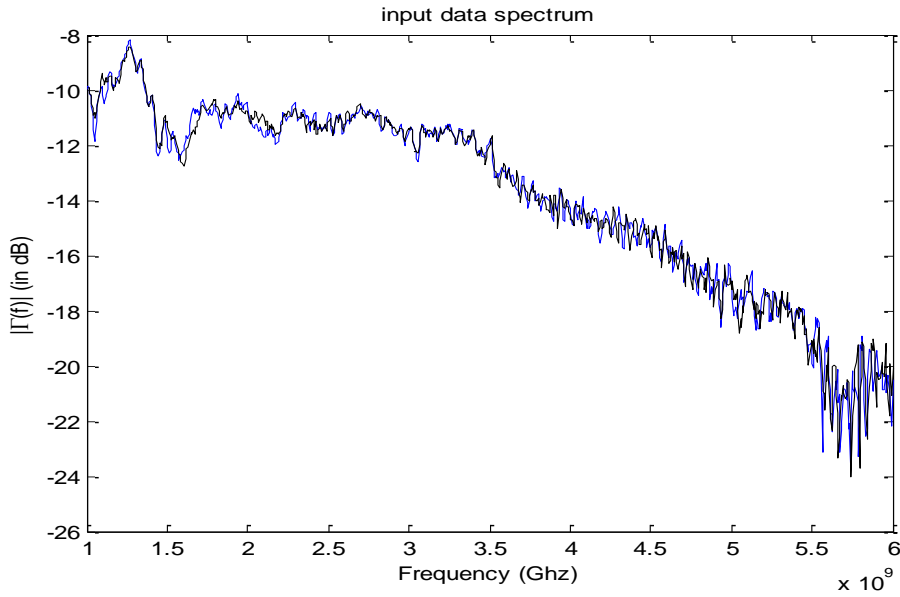


Figure 2.19: Input data spectrum of open space signal and signal with target corresponding to locations 03 and 10 in Fig. 2.17.

The Hermitian symmetry property states that the Fourier transform of a real valued function is Hermitian symmetric. The impulse response of the experimental system is assumed to be real valued. The complete Fourier spectra can be reconstructed by using the (f) corresponding to the Fourier transform of the impulse response for the positive frequencies band [1, 6] GHz, zero padding and generating the data for negative frequencies by using the Hermitian symmetry property. The complete process was explained in section 2.4.3, where the main objective is to generate the complete frequency range $[-f_{stop}, f_{stop}]$ or $p(f)$. For this purpose, the data (f) were converted to a Cartesian form $(z = a + bj)$ and then were zero padded in the frequency range $[0, f_{min}]$. In the present case, the number of zeros can be calculated as follows:

$$Number\ of\ zeros = \frac{10^9}{\Delta f} - 1 = 159. \quad (2.23)$$

The number of samples after the zero padding increases to 960 samples. Before calculating the IFFT, we expand the $p(f)$ for negative frequencies ($\Omega = [\pi, 2\pi]$) by using Hermitian symmetry as shown in Fig. 2.20. After the expansions, the data vectors $\Gamma_{wt}^H(f)$ and $\Gamma_{wot}^H(f)$ will have 1919 coefficients.

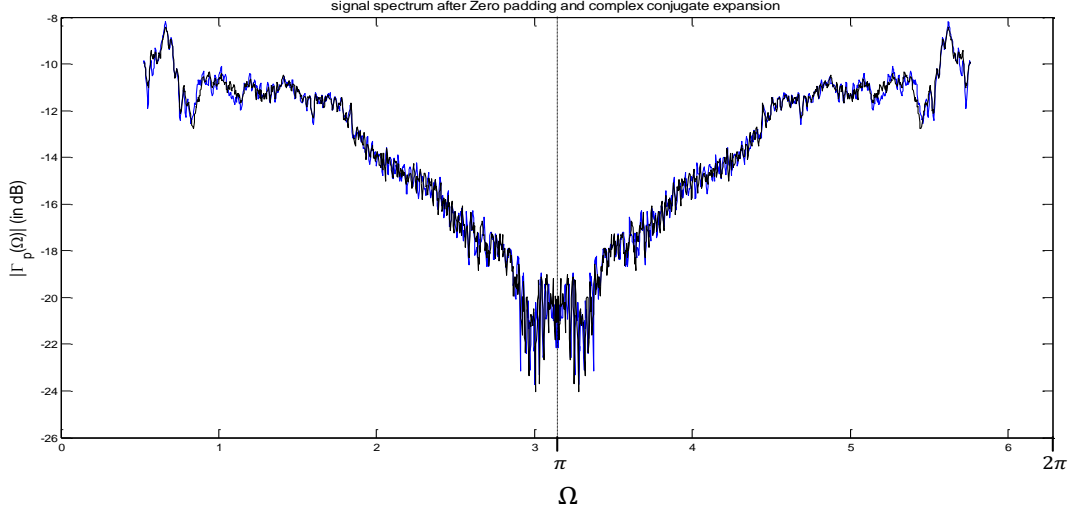


Figure 2.20: Signal spectrum after Hermitian signal processing. Blue signal is the signal without target. Black signal is the signal with target. Note that for $\Omega = [0, 0.52]$ and $[2\pi - 0.52, 2\pi]$, $|\Gamma| = 0 \approx -\infty$ dB

After the Hermitian expansion, the impulse response of the radar system is obtained as follows:

$$\gamma_{wt}(t) = \mathcal{F}^{-1}\{\Gamma_{wt}^H(f)\} \quad (2.24)$$

$$\gamma_{wot}(t) = \mathcal{F}^{-1}\{\Gamma_{wot}^H(f)\}, \quad (2.25)$$

where $\gamma_{wt}(t)$ is the impulse response of the system with target, and $\gamma_{wot}(t)$ is the impulse response of the open space system. Each of these responses contains 1919 samples.

The impulse response of the system due to the target is calculated as follows:

$$\gamma_d(t) = \gamma_{wt}(t) - \gamma_{wot}(t). \quad (2.26)$$

Note that $\gamma_d(t)$ eliminates the scattering effects of any object around the real target. The resulting $\gamma_d(t)$ is discrete, and the respective time resolution Δt can be calculated as follows:

$$\Delta t = \frac{1}{2 * f_{stop}}, \quad (2.27)$$

by using the minimum Nyquist rate, which is twice the highest frequency f_{stop} contained within the signal. Fig. 2.21 shows the $\gamma_d(t)$ of $\gamma_{wt}(t)$ and $\gamma_{wot}(t)$ corresponding to location Data 10 (with target) and Data 03 (without target) of the experimental set-up shown in Fig. 2.17. Fig. 2.22 shows the same signal at Fig. 2.21 with respect to distance.

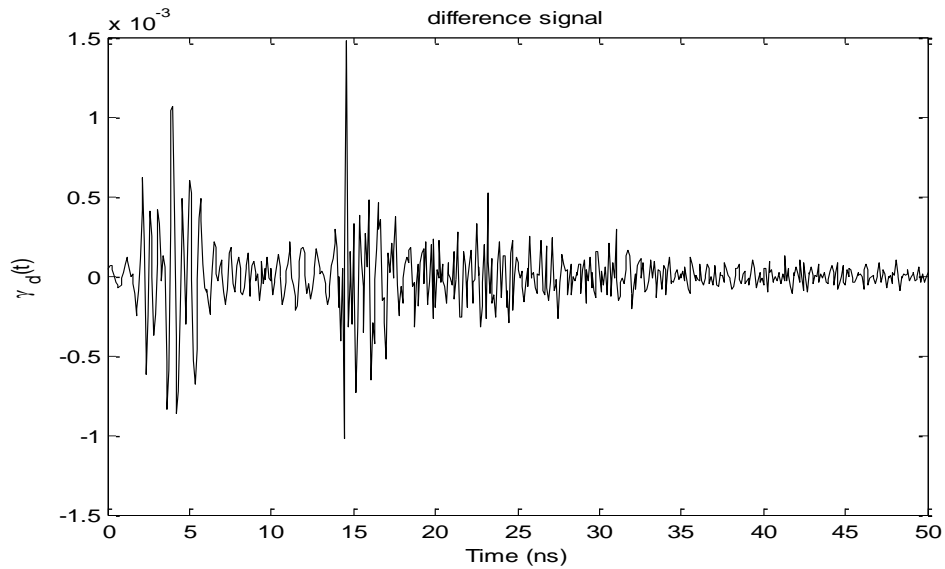


Figure 2.21: Difference of VNA signals with target and without target

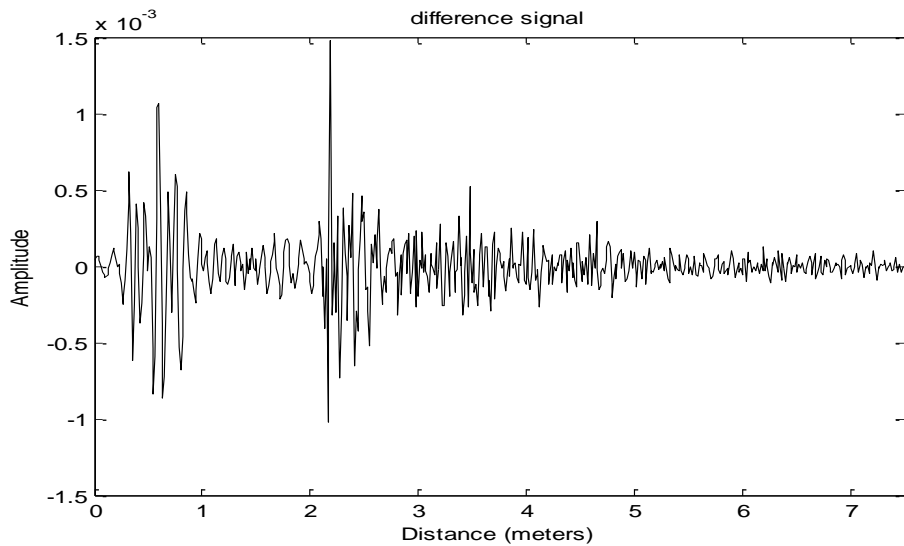


Figure 2.22: Difference of VNA signals with target and without target scattering with respect to distance

$\gamma_d(t)$ will contain information about the round trip propagation delay between the TX/RX location and the target position. From $\gamma_d(t)$, the real target location is uncertain because the signal contains multiple peaks that can be considered as false targets, generating a false target location. These false signals are generated due to the noise contribution from different sources such as the impulse response of the transmitter and receiver antennas, the antenna cross-coupling response, the transmitted and reflected medium response, the target impulse response, and the noise as explained in section 2.4.3.

Scattering Distance Calculation

After reconstructing the impulse response, the signal must be processed in order to obtain an accurate target positioning as shown in Fig. 2.23.

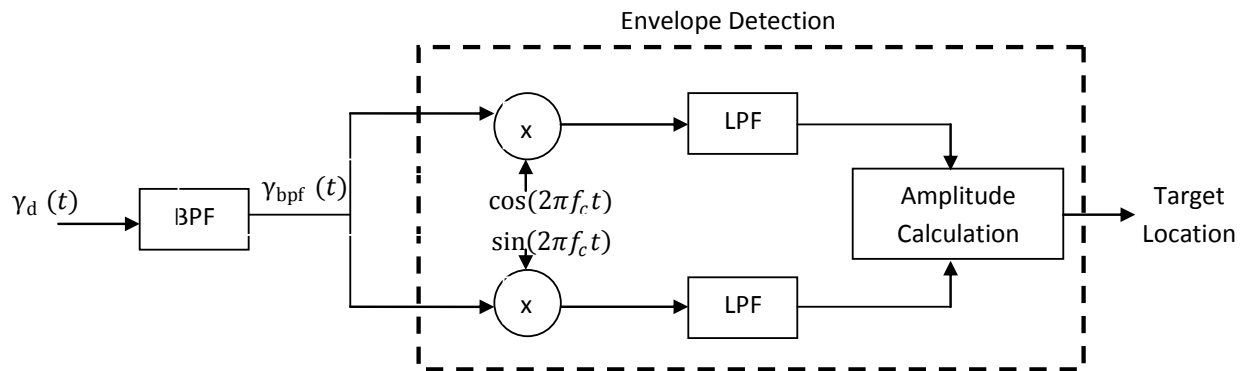


Figure 2.23: VNA impulse signal processing

This system will be explained in four different sections: 1- BPF, 2- demodulator, 3- LPF, and 4- Amplitude calculation.

1. BPF

From $\gamma_d(t)$, the signal spectrum shown in Fig. 2.24 can be calculated. From Fig. 2.24, the frequency range where most of the energy is concentrated can be found in order to design the band pass filter. If the energy is spread over the whole frequency range, a wide bandpass filter

can be designed. The filter was designed by using a Hamming window, order 100 with $F_s=12$ GHz. The filter passband was selected according to the antenna parameters. For the antennas used in our experiment, any value below 2.5 GHz could be considered noise and can be rejected. For this reason, the passband of the BPF was selected as [3.5, 5.5] GHz. The impulse response and the amplitude response of the BPF are shown in Fig. 2.25 (a) and (b). Fig. 2.25 (c) shows the signal spectrum after the BPF.

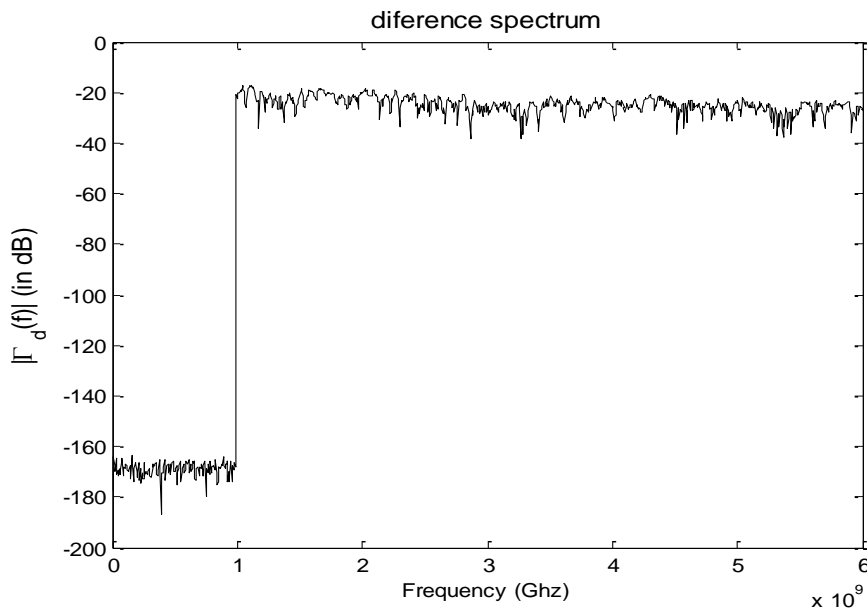
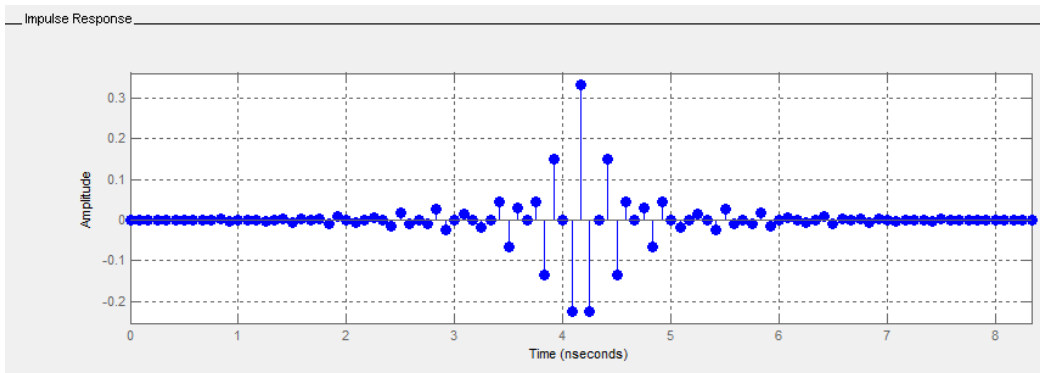
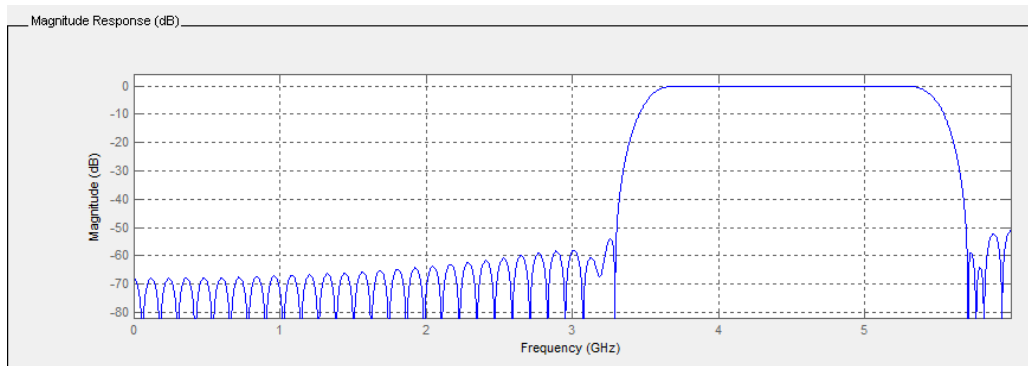


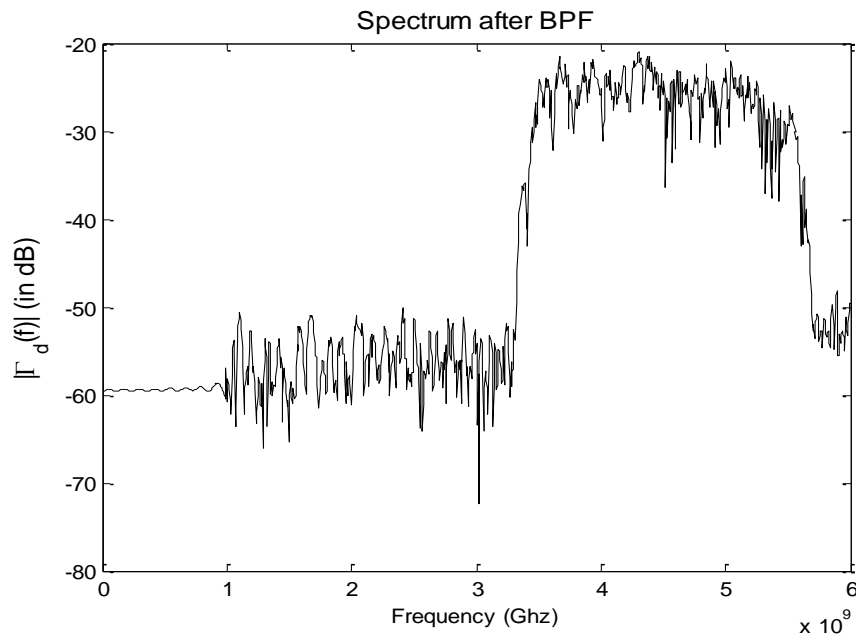
Figure 2.24: Signal difference spectrum



(a)



(b)



(c)

Figure 2.25: (a) The impulse response, (b) The magnitude response of the designed bandpass filter and (c) Signal spectrum after BPF

The resulting signal after the bandpass filter is shown in Fig. 2.26, which reveals that the noise due to the different impulse responses, described at the end of section 2.4.3, has been reduced or suppressed. The peak corresponds to the reflection from the target. Therefore, the distance can be calculated by using the round trip propagation delay. Further processing is necessary in order to obtain a smoother and enveloped signal.

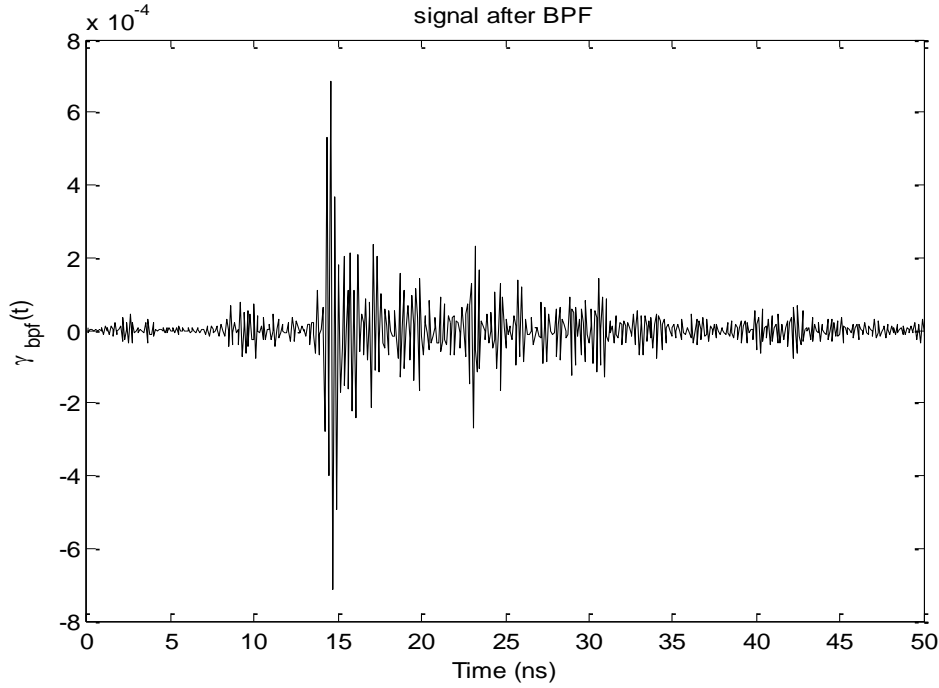


Figure 2.26: Signal after bandpass filter

2. Demodulator

Before the signal went into the demodulator, we verified the input signal where the number of coefficients remained at 1919 as shown in Fig. 2.26.

The objective of using the demodulator is to obtain an enveloped signal eliminating the noise and providing a more precise scattering location. The input value is multiplied by a cosine or a sine where the f_c in Fig. 2.23 represents the bandwidth to the center frequency of the bandpass filter, which can be calculated as follows:

$$f_c = \frac{(f_{\max BPF} - f_{\min BPF})}{2} = \frac{(5.5 - 3.5)}{2} = 1 \text{ GHz.} \quad (2.28)$$

Fig. 2.27 (a) and (b) show the cosine and sine functions that will multiply the $\gamma_{bpf}(t)$ signal. Fig. 2.27 (c) and (d) show the results after processing the signal through the demodulator (cosine and sine) before the LPF.

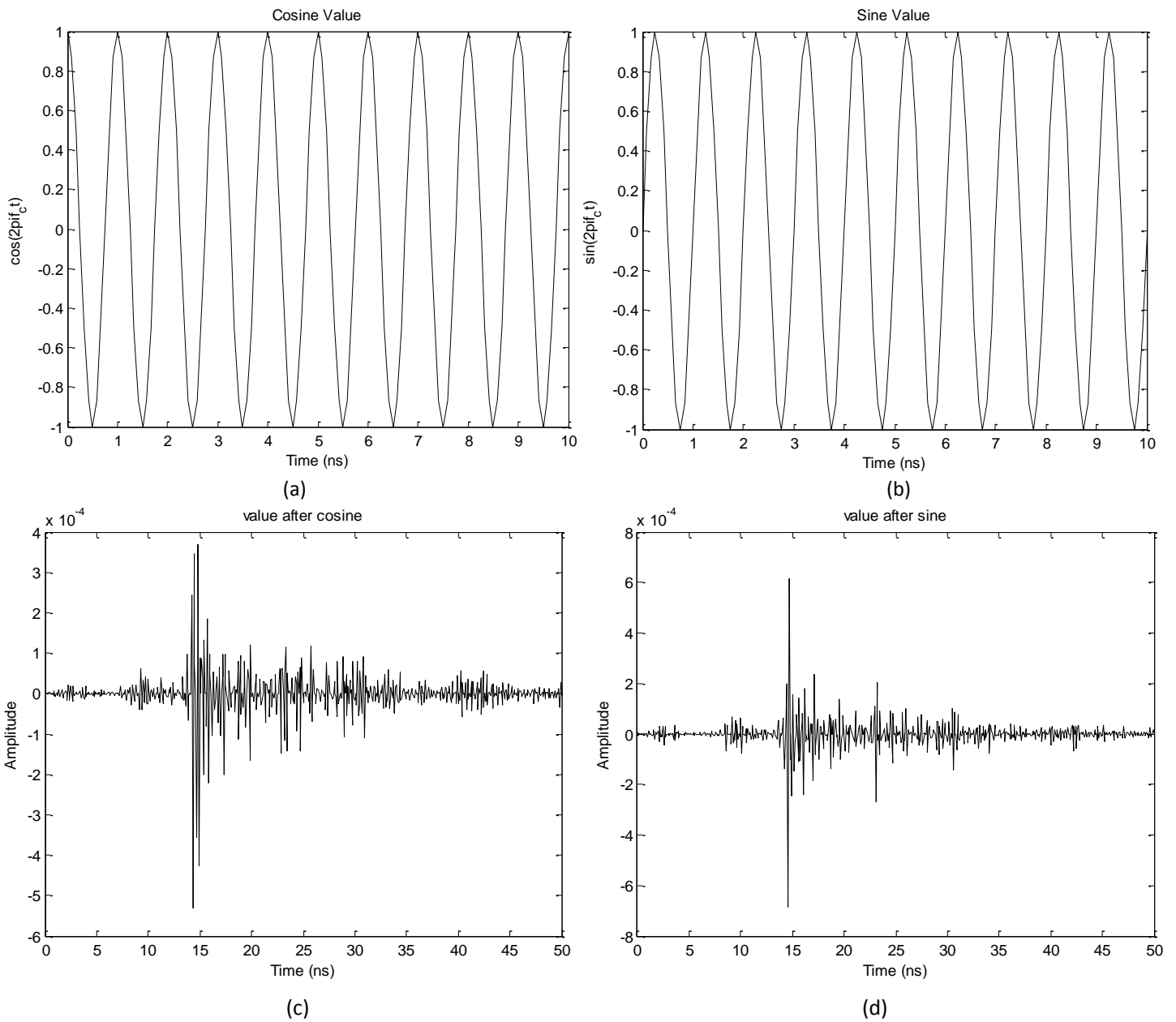


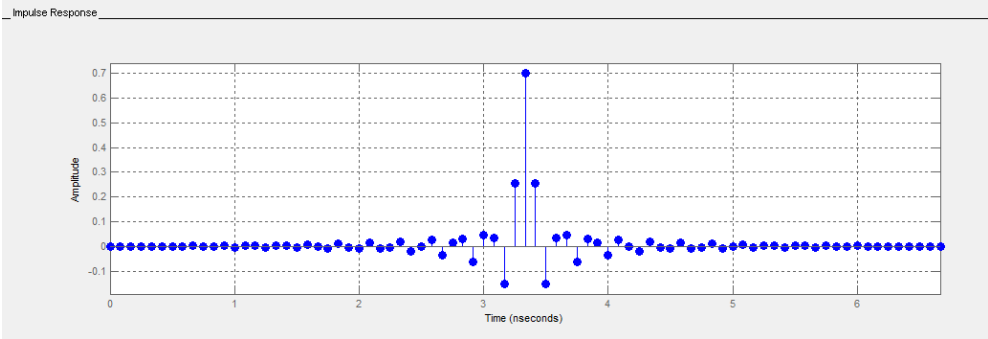
Figure 2.27: Demodulator (a) Cosine value, and (b) Sine value. (c) Signal after cosine and (d) Signal after sine.

3. LPF

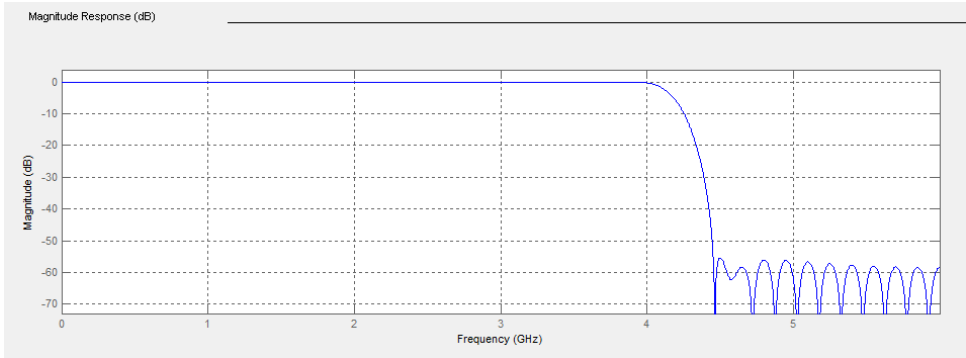
The low pass filter was designed in order to keep the low frequency components after the BPF.

The design was done by using the spectrum after the BPF shown in Fig. 2.25 (c). The filter was

designed by using a Hamming window order 80. The sampling frequency was set at $F_s=12$ GHz, and the cut frequency was set at 4.2 GHz. Fig. 2.28 (a) and (b) show the impulse response and the amplitude response of the low pass filter.



(a)



(b)

Figure 2.28: (a) The impulse response and (b) The magnitude response of the designed low pass filter

Fig. 2.29 shows the resulting signal after the LPF block shown in Fig. 2.23.

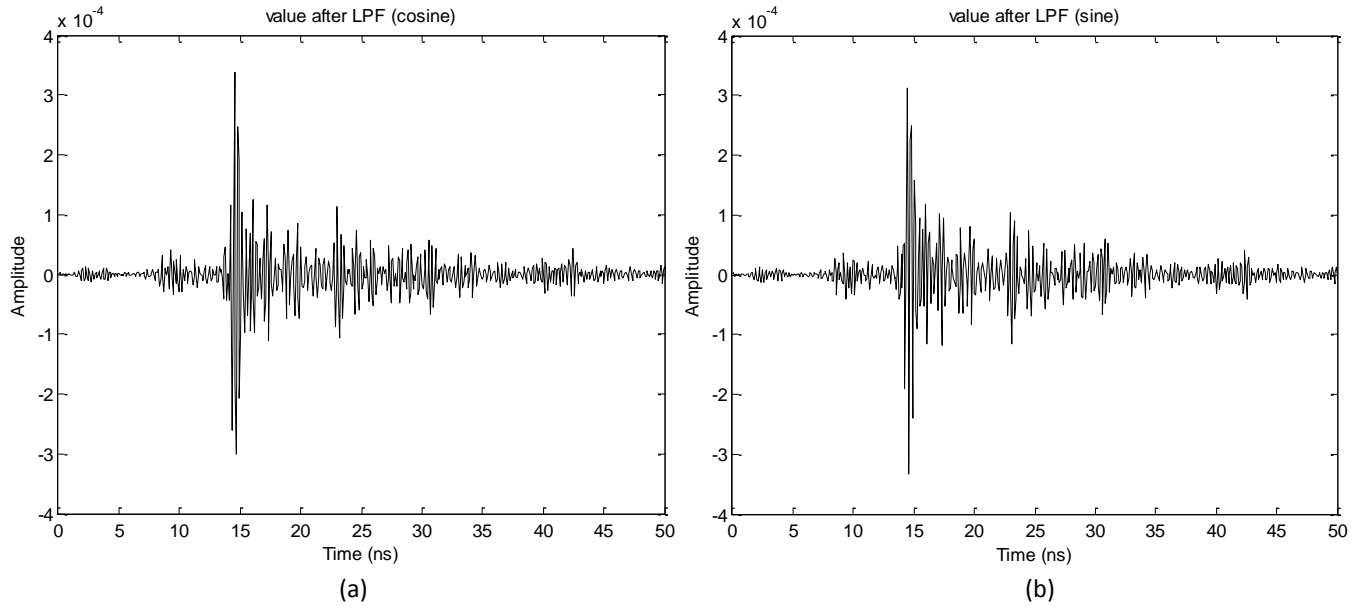


Figure 2.29: (a) Signal after LPF (cosine), and (b) Signal after LPF (sine)

4. Amplitude Calculation

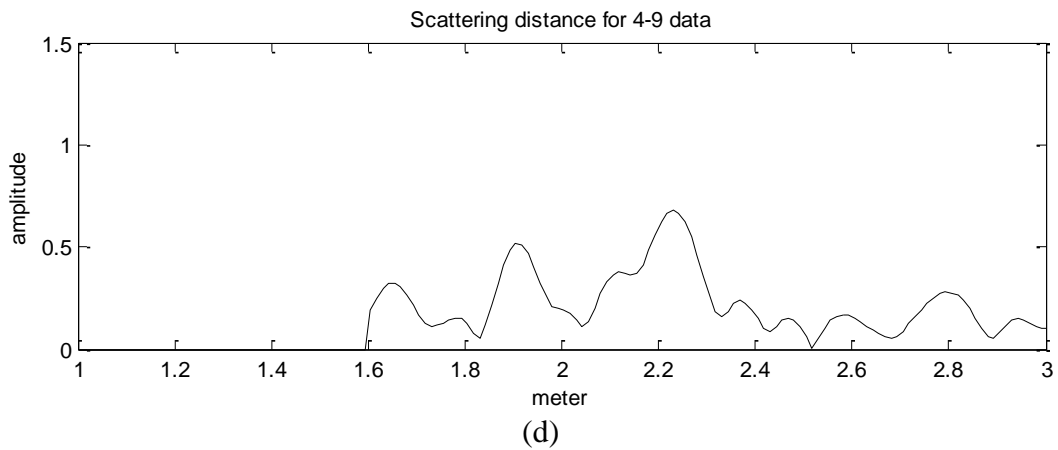
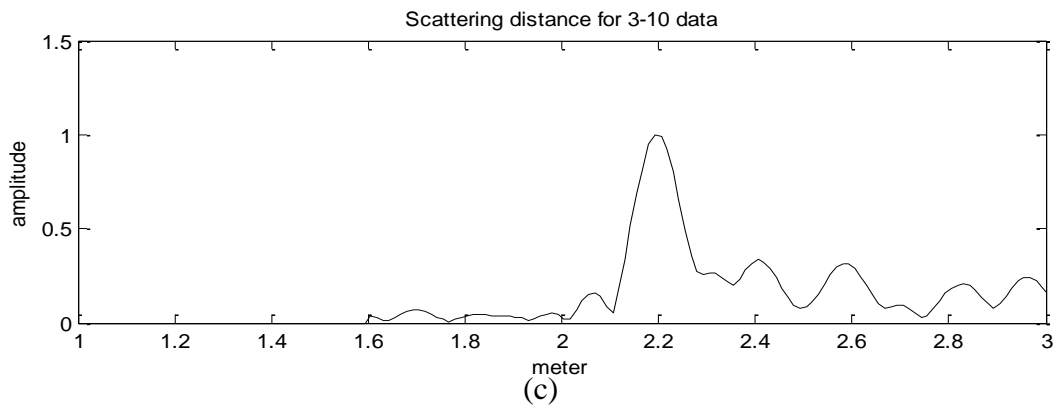
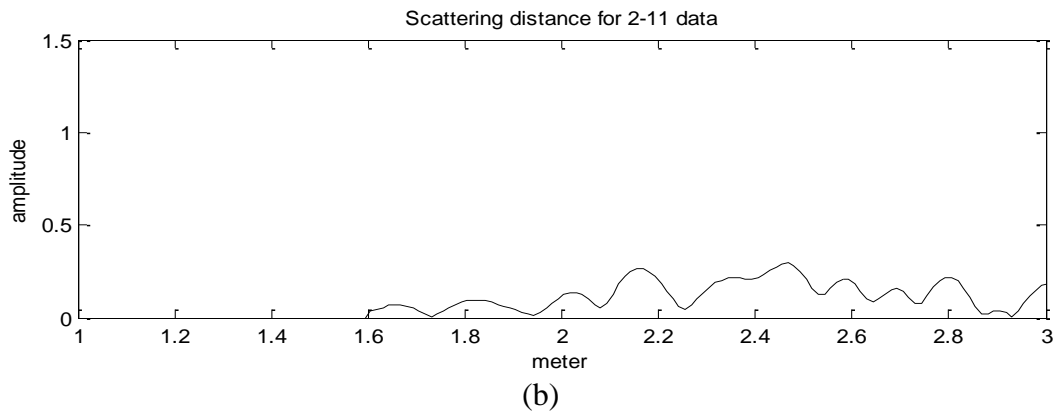
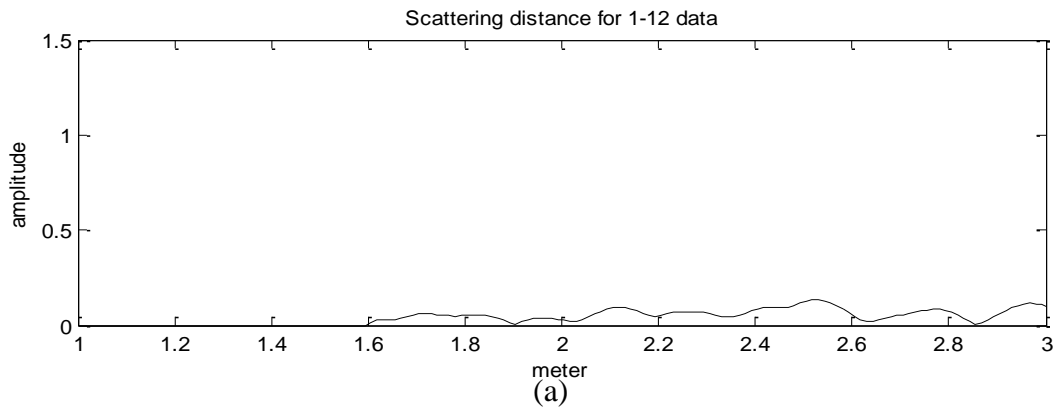
In the final module of the signal after the demodulator, the signal amplitude is obtained, providing a signal that will show clearly the location of each scattering source as shown in Fig.

2.30. The distance is calculated as follows:

$$distance = c * \frac{\Delta t}{2}, \quad (2.29)$$

where c is the speed of light, and Δt is the result of Eq. 2.27.

The processed data are normalized by the maximum value of the processed data in order to obtain amplitude values between 0 and 1. From Fig. 2.17, we can assume that any scattering below 1.6 meters should be zero because no scattering source is present between the antennas and the target.



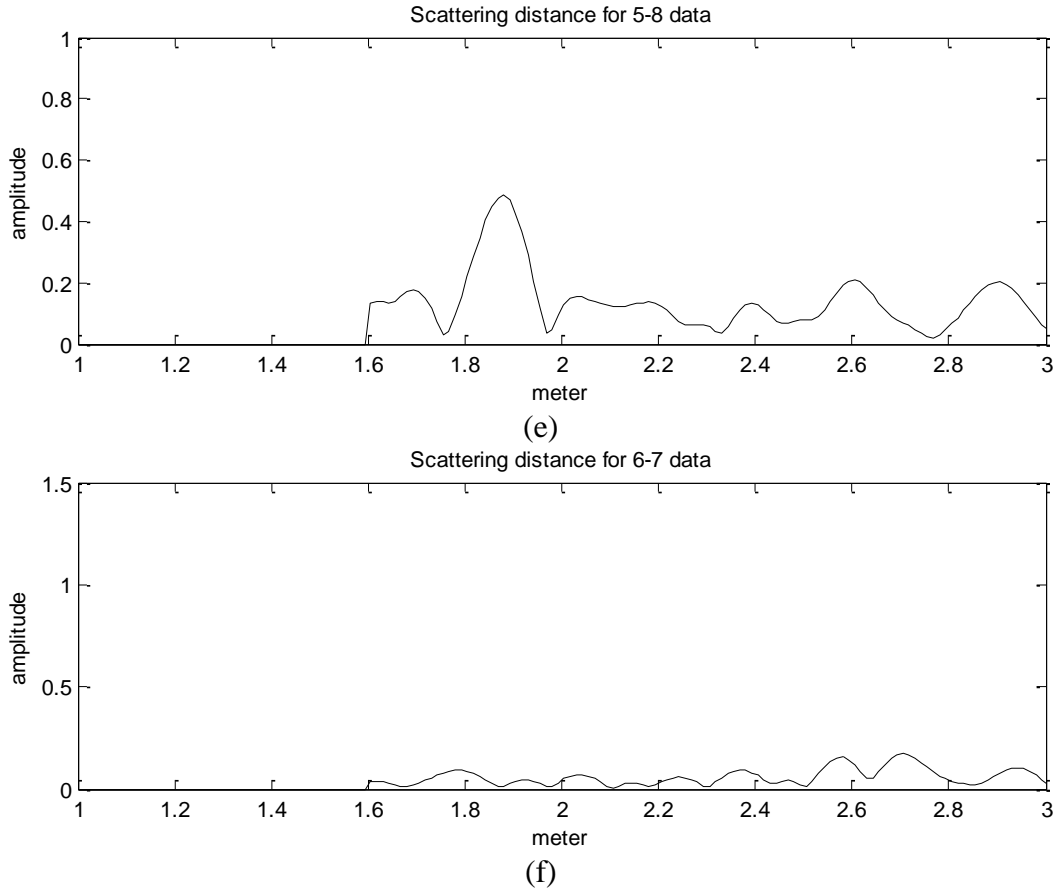


Figure 2.30: A-scan scattering images free space experiment (a) Data 1-12 antenna position, (b) Data 2-11 antenna position, (c) Data 3-10 antenna position, (d) Data 4-9 antenna position, (e) Data 5-8 antenna position, and (f) Data antenna 6-7 position.

2.4.4.3 B-Scan Imaging

A B-scan image can be generated after collecting a certain number of equidistant measurements or A-scans over the same line. The main idea of a B-scan image is to characterize a group of A-scan measurements as a function of depth or scattering distance. The six different A-scan measurements shown in Fig. 2.30 were stored in a matrix B of 112×6 . Each column was repeated 12 times, generating a 112×72 unfocused B-scan matrix B_u . The unfocused image shown in Fig. 2.31 was obtained.

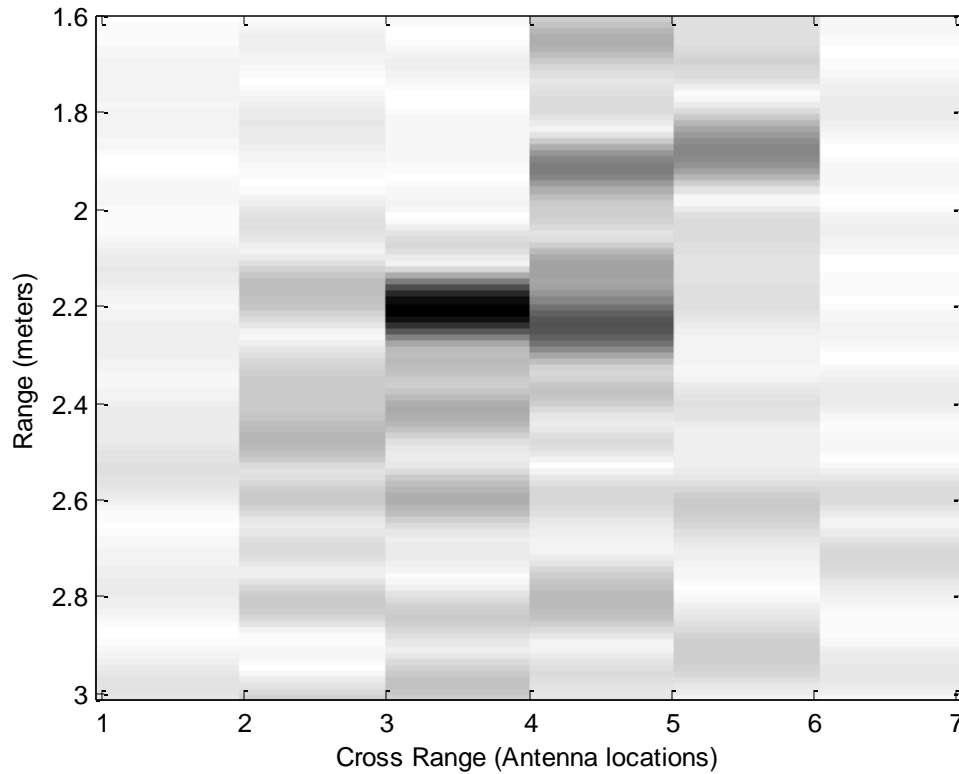


Figure 2.31: Unfocused B-scan image (obtained with schematic shown in Fig. 2.17)

In order to enhance the image quality of Fig. 2.31, the data in the horizontal direction must be resampled due to the low number of collection points (e.g. six antenna locations) and the low resolution horizontally. For this purpose, the matrix is resampled row-wise by using the function `resample(x,p,q)` where the sequence in vector `x` (e.g. row values) is resampled p/q times the original sampling. The values of `p` and `q` were defined as $p=12$ and $q=1$, so that each of the 6 measurements of matrix `B` was resampled 12 times. Matrix `B` was resampled to a new matrix `Br` of size 112 x 75, and the new image is shown in Fig. 2.32.

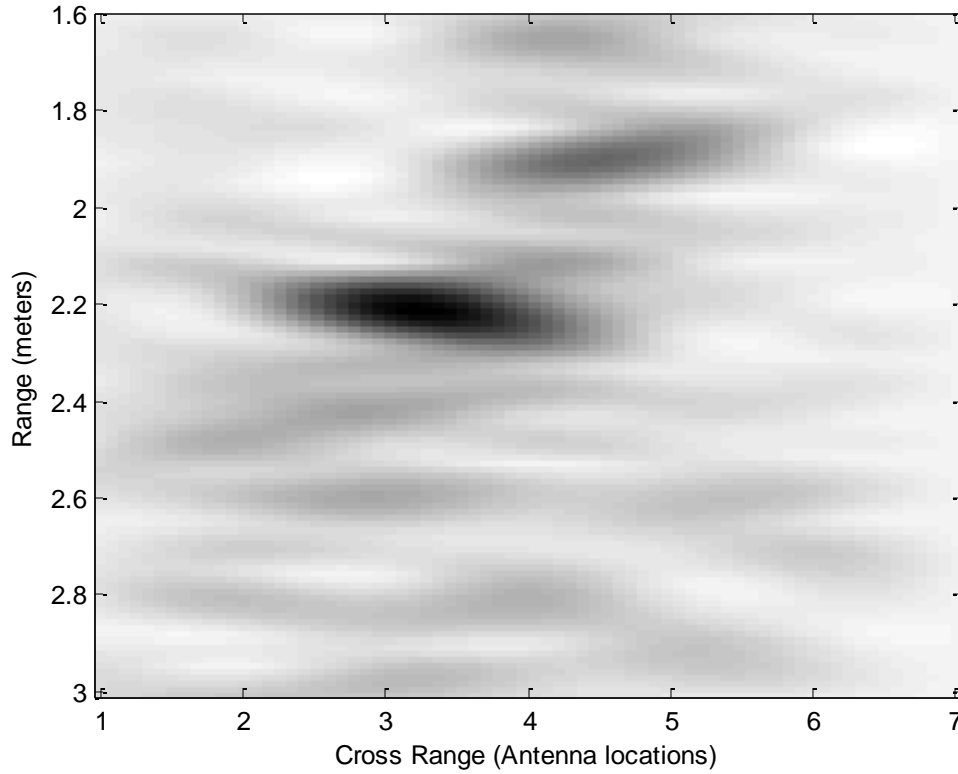


Figure 2.32: Resampled B-scan image (obtained with schematic shown in Fig. 2.17)

2.4.5 GPR Depth Estimation

In many cases, an approximate target location is known. In this case, a minimum (y_{min}) and maximum (y_{max}) target depth can be set (as shown in Fig. 2.33). The received data can be windowed, and only the data corresponding to depth in the range $[y_{min}, y_{max}]$ can be selected for accurate depth estimation. This process is repeated for N different B-scans, assuming a fixed z value for each scan. The range data are selected, based on the given information and the sampling theorem, as follows: $F_s = 2 * f_{stop}$, $\Delta t = \frac{1}{F_s}$, and $\Delta y = v * \Delta t$. By using the depth resolution (Δy), an estimated depth vector $y = (0:2001) * \Delta y$ can be calculated, and the collected data can be windowed as follows:

- (i) A B-scan matrix (z, x_n, f_m) of size $N \times M$ is considered.
- (ii) Using the approach explained in section 2.4.3, the frequency axis in matrix $N \times M$ (with $M=901$) is converted to double-sided and zero padded. The resulting matrix (z, x_n, f_q) has size $N \times Q$, where $Q=2001$.
- (iii) The 1-D IFFT with respect to f_q from (z, x_n, f_q) is calculated. The IFFT reconstructs the time domain signal for each antenna position, generating a new matrix $\gamma(z, x_n, t_q)$, with t_q having Q elements.
- (iv) By using y_{min} and y_{max} values and $\gamma(z, x_n, t_q)$, the reflected data can be filtered in between the minimum and maximum range, and the matrix $\gamma'(z, x_n, t_q)$ can be obtained:

$$\gamma'(z, x_n, t_q) = \begin{cases} \gamma(z, x_n, t_q) & \text{for } q_{min} \leq q \leq q_{max} \\ 0 & \text{otherwise} \end{cases} \quad (2.30)$$

where $q_{min} = \frac{y_{min}}{\Delta y}$ and $q_{max} = \frac{y_{max}}{\Delta y}$.

- (v) The matrix $\gamma'(z, x_n, t_q)$ is then moved back to the frequency domain by calculating 1-D FFT with respect to t_q , and a new matrix $r'(z, x_n, f_q)$ is obtained. Note that $r'(z, x_n, f_q)$ satisfies the Hermitian symmetric property with respect to the f_q dimension as shown in Fig. 2.34. For this reason, for our processing, only the first 1001 values of f_q are stored, and the rest of values are zero padded, to obtain the matrix $p(z, x_n, f_q)$.

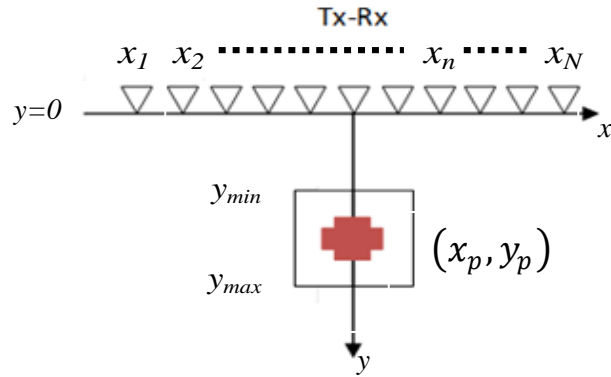


Figure 2.33: The imaging environment. x_n ($1 \leq n \leq N$) represents the TX/RX location. y_{min} and y_{max} are the minimum and maximum depth, respectively

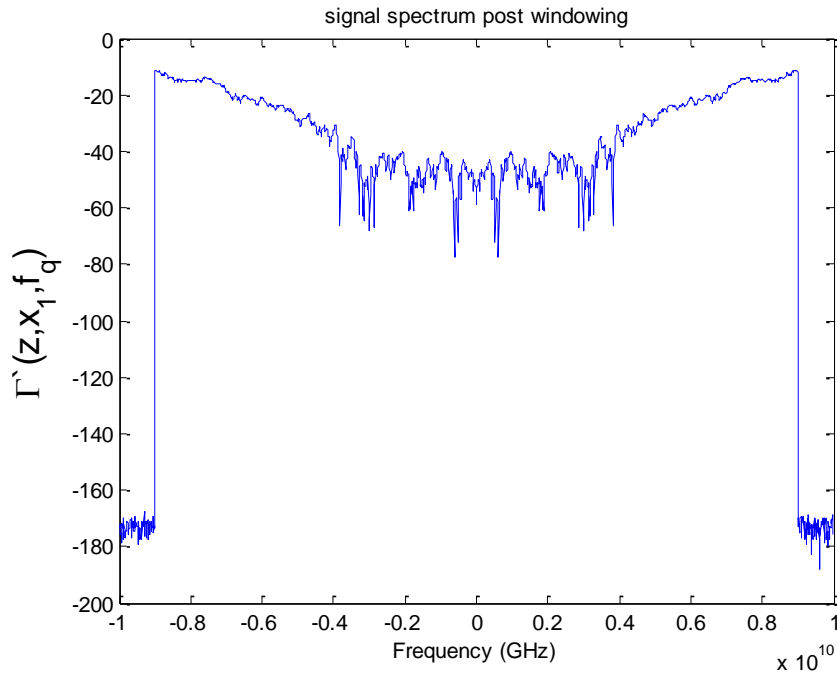


Figure 2.34: $\Gamma(z, x_1, f_q)$ spectrum post-windowing

2.4.6 Migration Imaging

2.4.6.1 Basic Migration Principle

This imaging technique was initially implemented in order to reconstruct subsurface images from some collected measurements [27], but later this technique was used in other applications such as GPR [28] and TWI [29].

The recorded data are obtained at the surface $y=0$, as shown in Fig. 2.33. (x, t) is the surface representation (i.e., at $y=0$) of a reflected wave field $P(x, t)$. For the purposes of the migration solution [29, 30], let us assume that the target is a source. The amplitude of the waves traveling back to the receivers can increase and decrease depending on the reflectivity $M(x, y)$ at each point. Let us assume the following:

$$M(x, y) = P(x, y, t = 0). \quad (2.31)$$

The above relation shows that migration is a simple mapping of the recorded data (x, t) onto the reflectivity $M(x, y)$ as follows:

$$(x, t) = P(x, y = 0, t) \xrightarrow[\text{Migration}]{} M(x, y) = P(x, y, t = 0). \quad (2.32)$$

The mapping procedure can be done by first deriving the wavefield $P(x, y, t)$ from the recorded reflected wavefield $P(x, y = 0, t)$ and substituting $t=0$ to obtain the wavefield $P(x, y, t = 0)$. With multiple receivers, the wavefield will result in a B-scan image.

2.4.6.2 Wavefield Migration Description

By using the reflected wavefield $P(x, y = 0, t)$, this wavefield can be decomposed into monochromatic waves that will be traveling at different angles from the vertical axis y . This plane wave decomposition can be performed with a 2-D Fourier transform of $P(x, y = 0, t)$, obtaining $P(k_x, y = 0, \omega)$. Consider a traveling plane wave that traveled upward from a point T at $t=0$ and reached the receiver at point G at time= t as shown in Fig. 2.35. As was explained in the explanation of the basic migration principle, the main objective is to obtain the wavefield at $t=0$. In order to achieve this objective, the energy must be returned to target T and will follow the same path used to reach the receiver. As the same path is followed, the downward continuation does not affect the horizontal wavenumber k_x .

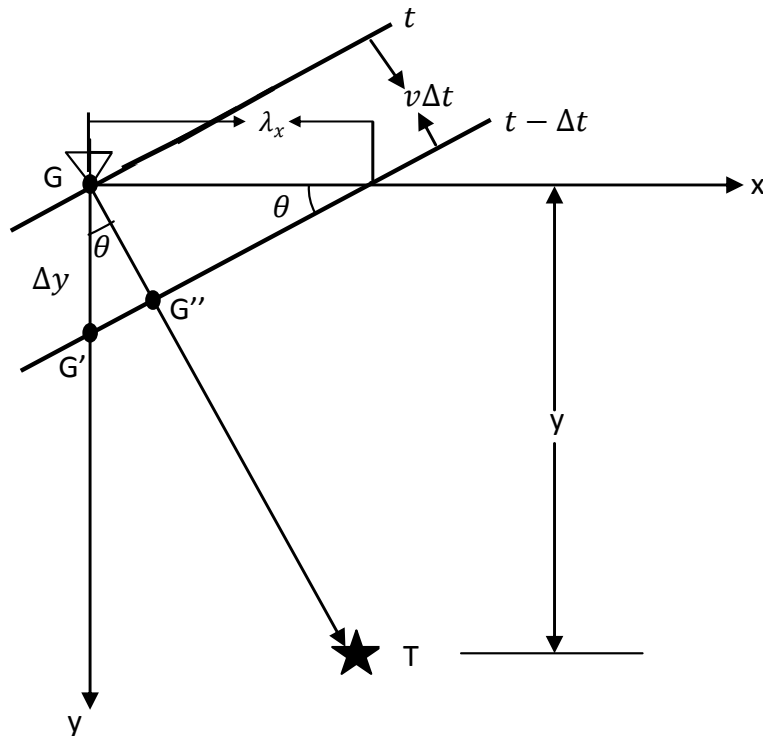


Figure 2.35: Wavefield extrapolation

If the wavefront moves to a depth $\Delta y = GG'$ and follows the ray path, the point G moves to G''. If the receiver were placed at G'', it would have received a plane wave at $t - \Delta t$, where Δt is the time difference between G and G''.

From Fig. 2.35, the following equation for Δt can be found:

$$\Delta t = \frac{\Delta y}{v} \cos \theta. \quad (2.33)$$

where v is the wave velocity.

We know the k_x and ω values for the plane wave after performing the 2-D FFT of $P(x, y = 0, t)$ with respect x and t . Suppose that the distance between G and G'' is one wavelength (λ) and that the wavefront at $t - \Delta t$ intersects the x-axis at a distance λ_x from G. Therefore, we can deduce the following equation:

$$\frac{GG''}{\lambda_x} = \frac{\lambda}{\lambda_x} = \sin \theta, \quad (2.34)$$

where $\lambda = \frac{2\pi}{\left(\frac{\omega}{v}\right)}$ and $\lambda_x = \frac{2\pi}{k_x}$, where ω/v is the wavenumber along the raypath. Substituting these values in the previous equation, we get

$$\sin \theta = \frac{vk_x}{\omega}. \quad (2.35)$$

Using a trigonometric identity, we obtain

$$\cos \theta = \sqrt{1 - \left(\frac{vk_x}{\omega}\right)^2}. \quad (2.36)$$

Substituting Eq. 2.36 into Eq. 2.33, we obtain

$$\Delta t = \frac{1}{v} \sqrt{1 - \left(\frac{vk_x}{\omega}\right)^2} \Delta y. \quad (2.37)$$

Eq. 2.37 provides a relationship between Δt and Δy . This relationship can be used to reconstruct $P(x, y, t)$ from $P(x, y = 0, t)$.

2.4.6.3 Kirchhoff Migration

Kirchhoff migration was introduced for seismic imaging purposes [31], but its applications have been expanded to other areas such as TWRI and GPR [32, 33].

The Kirchhoff migration algorithm [28, 33-35] is based on the integral form of the scalar wave equation. The solution to this integral is based on Green's function and will represent the scalar wavefield for all times at all locations as is shown in the following equation:

$$f(r, t) = \frac{1}{2\pi v_m} \frac{\partial}{\partial y} \int_{t'} \oint_S \psi(r', t') g(r, t; r', t'), \quad (2.38)$$

where $\psi(r', t')$ is the scalar wavefield at point r' and time t' and $g(r, t; r', t') = \frac{\delta(t-t'+R/v_m)}{R}$ represents the Green function.

Eq. 2.38 can be simplified taking the derivative with respect z and using the shifting property of the Green's function, obtaining the following expression:

$$f(r, t) = \frac{1}{2\pi v_m} \oint_S \frac{\partial}{\partial t'} \psi(r', t + R/v_m) \frac{\cos \theta}{R} dS, \quad (2.39)$$

where S is the surface that contains all the sources or targets, v_m is the wave velocity in the media, R is the distance between the TX/RX location to a point (x, y) , and θ is the angle between the y axis and R from the scenario shown in Fig. 2.36.

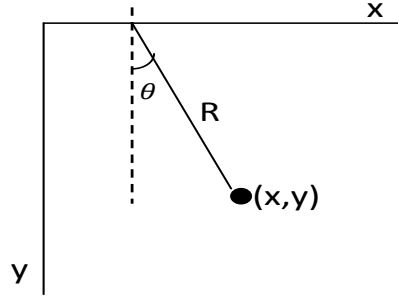


Figure 2.36: Kirchhoff scattering point scenario

Kirchhoff's integral can be interpreted as follows:

1. Look at a possible target (x,y) in the surface of study.
2. As the wave velocity in the media is known, find the apex of the diffraction hyperbola generated by target (x,y) in the time section.
3. Sum along the generated hyperbola according to Kirchhoff's integral.

Although from the previous steps, it is possible to migrate to the right depth, Kirchhoff's migration is more accurate because of the obliquity factor $(\cos \theta)$ and the derivative of the Green's function along the y axis.

By assuming the exploding reflector model, where the targets are assumed as sources and the wave travels only from the target to the TX/RX, the image can be reconstructed at $t=0$ as follows:

$$f(x, y) = \frac{1}{2\pi v_m} \oint_S \frac{\partial}{\partial t'} \psi(x', y' = 0, R/v_m) \frac{\cos \theta}{R} dS. \quad (2.40)$$

2.5 Ground Penetrating Radar Signal Processing

Yigit et al. [36] proposed the use of synthetic aperture radar (SAR) principles to obtain a GPR B-scan image to localize buried targets. SAR is a very efficient system used in space and

airborne operations, where a flight path is used to simulate an extremely large antenna. SAR imaging is a technique based on migration, performing spatial positioning, and focusing.

The technique proposed in [36] assumes that the TX/RX signal travels through a homogeneous medium. The VNA data collection is performed by using the method explained in section 2.4.6, where data are collected at N different antenna locations and m different frequencies $\{f_m, 1 \leq m \leq M\}$. The collected data for one B-scan will have a size of $M \times N$. The VNA output can be represented as the sum of the contribution from all scatterers in the scene. Let $\{\tau_{n,p}, 1 \leq n \leq N\}$ denote the round trip propagation delay between the n -th antenna and the p -th target (see Fig. 2.33). The $\tau_{n,p}$ can be calculated as follows:

$$\tau_{n,p} = \frac{2d_{n,p}}{v} = \frac{2\sqrt{y_p^2 + (x_a^n - x_p)^2}}{v}, \quad (2.41)$$

where $d_{n,p}$ is the distance between the n -th antenna at location $(x_a^n, 0)$ and the p -th target at location (x_p, y_p) , and v is the signal propagation speed.

The VNA output corresponding to n -th antenna and frequency f_m can be expressed as follows:

$$\begin{aligned} g_{pr}(n, m) &\cong \sum_{p=0}^{P-1} \sigma_p \exp \{-j2\pi f_m \tau_{n,p}\} \\ &= \sum_{p=0}^{P-1} \sigma_p \exp \left\{ -jk_m \left(2\sqrt{y_p^2 + (x_a^n - x_p)^2} \right) \right\}, \end{aligned} \quad (2.42)$$

where v is the velocity in the media, $k_m = \frac{2\pi f_m}{v}$ is the wavenumber corresponding to m -th frequency, and σ_p is the reflectivity of p -th target. The VNA output (n, m) is a complex value.

The VNA output is processed by using the f-k domain SAR imaging technique in order to obtain a B-scan image $\theta(x, y)$ which can be represented as follows:

$$\theta(x, y) = \begin{cases} 1 & \text{if } (x, y) \in \{(x_p, y_p), 1 \leq p \leq P\} \\ 0 & \text{otherwise} \end{cases}. \quad (2.43)$$

The schematic of the technique is shown in Fig. 2.37. The three modules in the technique are explained below.

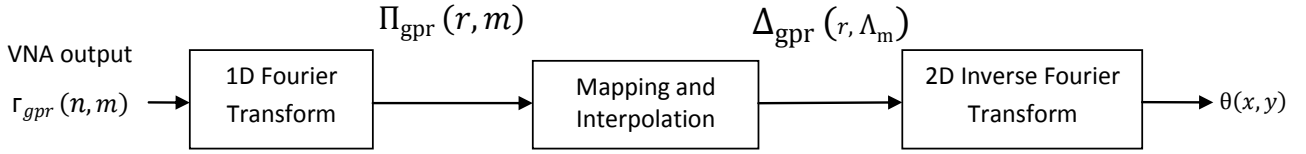


Figure 2.37: Existing SAR imaging technique

Module 1: 1D Fourier Transform

Calculating 1-D Discrete Fourier Transform along the x -axis, we obtain the DFT, for a given f_m value, in terms of the spatial frequency Ω_r , as follows:

$$\begin{aligned} \Pi_{gpr}(r, m) &= \mathfrak{F}\{gpr(n, m), 0 \leq n \leq N-1\} \quad 0 \leq r \leq N-1 \\ &= \sum_{n=0}^{N-1} gpr(n, m) \exp\left(\frac{-j2\pi nr}{N}\right). \end{aligned} \quad (2.44)$$

As Table 2.2 shows, the spatial frequency Ω_r and the index r are directly dependent.

Substituting $gpr(n, m)$ from Eq. 2.42 in Eq. 2.44, we obtain:

$$\begin{aligned} \Pi_{gpr}(r, m) &= \sum_{p=0}^{P-1} \sum_{n=0}^{N-1} \sigma_p \exp\left\{-jk_m \left(2\sqrt{y_p^2 + (x_a^n - x_p)^2}\right)\right\} \exp\left(\frac{-j2\pi nr}{N}\right) \quad (2.45) \\ &= \sum_{p=0}^{P-1} \sigma_p \sum_{n=0}^{N-1} \exp\left\{-jk_m \left(2\sqrt{y_p^2 + (x_a^n - x_p)^2}\right)\right\} \exp\left(\frac{-j2\pi nr}{N}\right) \\ &= \sum_{p=0}^{P-1} \sigma_p \sum_{n=0}^{N-1} \exp\left\{-jk_m \left(2\sqrt{y_p^2 + (x_a^n - x_p)^2}\right) - \frac{j2\pi nr}{N}\right\} \end{aligned}$$

$$\begin{aligned}
&= \sum_{p=0}^{P-1} \sigma_p \sum_{n=0}^{N-1} \exp \left\{ j \left[-\frac{2\pi f_m}{c} \left(2\sqrt{y_p^2 + (x_a^n - x_p)^2} \right) - \frac{2\pi nr}{N} \right] \right\} \\
&= \sum_{p=0}^{P-1} \sigma_p \sum_{n=0}^{N-1} \exp \left\{ j\omega_m \left[-\frac{2}{c} \sqrt{y_p^2 + (x_a^n - x_p)^2} - \frac{2\pi nr}{Nvk_m} \right] \right\} \\
&= \sum_{p=0}^{P-1} \sigma_p \sum_{n=0}^{N-1} \exp \{ j\omega_m [h(n)] \} \\
&= \sum_{p=0}^{P-1} \sigma_p I.
\end{aligned}$$

Eq. 2.45 represents the 1-D DFT along the x -axis of Eq. 2.42 and is represented by I in the final representation of $\Pi_{\text{gpr}}(r, m)$ shown before. For further processing, a complete expression in terms of wavenumber k_m and the spatial frequencies along the x -axis (Ω_r) and y axis (Λ_m) must be obtained. This expression denotes that

$$\Lambda_m = \sqrt{4k_m^2 - \Omega_r^2}. \quad (2.46)$$

In order to achieve the desired expression, the method of stationary phase solution must be used in order to obtain a general expression in terms of the desired spatial frequencies.

Table 2.2: DFT index and DTFT frequency values in x direction

DFT index, r	Spatial frequency in x direction $\Omega_r = 2\pi r/N$
0	0
1	$2\pi/N$
2	$4\pi/N$
⋮	⋮
N	$2\pi(N-1)/N$

Eq. 2.45 is solved by using the method of stationary phase [37], which approximates the Fourier transform and finds a simpler expression of an integral of the form:

$$I(x) = \int_a^b g(t) \exp [jxh(t)] dt, \quad (2.47)$$

where $g(t)$ and $h(t)$ are real value functions of a real variable t , and x is a real positive parameter. When the x value increases, the integrand becomes very oscillatory, and $I(x)$ will be zero for most t values in the range $[a, b]$. In order to solve this integral, the t values where $h'(t) = 0$ must be found. Supposing that there is a unique $t = t_0$ value such that $h'(t_0) = 0$, then $h''(t_0)$ must be defined as either > 0 or < 0 in order to choose the right answer from these two cases.

Case 1- $h''(t_0) > 0$

$$I(x) \approx g(t_0) \exp \left[jxh(t_0) + j \frac{\pi}{4} \right] \sqrt{\frac{2\pi}{xh''(t_0)}} \quad (2.48)$$

Case 2- $h''(t_0) < 0$

$$I(x) \approx g(t_0) \exp \left[jxh(t_0) + j \frac{\pi}{4} \right] \sqrt{\frac{2\pi}{x|h''(t_0)|}} \quad (2.49)$$

For the method of stationary phase definition, Eq. 2.45 is expressed as follows in a continuous form:

$$I = \int_{-\infty}^{\infty} \exp [j\omega_m h(x)] dx = \int_{-\infty}^{\infty} \exp \left[j\omega_m \left(-\frac{2}{c} \sqrt{y_p^2 + (x - x_p)^2} - \frac{k_x x}{ck_m} \right) \right] dx. \quad (2.50)$$

Following the process explained before, the instantaneous frequency of the phase function must be equated to zero, as shown in Eq. 2.51:

$$\frac{dh(x)}{dx} = \frac{d}{dx} \left[-\frac{2}{c} \sqrt{y_p^2 + (x - x_p)^2} - \frac{k_x x}{ck_m} \right] = 0, \quad (2.51)$$

which yields the following solution after deriving the expression $h(x)$ with respect to x :

$$2k_m \sin\theta_p(x_0) = k_x. \quad (2.52)$$

This equation implies that there exists one value $x = x_0$ such that $h'(x_0)=0$:

$$x_0 = y_p - \frac{k_x x_p}{\sqrt{4k_m^2 - k_x^2}}. \quad (2.53)$$

In order to find the correct solution $h''(x_0)$ must be established as either > 0 or < 0 as follows:

$$h''(x) = \frac{2\cos^2\theta_p(x)}{c\sqrt{y_p^2 + (x - x_p)^2}}. \quad (2.54)$$

By replacing x with x_0 it is possible to find that $h''(x_0) > 0$; therefore, the solution to I is

$$I = \int_{-\infty}^{\infty} \exp [j\omega_m h(x)] dx \approx \exp \left[jxh(x_0) + j\frac{\pi}{4} \right] \sqrt{\frac{2\pi}{xh''(x_0)}}. \quad (2.55)$$

By using this solution, the Fourier transform of $g_{pr}(k_x, m)$ with respect to x can be expressed as follows:

$$\Pi_{gpr}(k_x, m) = \frac{\exp\left(-j\frac{\pi}{4}\right)}{\sqrt{4k_m^2 - k_x^2}} \sum_{p=0}^{P-1} \sigma_p \exp \left\{ -jk_x x_p - j\sqrt{4k_m^2 - k_x^2} y_p \right\}. \quad (2.56)$$

In SAR image processing, the resulting amplitude ratio $\frac{\exp(-j\frac{\pi}{4})}{\sqrt{4k_m^2 - k_x^2}}$ is neglected, and the following

equation is derived:

$$\Pi_{gpr}(k_x, m) = \sum_{p=0}^{P-1} \sigma_p \exp \left\{ -jk_x x_p - j\sqrt{4k_m^2 - k_x^2} y_p \right\}. \quad (2.57)$$

This equation can be expressed in a discrete form as shown in Eq. 2.58:

$$\Pi_{\text{gpr}}(r, m) = \sum_{p=0}^{P-1} \sigma_p \exp \left\{ -j \left(\frac{2\pi r}{N} \right) x_p - j \sqrt{4k_m^2 - \left(\frac{2\pi r}{N} \right)^2} y_p \right\}. \quad (2.58)$$

Module 2: Mapping and Interpolation

Now this data must be mapped in the $\Omega_r - \Lambda_i$ domain. For this purpose, the following spatial-frequency mapping equation must be used to map the values from $\Pi_{\text{gpr}}(r, m)$ to $\Delta_{\text{gpr}}(r, \Lambda_m)$:

$$\Lambda_m = \sqrt{4k_m^2 - \Omega_r^2}, \quad (2.59)$$

where Ω_r takes the values shown in Table 2.

$$\Delta_{\text{gpr}}(r, \Lambda_m) = \sum_{p=0}^{P-1} \sigma_p \exp \{ -j\Omega_r x_p - j\Lambda_m y_p \} \quad (2.60)$$

The mapped data in the spatial domain is unevenly spaced due to the nonlinear behaviour of Eq. 2.59. In order to use IFFT, the data must be evenly spaced. Therefore, an interpolation procedure of $\Delta_{\text{gpr}}(r, \Lambda_m)$ is done.

Module 3: 2D Fourier Transform

The final focused 2-D B-scan GPR image is obtained after taking the 2-D IFFT of Eq. 2.60 as follows:

$$\theta(x, y) = \frac{1}{\sqrt{MN}} \sum_{m=0}^{M-1} \sum_{q=-N}^N \frac{\Delta_{\text{gpr}}(r, \Lambda_m)}{P(\omega)} \exp \{ -j\Omega_r x - j\Lambda_m y \}, \quad (2.61)$$

where $P(\omega) = 1$ in the case of VNA over all the frequencies of interest.

2.6 Backprojection Filtering

Backprojection is a reconstruction technique which can be used to reconstruct a 2-D image by combining several 1-D projections $g(\rho_1, \theta_1)$ from different directions θ_k . This process is repeated k times and increments the θ_k value between $180 < \theta_k \leq 0$ with a normal vector ρ with respect to the beam propagation. $g(\rho, \theta_k)$ is the complete projection composed of multiple single points. All points of the obtained backprojections are added together, and the target image is reconstructed as shown in Fig. 2.38.

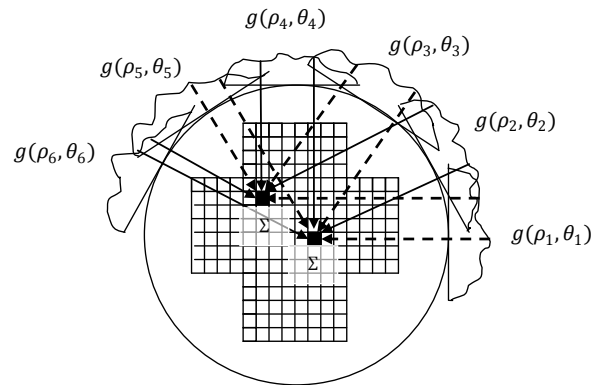


Figure 2.38: Backprojection image reconstruction

The following example of backprojection was taken from [42] and shows the reconstruction of a possible target by using the backprojection technique at different angles before filtering:

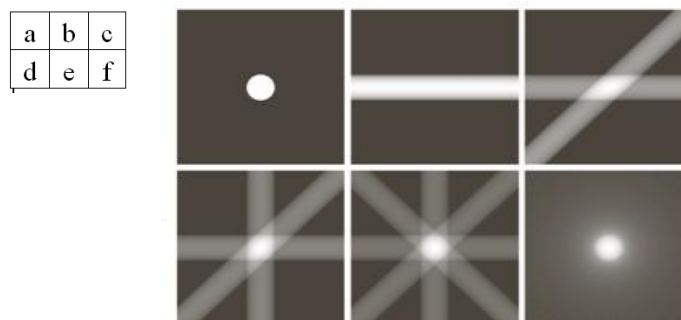


Figure 2.39: (a) Flat region showing a simple object. (b-e) Reconstruction using 1, 2, 3, and 4 backprojections 45° apart. (f) Blurred reconstruction with 32 backprojections 5.625° apart.

Filtering after Backprojection image extraction technique has been implemented recently in Computed Tomography (CT) images [42]. The main objective of this technique is to restore any degradation caused by the reconstruction process.

2.6.1 Image Filtering

From backprojection theory, a single backprojection at an angle θ is defined as

$$\hat{f}_\theta(x, z) = g(x \cos \theta + z \sin \theta, \theta). \quad (2.62)$$

The resulting image is obtained after integrating over all the back projected images in order to get the addition of all the projections that pass through the point (x, z) :

$$\hat{f}(x, z) = \int_0^\pi \hat{f}_\theta(x, z) d\theta. \quad (2.63)$$

The backprojected image is a blurred version of the desired image. For this reason, a filtering process is used to remove the blur. In the following step, the image is filtered in the Fourier domain by using a 2-D filter. The 2-D filter is defined as follows:

$$h(x, z) = \sqrt{x^2 + z^2} \quad \leftrightarrow \quad H(k_x, k_z) = \sqrt{k_x^2 + k_z^2}. \quad (2.64)$$

The filter is applied in the Fourier domain. Therefore, a 2D Fourier transform of $\hat{f}(x, z)$ must be applied to obtain $\hat{F}(k_x, k_z)$. The Fourier coefficients are filtered, and then a 2D IFFT is applied to obtain the restored image $f_b(x, z)$:

$$\hat{F}(k_x, k_z) = \int_{-\infty}^{\infty} \int_{-\infty}^{\infty} \hat{f}(x, z) e^{-j2\pi(k_x x + k_z z)} dx dz \quad (2.65)$$

$$f_b(x, z) = \int_{-\infty}^{\infty} \int_{-\infty}^{\infty} \sqrt{k_x^2 + k_z^2} \hat{F}(k_x, k_z) e^{j2\pi(k_x x + k_z z)} dk_x dk_z. \quad (2.66)$$

The discrete representation of Eq. 2.66 is as follows:

$$f_b(x, z) = \sum_{r=0}^{R-1} \sum_{i=0}^{I-1} \sqrt{k_x(r, i)^2 + k_z(r, i)^2} \hat{F}(k_x(r, i), k_z(r, i)) e^{j2\pi\left(\frac{k_x(r, i)x}{R} + \frac{k_z(r, i)z}{I}\right)}. \quad (2.67)$$

2.6.2 Backprojection in Radar applications

Backprojection image formation in radar applications is applied as is explained in the following steps:

- (i) Supposing there are N antenna locations and the area of study is divided in $I \times J$ points, producing a (x_I, y_J) pixels image of reflectivity.
- (ii) Considering the received signal from one target at two different antenna locations n_1 and n_2 as shown in Fig. 2.40 (a), where r_1 and r_2 correspond to the distance between the target and each antenna location .
- (iii) From the radar to target scenario, it is possible to find the distances r_1 and r_2 as a function of time using the following equation and as shown in Fig. 2.40 (b):

$$t_n = \frac{2r_n}{v} \quad (2.68)$$

where v is the wave velocity in the media.

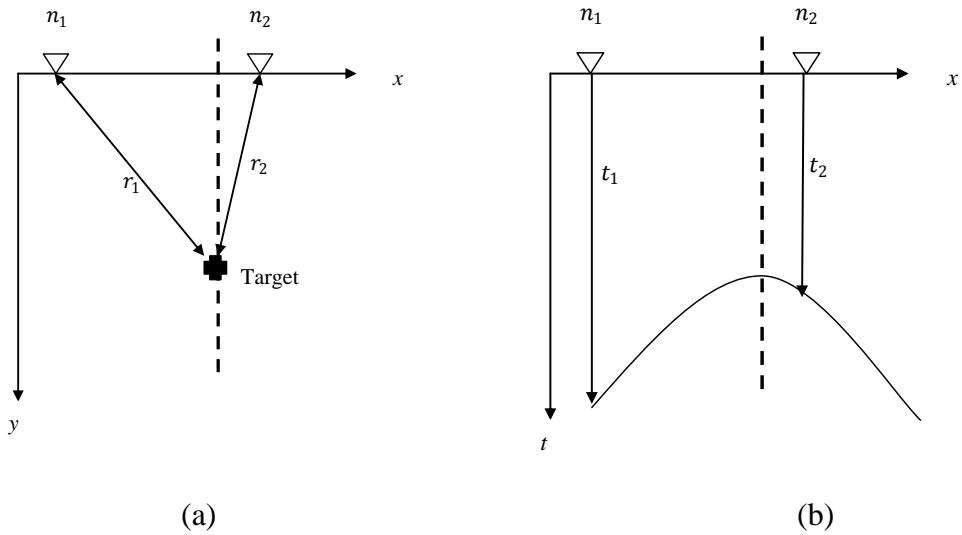


Figure 2.40: (a) Radar to target distance scenario, (b)Radar to target distance as function of time

- (iv) The reflection source can be located on a semicircle around each antenna location with radius $r_n = \frac{v \cdot t_n}{2}$, where t_n is the time delay calculated in step (iii) for each antenna position. A semicircle with radius r_1 and r_2 are generated as individual images. When the two generated images are overlapped and added, the section where the semicircles overlap will show a strong reflection while the others can be considered as noise and blurring as shown in Fig. 2.41.

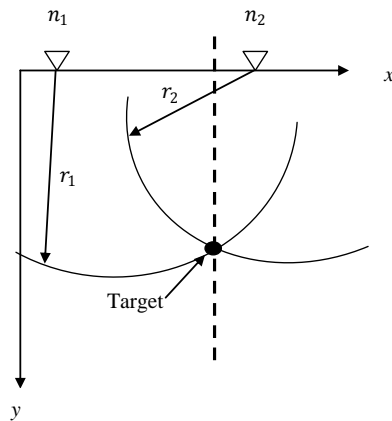


Figure 2.41: Image reconstruction

The resulting backprojected image shows some blurring around the scattering source, for this purpose the filtered backprojection technique must be applied.

2.7 Summary

This chapter began by providing a brief history of how and why radars were initially invented. Next, the principles of radar operation were explained. A section explaining the wave propagation principles was included to explain how waves propagate and react in different environments. Radar image formation is the main topic in this thesis. Thus, we explained in detail how radars transmit and receive a signal back and how the time difference between the transmission and reception can be calculated. As radar technology is very expensive and is not accessible to everyone, we had to use a different device to perform as a radar. VNA was the device used to simulate the radar signals. For this reason, a section of this chapter described in detail how VNA operates. Acquired VNA signals require some pre-processing before they can be processed. Section 2.4.3 described the signal pre-processing steps that have to be followed in order to have a signal ready to be processed and interpreted. Section 2.4.4 explained the different ways acquired data can be interpreted. Section 2.4.5 explained how the collected data can be windowed by estimating a minimum and maximum depth. Section 2.4.6 described the migration principles, in order to explain the objective of migrating a signal theoretically and physically. This explanation was followed by a complete description of how the Kirchhoff migration works. Section 2.5 described the existing GPR technique that was the basis for our proposed technique, which is explained in the following chapter. Section 2.6 described the backprojection image reconstruction and the filtering after backprojection procedure to reduce any blurring generated

during the reconstruction process. It includes an explanation of how the backprojection technique is used in radar applications.

Chapter 3

Proposed Modified F-K (MFK) focusing technique

A review of radar-based subsurface and through-wall imaging techniques have been presented in chapter 2. In this chapter, we present the proposed radar imaging technique whose main objective is to improve the target image resolution compared to other existing techniques. In section 3.1, the proposed modified F-K migration technique is presented. The proposed technique is divided into five different modules that are explained through section 3.1 to section 3.6. The technique takes as an input a 2-D array of reflection coefficients as described in section 2.4.4. In section 3.2, the energy of the collected data at each antenna position is focused on a given point. In section 3.3, the focused data is windowed using the Hermitian and Fourier transform properties. The windowed data is processed in section 3.4, using the F-K migration technique, which will drop as a result a 2-D B-scan matrix that contains the migrated data with respect the possible scattering depth. The process done up to this point is repeated for N different z positions, obtaining N different B-scan matrices in section 3.5. A sectional target image is reconstructed from all the resulting B-scan matrices. In section 3.6, a backprojection filter is used in order to increase target details and reduce noise in the image.

3.1 Schematic of the focusing technique

In section 2.4.6 we introduced the migration principles and the Kirchhoff migration technique. F-K migration is another popular technique that has been used for target location in ground penetrating radar (GPR) applications. One of the limitations in this application is that GPR typically assumes a homogeneous medium [36]. In section 2.4, it was discussed that this assumption is not satisfied in many situations where the antennas are not located close to the ground and the signal traveling path is affected by the change of media. To improve the detection performance, the proposed technique assumes a two-media environment (e.g., air-sand, wall-air). The schematic of the proposed MFK focusing technique is shown in Fig. 3.1. The description of each module is given below.

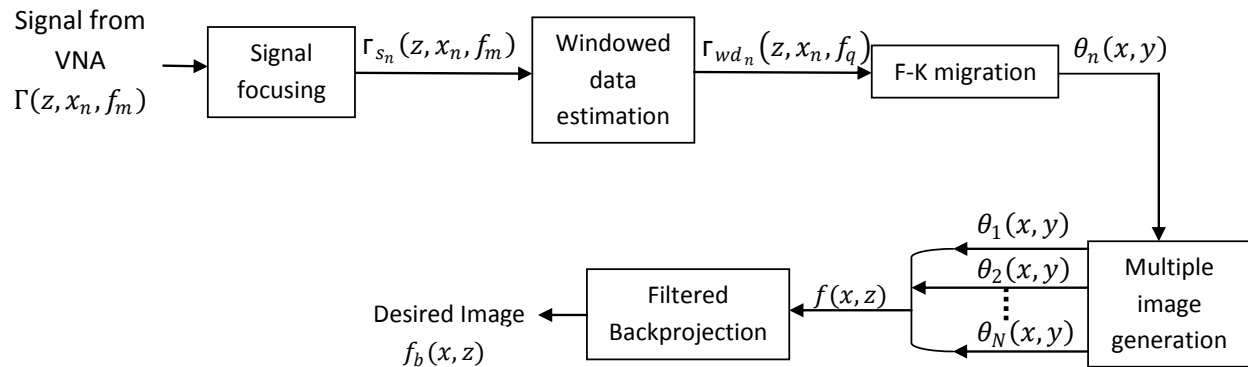


Figure 3.1: Schematic of the proposed Modified F-K (MFK) focusing technique

For the purposes of this technique, the benefits of using the frequency wavenumber for target positioning and the deblurring process of filtering after backprojection are combined when seeking to improve the target image acquisition and target edge.

Data are acquired after implementing multiple B-Scans over the area of interest by using a monostatic antenna. Consider a VNA which works as a radar system, acquiring a reflected signal

at each TX/RX position shown in Fig. 2.14. The acquired signal corresponding to each point along the x-axis, with constant z, will form the signal (z, x_n, f_m) , $1 \leq n \leq N$; $1 \leq m \leq M$. Each *n*-th row of the $N \times M$ B-scan matrix will be the acquired VNA data at the *n*-th antenna location in the x-direction.

3.2 Signal Focusing

The signal focusing module takes the VNA output as its input and focuses the signal on the target. It is assumed that the target position is known, or a possible location is established from the existing scenario. For a single antenna location (x_n, z_n) , it focuses the M complex scattering coefficients on an assumed target position (x_p, z_p) , where $p=1,2,\dots,P$ refers to the *p*-th target.

Fig. 3.2 shows a two-media signal refraction geometry. In order to calculate the correct signal path between the antenna and the target *p*, the correct refraction point between the two layers must be found. Johansson et al.[38] proposed a technique to calculate the approximate wave path of the traveling waves by finding the approximate location of the refraction point. In order to find this point, the possible wave paths are analyzed by using Snell's law. By using this law, it can be shown that if $\epsilon_1 = \epsilon_2$, the wave passes through the refraction point X_a . However, if $\epsilon_2 \gg \epsilon_1$, the refraction point is X_c as shown in Fig. 3.2. For other values of ϵ_1 and ϵ_2 , the approximate refraction point (X_b) is between X_a and X_c . Once X_b is found, the respective propagation delay for the transmitted and reflected signal for each antenna position can be calculated. This process is done in two steps.

Step 1: Refraction Point calculation

The first step is to calculate the approximate refraction point X_b shown in Fig. 3.2. Assuming the antenna location (x_n, y_j, z) and the target position (x_p, y_p, z) are known, the distance b_2 shown in Fig. 3.2.

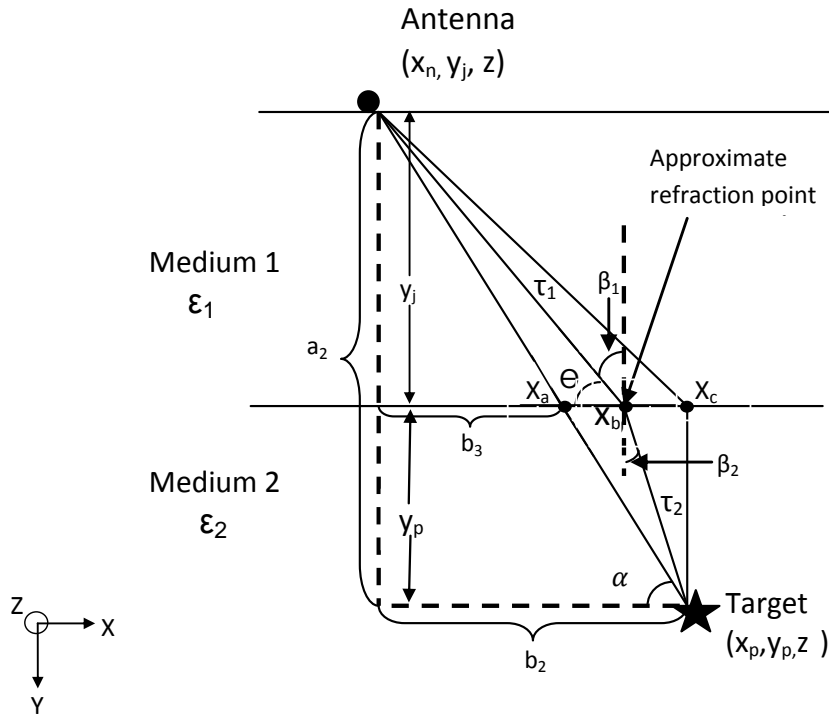


Figure 3.2: Two-media signal refraction point geometry. ϵ_1, ϵ_2 are the dielectric constants of two media (e.g., air and sand). τ_1 and τ_2 are the signal propagation delays in media 1 and 2, respectively.

The angle α in Fig. 3.2 is used to calculate b_3 and determine the exact location of X_a . These values are calculated as follows:

$$\alpha = \tan^{-1} \frac{a_2}{b_2}, \quad (3.1)$$

$$b_3 = \frac{y_j}{\tan \alpha}$$

where the distance from the antenna location to the assumed target position along the y axis can be expressed as $a_2 = y_j + y_p$. The separation between the target and the antenna location can be expressed as $b_2 = |x_p - x_n|$.

By using the approximation formula given by Johansson et al.[38], the refraction point x_b can be calculated by using the following equation:

$$x_b = x_c + \sqrt{\frac{\epsilon_1}{\epsilon_2}} (x_a - x_c), \quad (3.2)$$

where the point x_c is the same target position along the x axis. x_b , x_c and x_a point values are taken only with respect the x axis.

Step 2: Focused scattering coefficients calculation

Now that x_b is calculated, Snell's law can be used to calculate the angle β_2 by using β_1 . Note that $\beta_1 = 90 - \theta$ where θ is expressed as :

$$\theta = \tan^{-1} \left(\frac{y_j}{|x_b - x_n|} \right). \quad (3.3)$$

By using Snell's law, β_2 can be found as follows:

$$\beta_2 = \sin^{-1} \left(\frac{\epsilon_1 * \sin(\beta_1)}{\epsilon_2} \right). \quad (3.4)$$

By using θ and β_2 , path lengths τ_1 and τ_2 can be calculated as follows:

$$\tau_1 = \frac{y_j}{\sin\theta}; \quad \tau_2 = \frac{y_p}{\cos(\beta_2)}. \quad (3.5)$$

By using the τ_1 and τ_2 , the round trip propagation time can be calculated as follows:

$$\tau_{n,p} = \frac{2\tau_1}{v_1} + \frac{2\tau_2}{v_2}, \quad (3.6)$$

where v_1 and v_2 are the wave velocity in two different media and can be expressed as

$$v_k = \frac{c}{\sqrt{\epsilon_k}} \quad k = 1,2, \text{ where } k \text{ represents the media.}$$

One of the assumptions at this point is the exploding reflector model. We use only one-way trip propagation delay because we assume the signal travels only from the target to the RX. Each set of collected data is focused as follows:

$$s_n(z, x_n, f_m) = (z, x_n, f_m) \sum_{p=0}^{P-1} \exp \left\{ -j(2\pi f_m (\tau_{n,p}/2)) \right\}, \quad (3.7)$$

where P is the number of targets.

3.3 Windowed Data Estimation

After the energy is focused, the windowed data estimation module restricts the data corresponding to a set target area within the complete scenario. This module takes the focused scattering coefficients s_n as follows:

- (i) The focused data are stored in a matrix $s_n(z, x_n, f_m)$. The matrix s_n is then pre-processed by applying Hermitian signal processing, as was explained in section 2.4.3. This processing generates a matrix $H(z, x_n, t_q)$ of size $N \times Q$.
- (ii) The data of matrix H are windowed by choosing a minimum and maximum depth as shown in Fig. 2.33, to obtain the matrix $w_{d_n}(z, x_n, f_q)$. The windowing procedure is

implemented by using the same process used for GPR depth estimation explained in section 2.4.5. The value of Q depends on the f_{stop} . For example, if $f_{start} = 1 \text{ GHz}$, $f_{stop} = 10 \text{ GHz}$, $\Delta f = 10 \text{ MHz}$, $M = 901$, it can be shown that $Q = 2001$.

3.4 F-K migration

The F-K migration is a frequency domain migration technique used in seismology in order to determine the earth formation from seismic data collected at the surface. One of the assumptions in this technique is the exploding reflector model, which assumes that the energy sources are not placed at the surface, but are located along the reflecting subsurface. This assumption reduces the problem to only the upcoming waves returning back to the receiver, and for this reason, the two-way travel time of the VNA recorded data has to be converted to one-way travel time. This conversion scales down by two the wave propagation velocity.

Fig. 3.3 shows the block schematic of the F-K migration technique. The four steps in the technique are explained below:

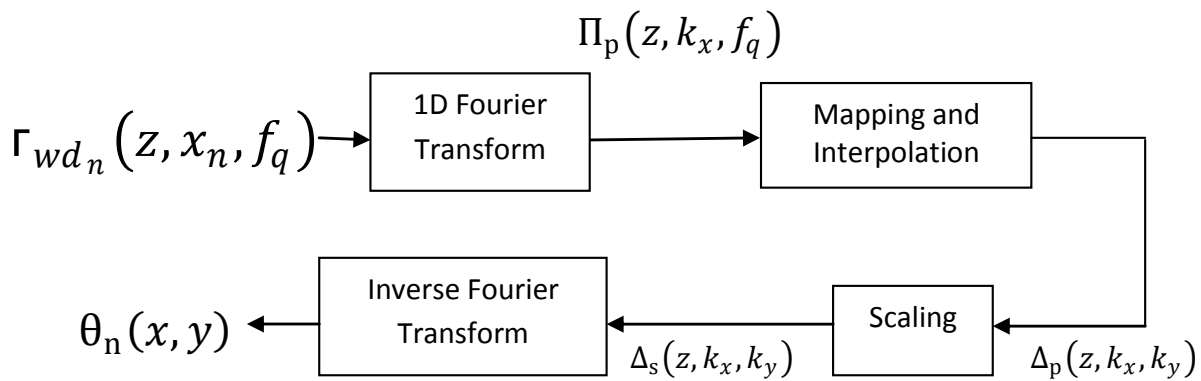


Figure 3.3: Block schematic for F-K migration technique

Step 1: 1D Fourier Transform

The objective of this module is to transform the x -coordinate to wavenumber k_x , which is similar to the spatial frequency in the x direction. This transformation is done by calculating an N -point 1-D Fourier transform of the matrix $r_{wd_n}(z, x_n, f_q)$ with respect to the x -axis. This process of calculating the 1-D Fourier transform is repeated for all f_q values, $1 \leq q \leq Q$. All results are stored in the output matrix $\Pi_p(z, k_x, f_q)$. Note that the k_x dynamic range values are satisfied by the Nyquist theorem as shown as follows.

The sampling frequency is defined as:

$$f_{sampling} = \frac{1}{\Delta x}. \quad (3.8)$$

Using the Nyquist theorem and the sampling frequency definition, it is possible to find k_{xmax} value as follows:

$$2k_{xmax} = 2\pi f_{sampling} \implies k_{xmax} = \frac{\pi}{\Delta x}. \quad (3.9)$$

Using the discrete Fourier transform theory, which states that the use of N points in the x domain implies the use of N points in the k_x domain, the following expression can be defined:

$$x_{max} = (N - 1)\Delta x \xrightarrow{DFT} 2k_{xmax} = (N - 1)\Delta k_x. \quad (3.10)$$

Solving Δk_x from Eq. 3.10, the separation between samples in the k_x domain can be determined as follows:

$$\Delta k_x = \frac{2k_{xmax}}{(N - 1)} = \frac{2\pi}{(N - 1)\Delta x} = \frac{2\pi}{x_{max}}. \quad (3.11)$$

Using Eq. 3.10 and Eq. 3.11 the dynamic range of k_x is obtained as $-k_{xmax}:\Delta k_x:k_{xmax}$ with $\Delta k_x = \frac{2\pi}{x_{max}}$ [28]. After all the 1-D Fourier transforms are calculated, the matrix size remains the same i.e., $N \times Q$. The wavenumber processing allows the extraction of spatial and directional information from waves sampled with an array of sensors in a specific spatial position [39]. Fig. 3.4 shows the frequencies corresponding to the elements of matrix $\Pi_p(z, k_x, f_q)$ for a given z value where the coefficients in a row correspond to different wavenumbers in the x direction for a given frequency f_q .

	k_x						
	$-k_{xmax}$	Δk_x	0	k_{xmax}			
$\omega_1 = 2\pi f_1$							
$\omega_2 = 2\pi f_2$							
$\omega_3 = 2\pi f_3$							
⋮							
$\omega_Q = 2\pi f_q$							

Figure 3.4: Matrix illustration of $\Pi_p(z, k_x, f_q)$ with respect (ω, k_x) , where $\omega_q = 2\pi f_q$.

Step 2: Mapping and Interpolation

In step 1, we introduced the concept of wavenumber k_x in x direction. There is an equivalent wavenumber k_y in the y direction. In this step, we derive a relationship between the frequency f_q , the wavenumber k_x in the x direction, and the wavenumber k_y in the y direction. This process will allow us to represent the matrix Π_p by using only wavenumbers (for a fixed z).

Mapping: It can be shown that k_x, k_y and ω_q are related by the following equation [41]:

$$k_x^2 + k_y^2 = \frac{\omega_q^2}{v_m^2}, \quad (3.12)$$

where the velocity through the media $v_m = v/2$, where v the propagation velocity following the exploding reflector model mentioned at the beginning of this section.

Eq. 3.12 has the form of a circle. This form shows that the (k_x, k_y) space for constant frequencies is represented as semi-circles with radius (ω_q/v_m) as shown in Fig. 3.5 (a). Note that unlike k_x , $k_y \geq 0$. In Fig. 3.5 (b), the $(k_x, \omega_q/v_m)$ space is superimposed over the (k_x, k_y) space represented in Fig. 3.5 (a). Fig. 3.5 (b) shows an example of how the ω_q/v_m data is mapped to the respective semi-circle with radius ω_q/v_m in the k_y domain for a fixed $k_x = -k_{xmax} + \Delta k_x$ value. The mapping process is done by solving Eq. 3.12 for k_y as is shown in the following equation:

$$k_y = \sqrt{\left(\frac{\omega_q}{v_m}\right)^2 - (k_x)^2}. \quad (3.13)$$

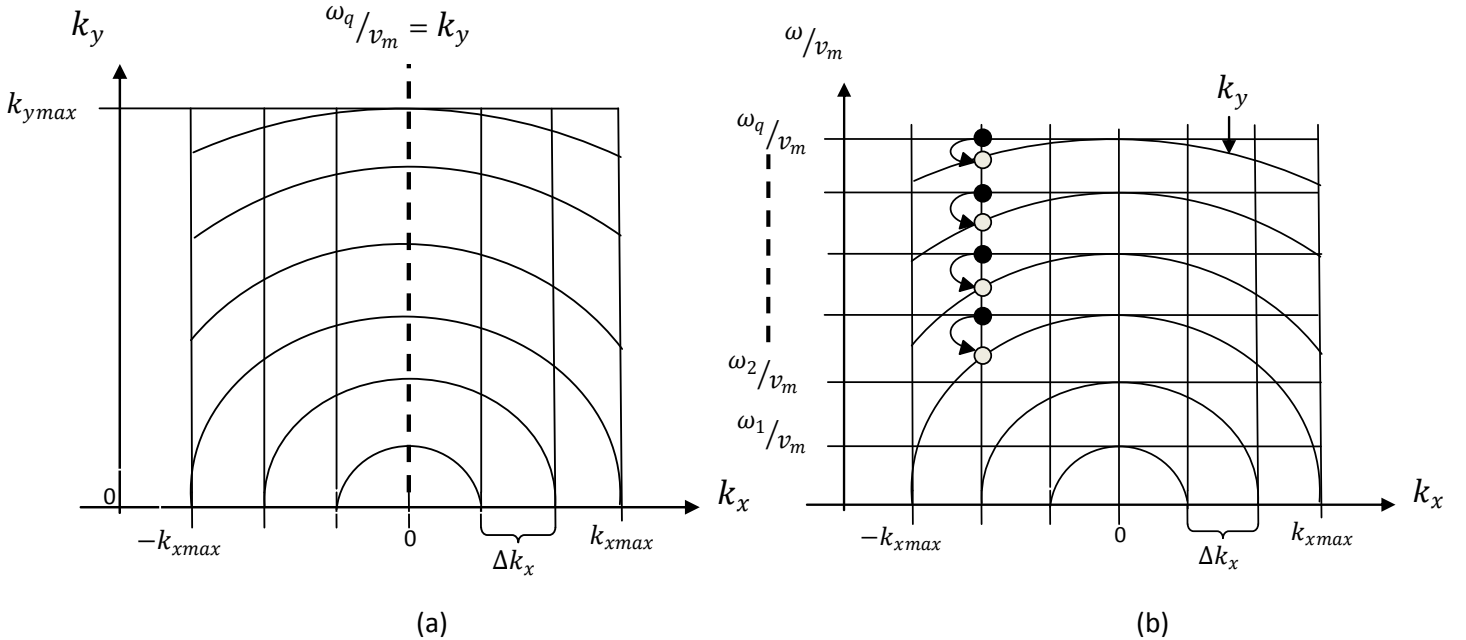


Figure 3.5: (a) The space (k_x, k_y) with contours of ω_q/v_m as given in Eq.3.7. (b) Mapping process from $(-k_{xmax} + \Delta k_x, \omega_q/v_m)$ to $(-k_{xmax} + \Delta k_x, k_y)$ [40].

Interpolation: After the mapping, let the minimum and maximum value of k_y be denoted as k_{ymin} and k_{ymax} , respectively. The values of k_{ymin} and k_{ymax} can be calculated as follows:

$$k_{ymin} = 0,$$

$$k_{ymax} = \sqrt{\left(\frac{\omega_q}{v_m}\right)^2 - \max(\text{abs}(k_x))^2}, \quad (3.14)$$

where $\left(\frac{\omega_q}{v_m}\right)$ is calculated using the last q frequency value, and $\max(\text{abs}(k_x))$ is the maximum value in the k_x range. After the new k_y range is defined, a linearly spaced vector with size $1 \times Q$ is generated between the minimum and maximum value [28,40]. This vector is repeated in order to generate an $N \times Q$ matrix. Note that k_x is an $N \times 1$ vector, defined in step 1, and is repeated for each f_q , generating an $N \times Q$ matrix.

In Fig. 3.6 (a), the mapped values for k_{ymax} and k_{ymax-1} are taken as an example to show that the mapped data is not evenly spaced. An evenly spaced data matrix, in the $k_x - k_y$ domain, is now generated by interpolating the mapped data as shown in Fig. 3.6 (b). The interpolated matrix is denoted as $\Delta_p(z, k_x, k_y)$. In this thesis, we have used bilinear interpolation

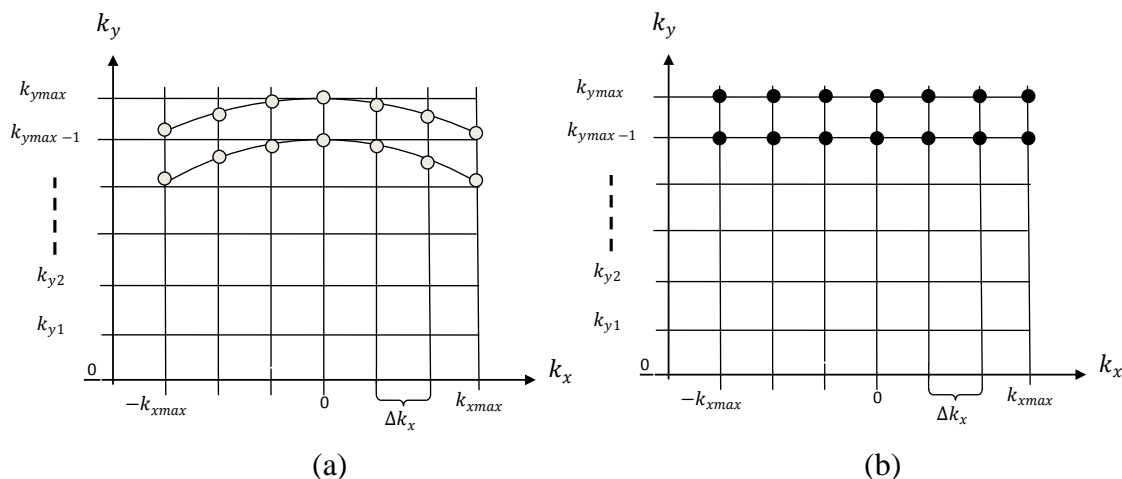


Figure 3.6: (a) Mapped data for k_{ymax} and k_{ymax-1} in the (k_x, k_y) domain (b) Interpolated data for k_{ymax} and k_{ymax-1} in the (k_x, k_y) domain.

Step 3: Scaling

The scaling factor is used to appropriately scale the change from ω to k_y and $d\omega$ to dk_y domain in the interpolated matrix as follows:

$$\Delta_s(z, k_x, k_y) = \Delta_p(z, k_x, k_y) * \frac{d\omega}{dk_y} \quad (3.15)$$

Note that Eq. 3.12 can be rewritten as:

$$\omega(n, q) = v_m \sqrt{k_x(n, q)^2 + k_y(n, q)^2} \quad (3.16)$$

Differentiating Eq. 3.16 with respect k_y , we obtain:

$$\frac{d\omega}{dk_y} = \frac{v_m(2k_y)}{2\sqrt{k_x^2 + k_y^2}} = \frac{k_y(n, q)v_m}{\sqrt{k_x(n, q)^2 + k_y(n, q)^2}} \quad (3.17)$$

In other words, Eq. 3.15 can be expressed as:

$$\Delta_s(z, k_x, k_y) = \Delta_p(z, k_x, k_y) * \frac{k_y(n, q)v_m}{\sqrt{k_x(n, q)^2 + k_y(n, q)^2}} \quad (3.18)$$

The mapped and interpolated matrix $\Delta_p(z, k_x, k_y)$ with size $N \times Q$ will be scaled by the result of Eq. 3.17, giving as a result an scaled matrix $\Delta_s(z, k_x, k_y)$ with size $N \times Q$.

Step 4: Inverse Fourier Transform

After the 2-D matrix $\Delta_s(z, k_x, k_y)$ is obtained, the inverse Fourier transform (IFT) of the 2-D matrix $\Delta_s(z, k_x, k_y)$ is calculated to move from the $k_x - k_y$ plane to the Cartesian

coordinates (x, y) . The IFT is calculated separably using 1-D IFT's, first along the k_x axis and then along the k_y axis. The steps are as follows:

- (i) Calculate the 1-D IFTs over the k_x axis for each value of k_y .
- (ii) The Hermitian signal processing mentioned in section 2.4.3 is performed along the k_y axis. The data along k_y axis for each k_x value has $2Q$ samples.
- (iii) Calculate the 1-D IFT over the k_y axis for each value of k_x .

When steps (i)-(iii) are completed, the obtained matrix (after IFT) is expressed as follows:

$$\theta_{fk}(x, y) = \sum_{q=0}^{2Q-1} \sum_{n=0}^{N-1} \Delta_s(z, k_x(n, q), k_y(n, q)) e^{-j\left(\frac{k_x(n, q)x}{N} + \frac{k_y(n, q)y}{Q}\right)}. \quad (3.19)$$

- (iv) As the number of antenna locations (in our experiment, $N=10$) per B-scan is very small, the $N \times 2Q$ matrix must be resampled row-wise. After resampling the data, the matrix size will be $R \times 2Q$. In order to find the relationship between k_y and y , it is necessary to follow the discrete Fourier transform (DFT) theory and the sampling theorem. It can be shown that the relationship between k_y and y is as follows:

$$2k_{y \max} = (2Q - 1)\Delta k_y \xrightarrow{IDFT} y_{\max} = (2Q - 1)\Delta y. \quad (3.20)$$

Using the sampling theorem, and assuming the sampling frequency, f_s , in the y direction, we obtain the following:

$$2\pi f_s = 2k_{y \max}, \quad (3.21)$$

where f_s along the y axis is defined as:

$$f_s = \frac{1}{\Delta y}. \quad (3.22)$$

Replacing Eq. 3.22 in Eq. 3.21, it is possible to find a relation between $k_{y_{max}}$ and y_{max} through Δy as shown below:

$$\frac{2\pi}{\Delta y} = 2k_{y_{max}} \implies \frac{\pi}{\Delta y} = k_{y_{max}} \implies \Delta y = \frac{\pi}{k_{y_{max}}}, \quad (3.23)$$

The $k_{y_{max}}$ value can be obtained using Eq. 3.14. Replacing the obtained Δy depth resolution from Eq. 3.23 into Eq. 3.20, it is possible to obtain the depth location of our data for different q ($q = 1, 2, \dots, Q$) value .

- (v) Since y_{max} is going to be out of our range of interest, the $R \times 2Q$ values are focused in the range between y_{min} and y_{max} . In our experimental set-up, $y_{min}=0.1\text{m}$ and $y_{max}=0.5\text{m}$. A final image $\theta_n(x, y)$ of size $R \times J$, where J is the data between $[y_{min}, y_{max}]$, and R is the resampled data row-wise.

3.5 2-D Image Generation

The schematic of the proposed technique was shown in Fig. 3.1. After the first three modules, i.e., after F-K migration, the output $\theta_n(x, y)$ with size $R \times J$ is obtained. These three modules are repeated N times for all the different (z, x_n, f_m) collected along the grid for N different z values, A final output of $\theta_N(x, y)$ B-scan images are obtained as shown in Fig. 3.7. From these images, a horizontal image $f(x, z)$ with size $N \times R$ corresponds to the object plane at depth y (with respect to the antenna plane) will correspond to the row y of the different 2-D matrices $\theta_n(x, y)$, as shown in Fig. 3.7. The image at the depth y can be expressed as follows:

$$f_y(x, z) = \begin{bmatrix} \theta_1(0, y) & \theta_1(1, y) & \cdots & \theta_1(N-1, y) \\ \theta_2(0, y) & \cdots & \cdots & \theta_2(N-1, y) \\ \vdots & \cdots & \cdots & \vdots \\ \theta_N(0, y) & \theta_N(1, y) & \cdots & \theta_N(N-1, y) \end{bmatrix} \quad (3.24)$$

The sampling interval Δz in the z direction is much higher with respect the sampling interval Δx in the x direction. In order to obtain uniform sampling interval in both x and z , the matrix $f_y(x, z)$ is upsampled by an appropriate factor U_x and U_z along the x and z axis, respectively.

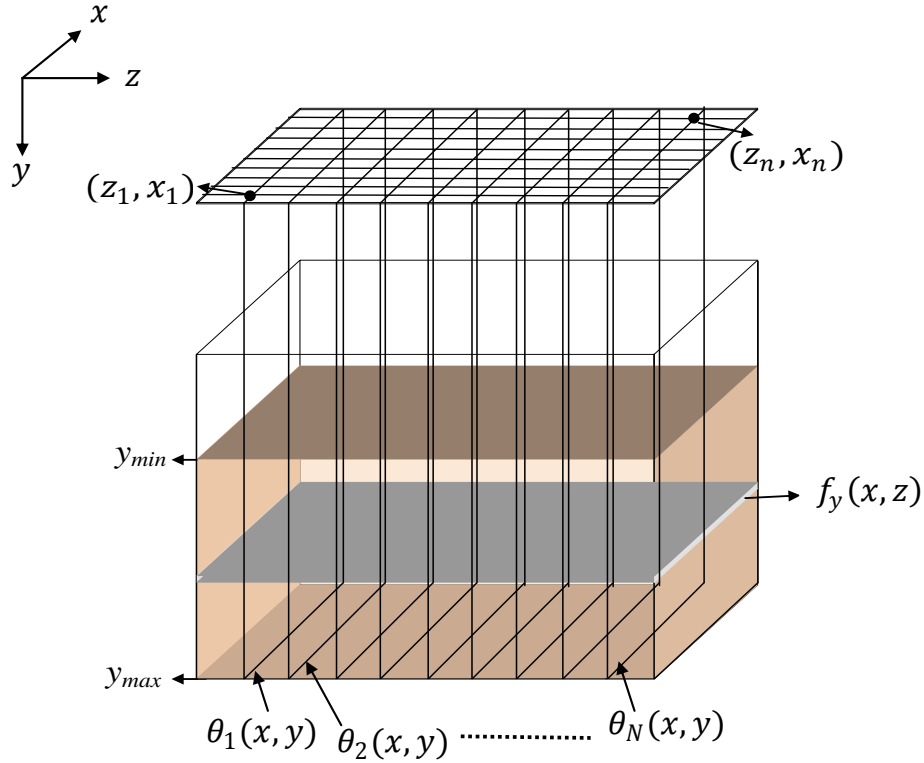


Figure 3.7: Image reconstruction before filtering

3.6 Filtered backprojection

The filtered backprojection module reduces the blurring generated in MRI and radar imaging, where reflected signals at different angles are added to reconstruct a target image. This process will not only reconstruct the target, it will also generate blurring around the detected target

caused by summation process. In our technique, the data was collected using the same process used in radar backprojection implementation. Note that in the proposed technique filtered backprojection is done in the Fourier domain to reconstruct the image.

In this module it is assumed that the resampled matrix $f(x, z)$, generated in section 3.5, is the resulting blurred image $\hat{f}(x, z)$ expressed in Eq. 2.63. By following the backprojection filtering explained in section 3.6.1, $f(x, z)$ is filtered in order to get the deblurred and final version of our image. The implemented filter is defined as follows:

$$H(u, v) = \sqrt{\left(\frac{u}{(M - \Delta M)}\right)^2 + \left(\frac{v}{(N - \Delta M)}\right)^2}, \quad (3.25)$$

where $M \times N$ is the size of $f(x, z)$, and the ΔM value is changed between 0 and approximately M , while searching for the optimum target resolution. Fig 3.8 shows an example of $H(u, v)$ for $M = 550$, $N = 600$, and $\Delta M = 450$.

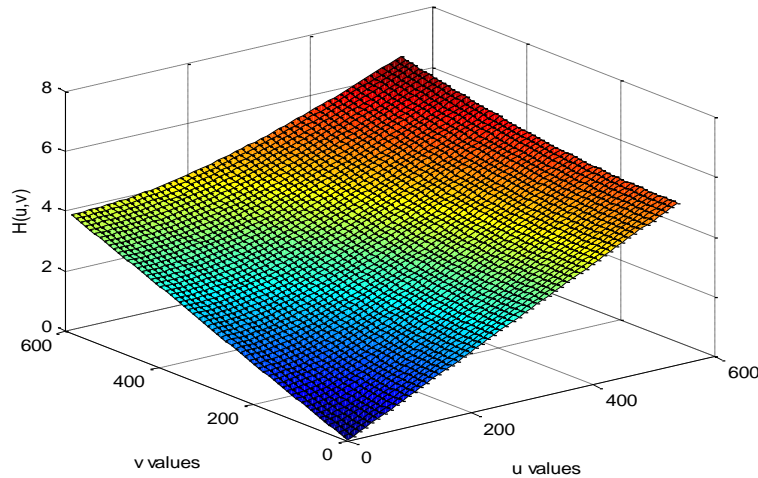


Figure 3.8: Filter frequency response

In Fig. 3.9, the frequency response is plot using different ΔM values.

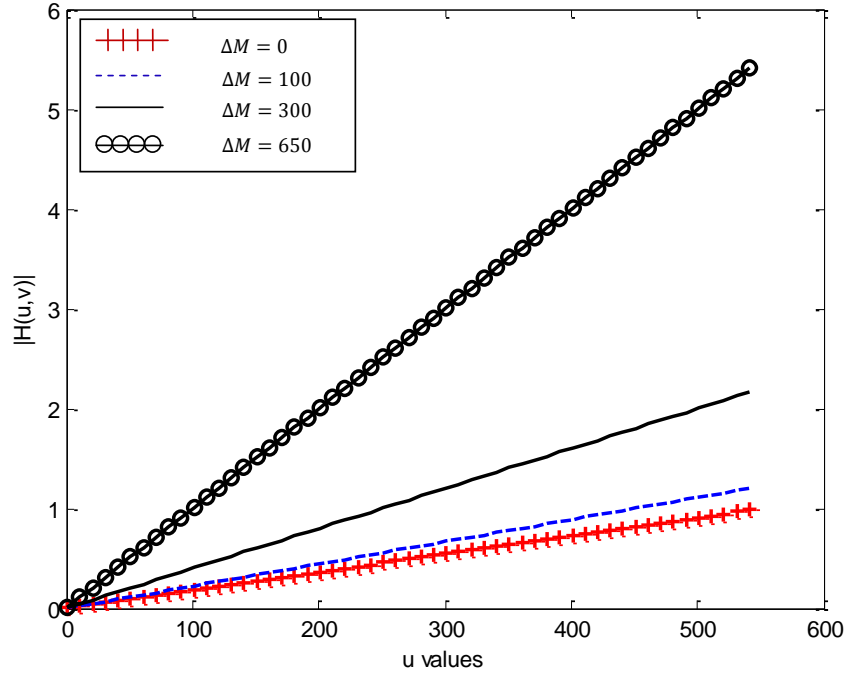


Figure 3.9: Filter frequency response for different ΔM values (with $M = 550$, $N = 600$).

The final image can be found as follows:

$$f_b(x, z) = \sum_{u=0}^{U-1} \sum_{v=0}^{V-1} H(u, v) F(u, v) e^{j2\pi\left(\frac{ux}{U} + \frac{vz}{V}\right)}. \quad (3.26)$$

where $\mathbf{F}(\mathbf{u}, \mathbf{v})$ is the 2-D Fourier transform of $\mathbf{f}(\mathbf{x}, \mathbf{z})$, and $\mathbf{f}_b(\mathbf{x}, \mathbf{z})$ is the 2-D IFFT after multiplying $\mathbf{H}(\mathbf{u}, \mathbf{v})$ by $\mathbf{F}(\mathbf{u}, \mathbf{v})$.

3.7 Summary

In this chapter, we presented a brief introduction to the main problems to be solved by any GPR or TWI technique. The proposed technique implemented in this thesis was presented in section 3.1. The main purpose of the proposed technique is to improve the target image and target size. The collected data was processed assuming the B-scan properties. These data was processed

through five modules. In the module described in section 3.2, the collected data was focused on a given target location. In section 3.3, the focused data was windowed, conserving the data relevant to the area of study. In section 3.4, the F-K migration theory was applied to the windowed data, which generate a B-scan matrix that contains the located scattered data. In section 3.5, all the different $\theta_n(x, y)$ B-scan matrices, generated from the grid showed in Fig. 2.14, were stored, and a sectional image $f(x, z)$ was generated. In section 3.6, it was explained how the backprojection filtering was implemented in our proposed technique and a superior image was obtained.

Chapter 4

Performance Evaluation

In chapter 3 we presented the Modified F-K (MFK) focusing technique. In this chapter we evaluate the performance of the proposed technique, and compare with other existing techniques. In section 4.1, we present the experimental set-up. In section 4.2, we present the generated images obtained by processing the collected data using the proposed MFK focusing technique. The proposed technique was implemented by both excluding and including the antenna length (8 cm). The resulting images are compared with the results obtained by implementing two common migration techniques (F-K and Kirchhoff migration). For the implemented migration techniques, it is assumed that the wave travels over a single media environment (sand) with a dielectric constant $\varepsilon = 3.5$.

4.1 Experimental Set-up

An experiment was set-up in the laboratory by using a 40 cm x 30 cm box as a sampling area. For our measurement, the design of a monostatic radar was used. Vivaldi antennas [43], which were connected to an Agilent E8362B vector network analyzer (VNA), were implemented. Fig. 4.1 shows a closer view of both sides of one of the antennas used during the experiments.

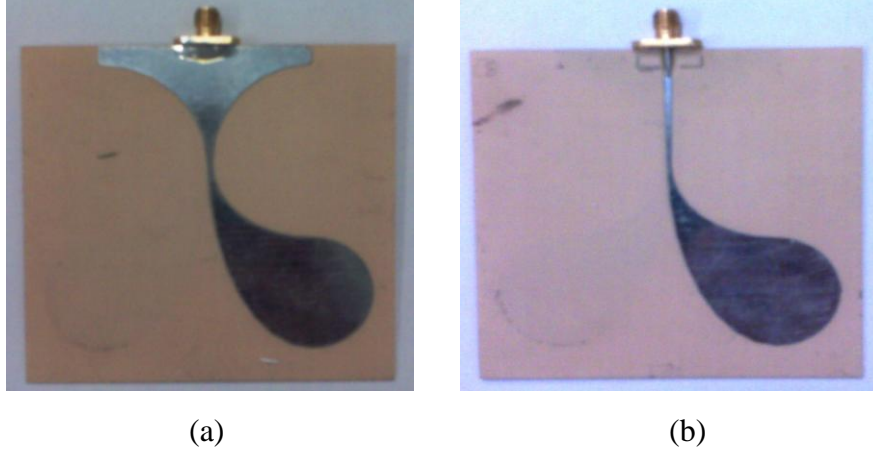


Figure 4.1: Vivaldi antenna (a) side 1 and (b) side 2.

The transmitted signal at a given position (x_i, z_j) is a stair-case frequency signal as shown in section 2.4.1, where the transmitted signal with m -th frequency can be represented as $\exp\{-j2\pi f_m t\}$, where $f_m = f_0 + m\Delta f$ and Δf is the step frequency. The measurement frequency is varied from 1GHz to 10 GHz with constant increments of 10 MHz. A total of 901 samples for the same number of frequencies are collected. Each collected data set is initially stored in the VNA hard drive and then transferred to a USB drive to be processed using the respective algorithms explained in Chapters 2 and 3. This measurement process was done using two different scenarios, which are described in section 4.1.1 and 4.1.2.

4.1.1 Scenario 1

In this scenario, the antennas were located at 28 cm from the sand and the measurements were taken with sampling intervals $\Delta x = 3.6 \text{ cm}$, $\Delta z = 2.7 \text{ cm}$ to provide a total of 100 measurement points. Three different targets were buried separately at 6 cm depth as shown in Fig. 4.2 and Fig. 4.3.

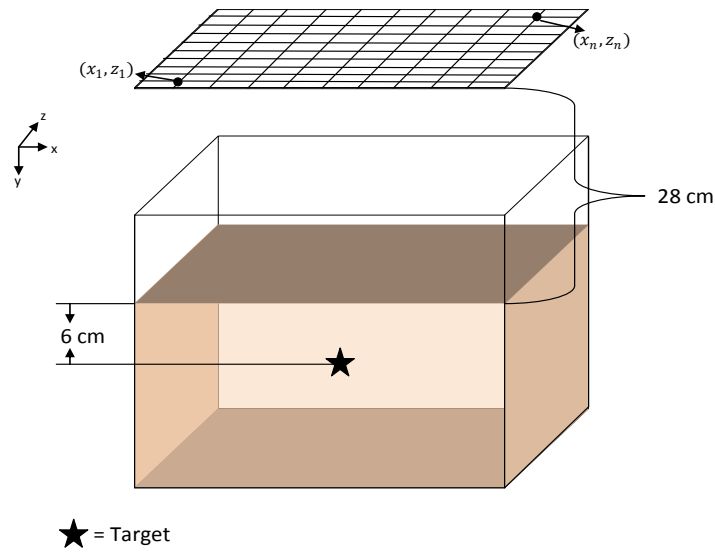
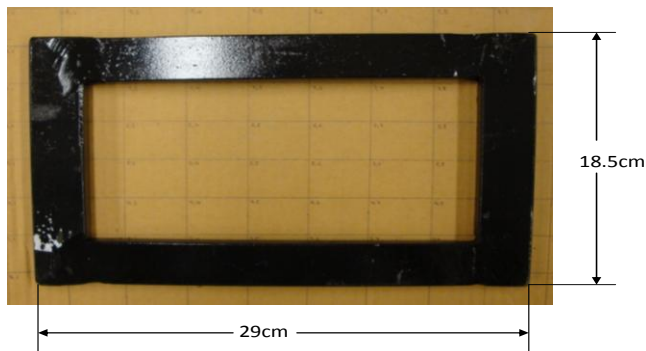
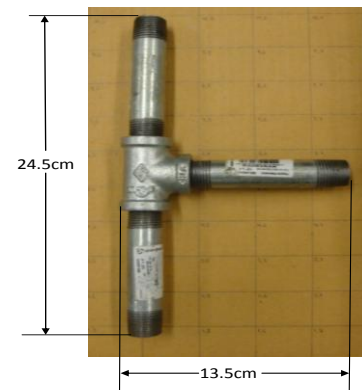


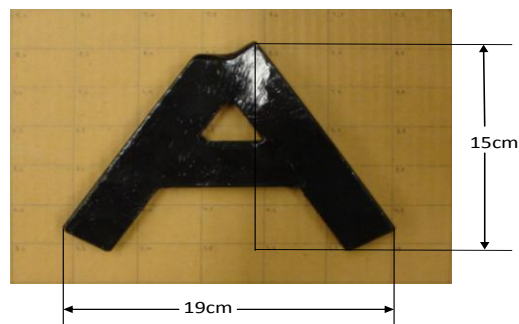
Figure 4.2: Laboratory setup scenario 1.



(a)



(b)



(c)

Figure 4.3: Target dimensions scenario 1(a) Rectangle, (b) Pipe and (c) Letter A.

The targets shown in Fig. 4.3 have different shapes, in order to evaluate the image reconstruction efficiency for different techniques. For the antenna distance from the sand to the lower dimension of the antenna is 28 cm and to the upper dimension of the antenna is 36 cm.

4.1.2 Scenario 2

In scenario two, the antennas were located at 42 cm from the sand, and the measurements were taken with sampling intervals $\Delta x = 4 \text{ cm}$, $\Delta z = 3 \text{ cm}$ to provide a total of 81 measurement points. The target was buried at 6 cm depth as shown in Fig. 4.4. In Fig. 4.5, the target used in this scenario is shown with the respective physical dimensions.

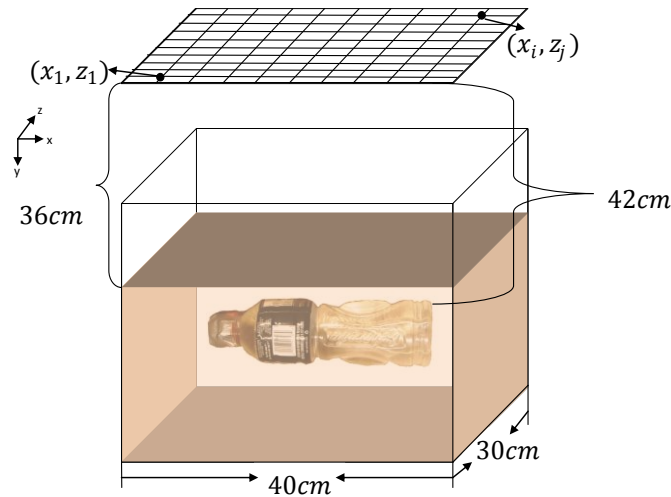


Figure 4.4: Scenario 2 dimensions and target (bottle) location.

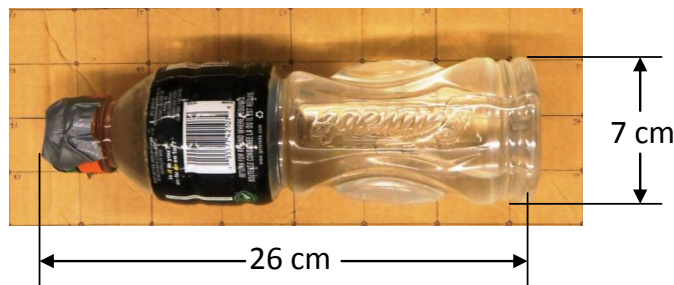


Figure 4.5: Target dimension scenario 2.

The distance from the sand to the antenna lower dimension is 36 cm as shown in Fig 4.4. If the distance is changed to the upper dimension then it changes to 44 cm.

4.2 Developed Software

The software was implemented using Matlab 7.10.0 (R2010a). The following table explains the purpose of each implemented function and the corresponding reference.

Table 4.1: List of MATLAB codes

Matlab Codes	
Function name	Objective
sec_im=fk_im_gen_and_filt()	Generates a sectional 2-D image compiling all the different B-scan's as the one explained on section 3.5 and includes the filtering module
[y]=delayandsumGPR(mag,freqvec,xapos,yapos,zapos, pha)	Focusing module explained in section 3.2. It takes as an input the magnitude from S21 parameter, the frequency vector, the antenna position along x, y and z axis, and the phase from S21 parameter. It returns the focused data to be windowed and processed inside the respective fk function.
[x]=tdelayGPR(Xr,Yr,Zr,TargX,TargZ,TargY,numtarg)	Time delay calculation for the focusing module. It takes as an input the antenna position along the x, y and z axis. A possible target (s) location is/are given along the x, z and y axis and a number of targets is defined. It gives as an output the one way time delay.
[S]=call_b_scan_data(val1)	This function calls the collected data on each B-scan (val1) and returns the collected data on a matrix S1.
[c1 datain1]=bscan_data(bscan,ant)	This function generates the complex expression of the collected B-scan data. It takes as an input the B-scan number and the measurement number. It returns c1 that contains the complex form of the measurements with target and data1 contains the complex form of the collected data without target.
see_img=kirch_im_gen()	Generates a sectional 2-D Kirchhoff image compiling all the different B-scan's as the one explained on section 3.5

Matlab codes obtained from [28]	
[d1]=fk(S)	This function calculates one B-scan F-K migration (for different z fixed values) by taking into account the focusing and windowing modules.
fk1_pipe_modified, fk2_pipe_modified, fk3_pipe_modified, fk4_pipe_modified, fk5_pipe_modified, fk6_pipe_modified, fk7_pipe_modified, fk8_pipe_modified, fk9_pipe_modified and fk10_pipe_modified	Calculates one B-scan F-K migration reducing the noise by taking into account the scenario without target and using the windowing module.
[k1]=kirchhoffmigration(S1)	Each function calculates one B-scan Kirchhoff migration image for different z fixed values. Takes as an input the data from each B-scan data from kirch_b_scan function individually.

4.3 Reconstructed Images

The subjective quality of the reconstructed images is important in radar imaging. Ideally the obtained target shape and the dimensions should be as close to the target as possible. As shown in Fig. 4.3, the targets used in scenario 1 were measured to facilitate the comparison with the reconstructed target dimensions. All reconstructed images were scaled according to the initial scenario dimensions. The targets used in scenario 1 were all metallic objects, and the target used in scenario 2 was a plastic water bottle. Since the targets in scenario 1 and scenario 2 have different dielectric constants, we can compare the efficiency of each technique in detecting different targets composed of different materials and different shapes. In section 4.3.1, we will show in three steps the process followed in the proposed technique to obtain one B-scan image. For this purpose, the measurements taken along the x axis with $z = 15$ cm for the pipe set-up, were taken as an example. In section 4.3.1.1, we show the efficiency of the backprojection filter module comparing the generated images before and after the module. In section 4, we show the

images reconstructed for the scenario 1 and scenario 2 measurements by using the two migration techniques (F-K, Kirchhoff) and the proposed modified F-K focusing technique.

4.3.1 Image reconstruction process

The reconstruction process for the proposed technique was explained in section 3.1. In this section we will show in three steps, as an example, the pipe scenario results for and specific B-scan for the three first proposed modules.

- (i) Input signal: The magnitude and phase for the collected data at the antenna location $x = 3.6$ cm with $z = 13.5$ cm are shown in Fig. 4.6.

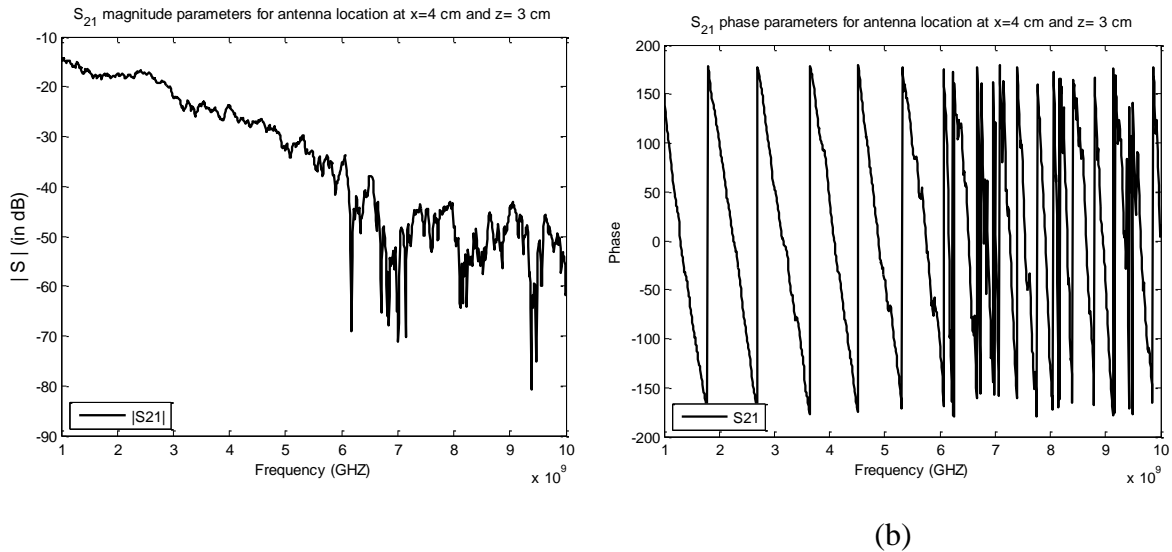
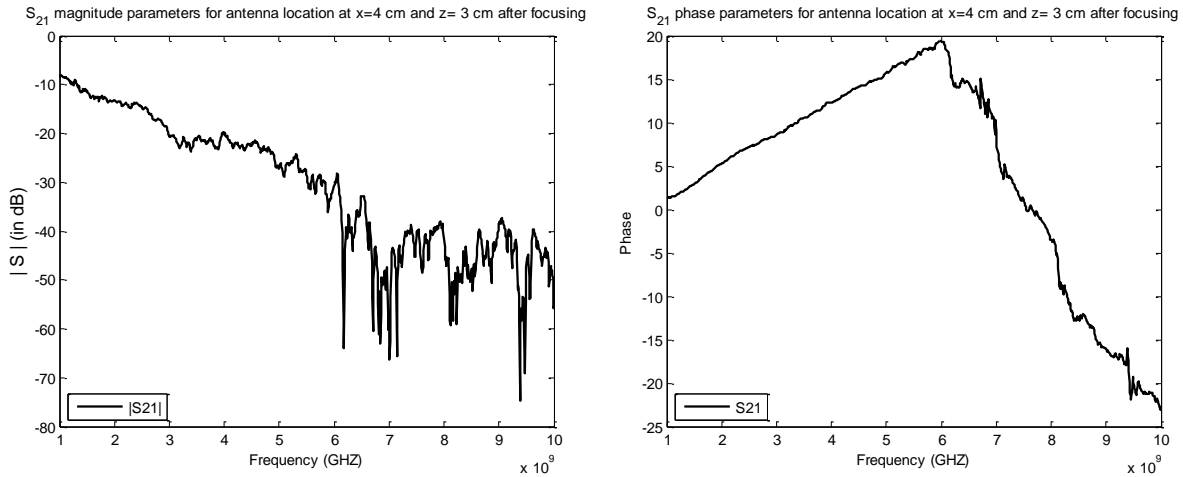


Figure 4.6: Collected data at $x = 3.6$ cm with $z = 13.5$ cm antenna location (a) Magnitude and (b) Phase.

- (ii) Focused signal: The collected phase changes due to the signal focusing process from a particular antenna location to a specific target location, as expressed in Eq. 3.7. This equation shows that the calculated focused phase is added to the original phase modifying the resulting signal phase. The magnitude has a small change due to the

assumption of multiple target locations in our scenario and the contribution of each of them during the focusing process. The focused signal magnitude and phase are shown in Fig. 4.7.



(b)

Figure 4.7: Focused data at $x = 3.6$ cm with $z = 13.5$ cm antenna location (a) Magnitude and (b) Phase.

Step (i) and (ii) are repeated for each antenna location along $z = 13.5$ cm and then we proceed to apply the module 3 to our processing.

- (iii) After the data in all the different antenna locations is collected and focused, it is possible to apply the F-K migration module to obtain one B-scan image that shows the location of the reflected signal. In Fig. 4.8, it is possible to see a strong reflection between 0.3 and 0.35 meters. As we know the pipe location from our set-up, this reflection coincides with the pipe position with respect the x-range.

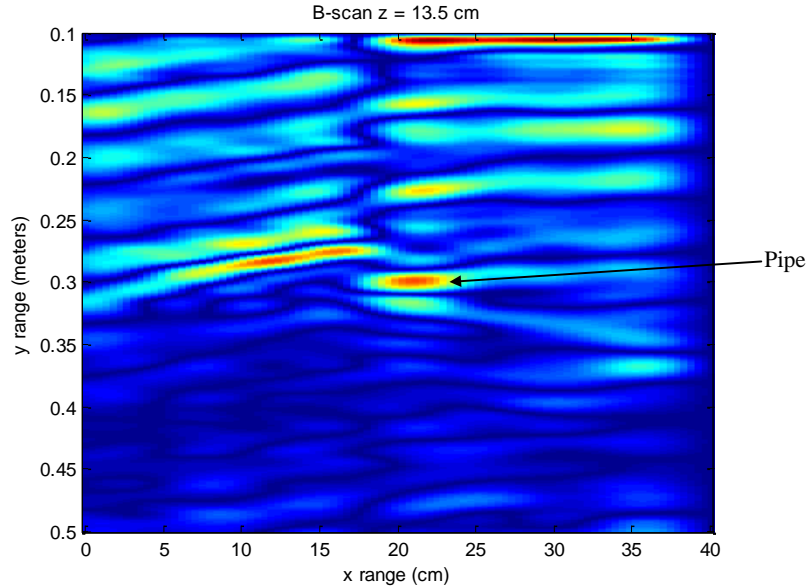


Figure 4.8: B-scan image for pipe scenario at $z = 13.5$ cm.

4.3.1.1 Effect of Backprojection Filtering

Basics of backprojection filtering explained in section 2.6.1 were used in our proposed image reconstruction. In the following images we are showing the effects that the filtering module, shown in chapter 3, is having over our reconstructed images. The images generated before filtering were upsampled by a factor of 68 and 9 along the x and z axis, respectively, as explained in section 3.5. For purposes of our comparison, we only show, as an example, the effects over the Modified F-K focusing technique including the antenna length. The results are compared based in the original targets, shown in Fig. 4.9.

The detected object can be determined from the image before filtering, but it is possible to see that the reflection is not even or strong as it could be expected. However, after the filter was implemented, the displayed target in Fig. 4.10 (b) to Fig. 4.13 (b) is improved with respect Fig. 4.10 (a) to Fig. 4.13 (a), allowing us to determine the target shape in all the different set-ups.

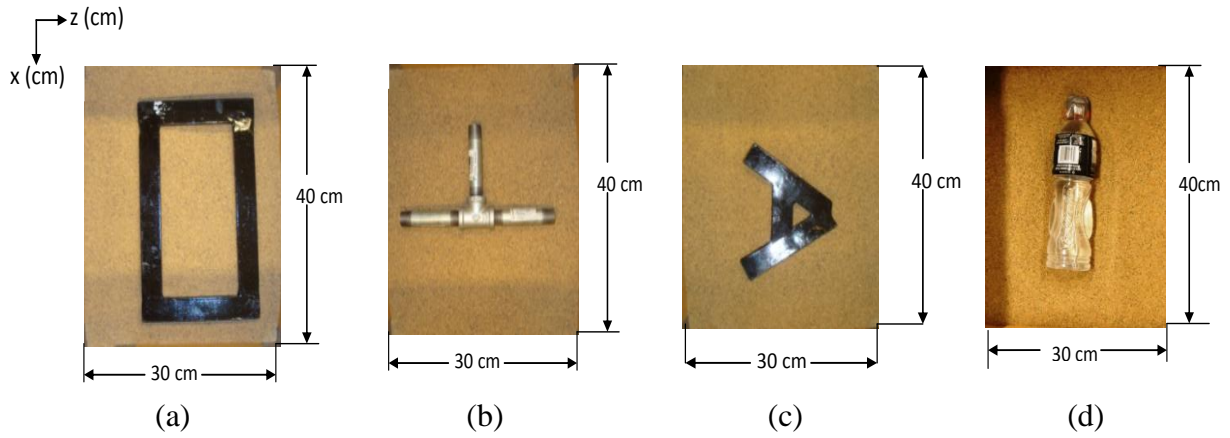


Figure 4.9: (a) “Rectangular” object (b) “Pipe” object (c) “A” object and (d) “bottle” object

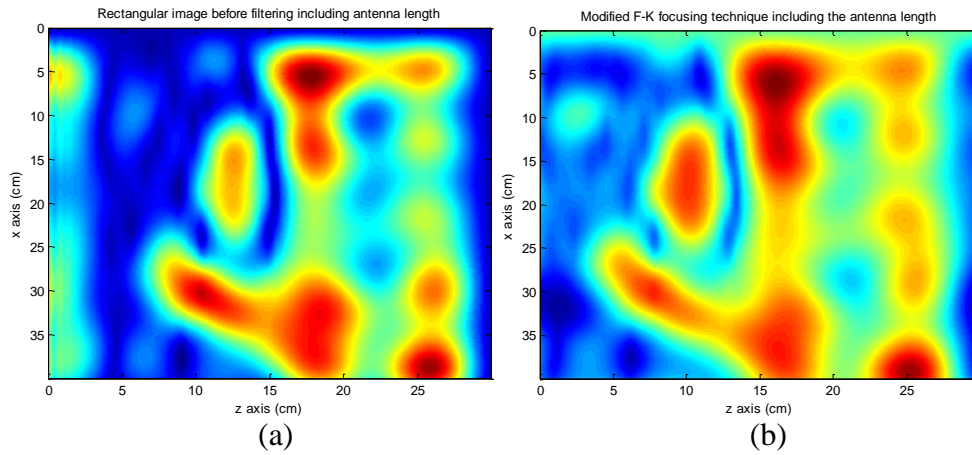


Figure 4.10: Rectangular object (a) before filtering, (b) after filtering. Filter value was set with $\Delta M=837$, $M=673$ and $N=837$.

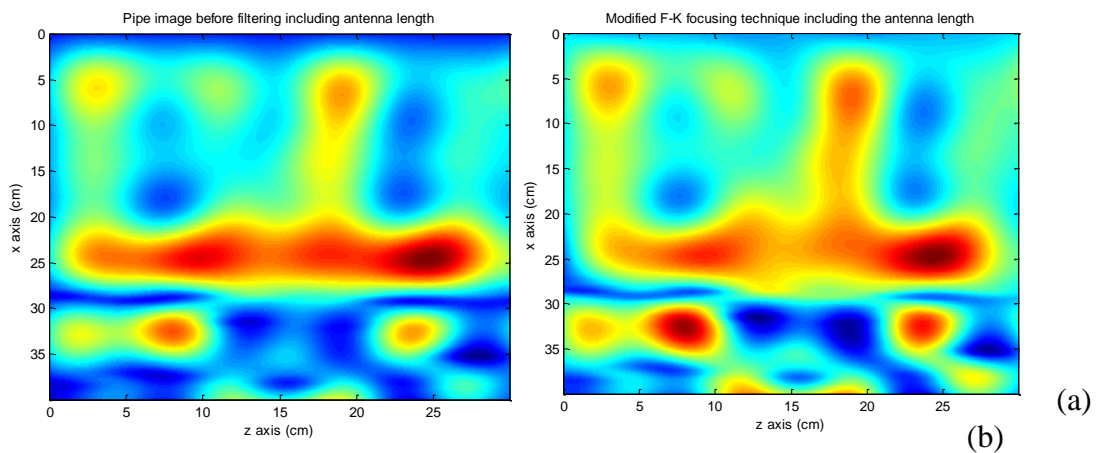


Figure 4.11: Pipe object (a) before filtering, (b) after filtering. Filter value was set with $\Delta M=450$, $M=673$ and $N=837$.

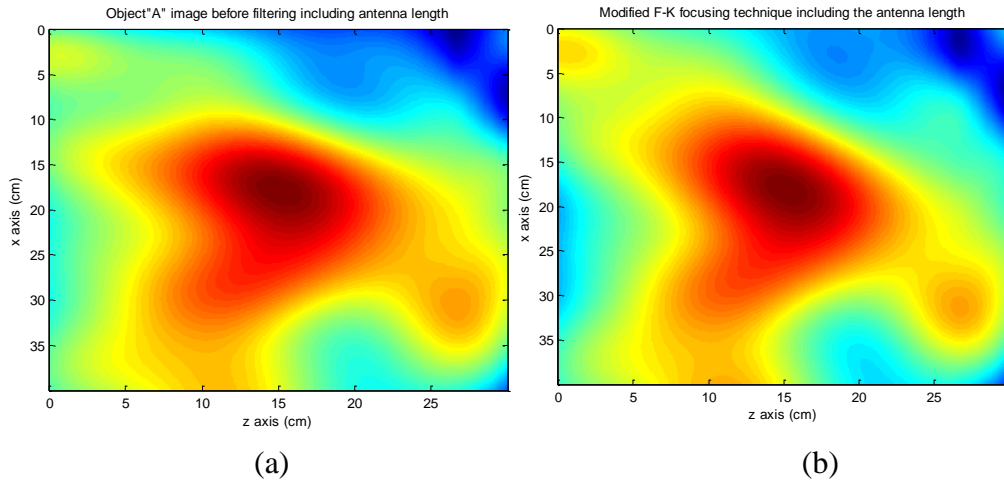


Figure 4.12: Object “A” (a) before filtering, (b) after filtering. Filter value was set with $\Delta M=850$, $M=673$ and $N=837$.

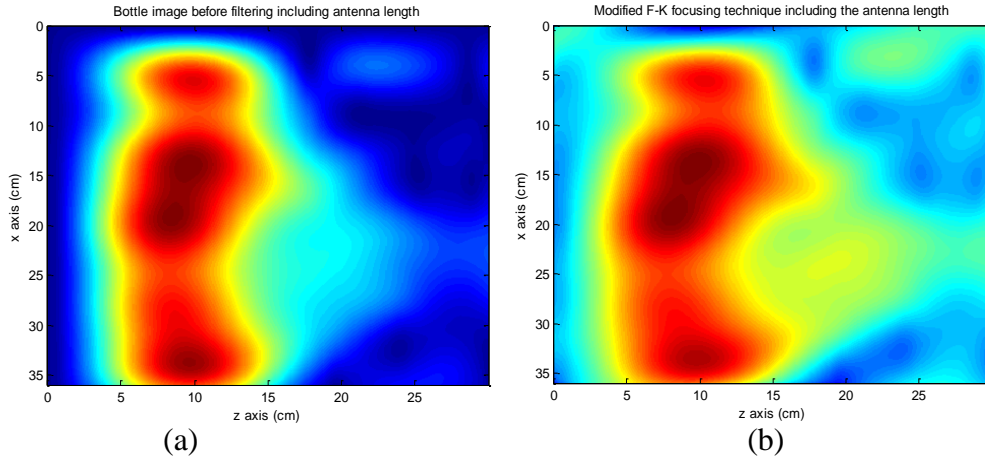


Figure 4.13: Object “bottle” (a) before filtering, (b) after filtering. Filter value was set with $\Delta M=107$, $M=406$ and $N=837$.

The value of ΔM becomes important in the image reconstruction, because this value has an effect over the target resolution in the reconstructed image. The effect that ΔM has over the image reconstruction is shown in Fig. 4.14, where it is possible to see how the target resolution improves with the change of ΔM . The “pipe” reconstructed image was taken as an example using three different ΔM values.

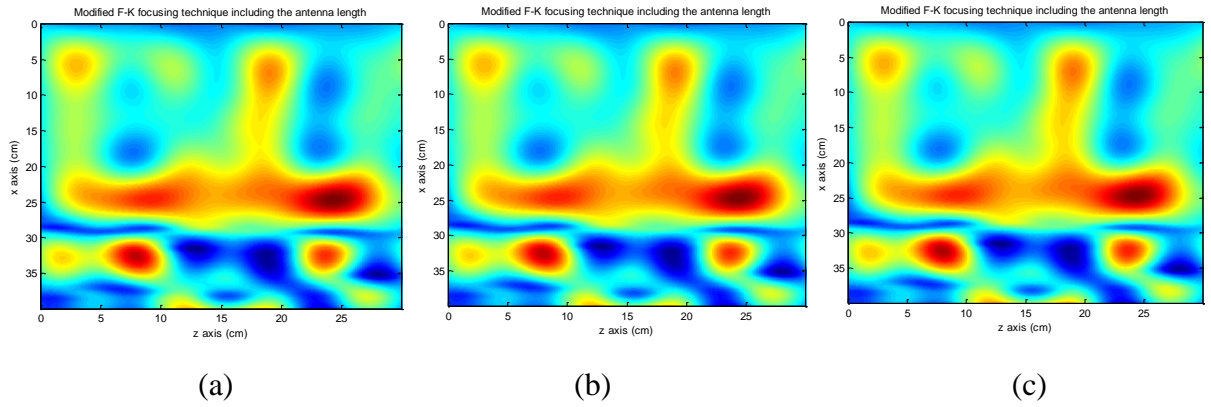


Figure 4.14: Object “pipe” reconstructed image (a) with $\Delta M=0$, (b) with $\Delta M=100$ and (c) with $\Delta M=300$. $M=406$ and $N=837$ for all the examples.

4.4 Comparison of the MFK technique with other techniques

Different studies have focused on Kirchhoff migration and F-K migration [44], and the comparison of their resulting images has demonstrated that Kirchhoff migration is an efficient ground-penetrating imaging technique. In this section we present the resulting images of these two migration techniques and the proposed modified F-K focusing technique excluding and including the antenna length for all the different scenarios.

Object “rectangle”: Fig. 4.15 presents the resulting images of these two migration techniques and the proposed modified F-K focusing technique excluding and including the antenna length for the “rectangle” scenario. As was expected, Kirchhoff migration (Fig. 4.15 (c)) is shown to be an efficient technique with respect to F-K migration (Fig. 4.15 (b)), when the respective results are compared to those in Fig. 4.15 (a). Although Kirchhoff migration shows better results, the target shape is not completely defined. Fig. 4.15 (d) shows the image reconstructed by using the modified F-K focusing technique excluding the antenna length. This figure shows an improvement in the target detection, in determining the rectangular shape of the target, and

presents an evident improvement in the image with respect to the F-K and Kirchhoff image reconstructions.

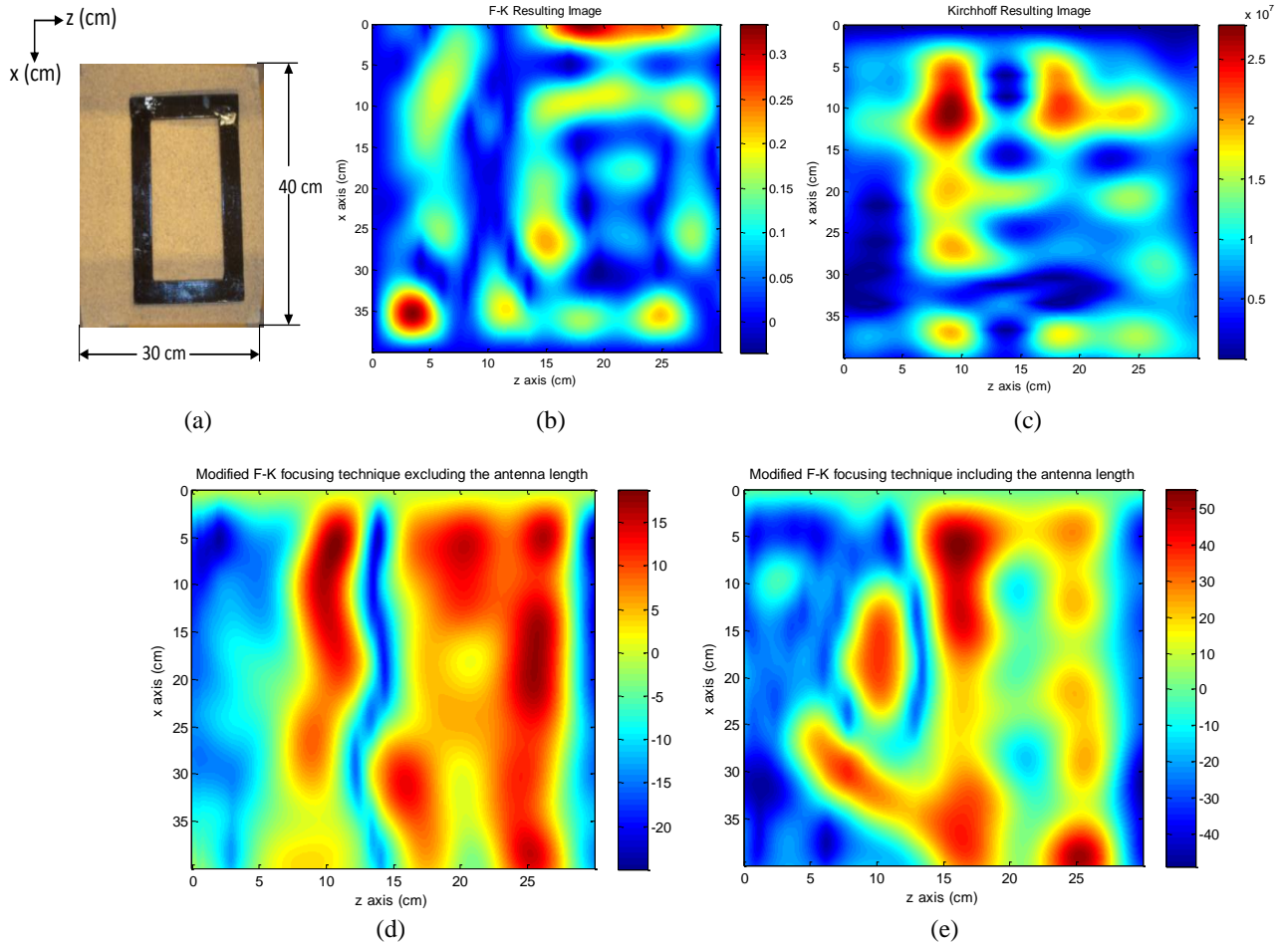


Figure 4.15: (a) Original rectangle object. Rectangle image obtained using (b) F-K migration, (c) Kirchhoff migration, (d) Modified F-K focusing technique excluding the antenna length, (e) Modified F-K focusing technique including the antenna length. Filter value was set with $\Delta M=835$, $M=673$ and $N=837$.

However, although an improvement is shown, the target shape still can be improved. For this purpose, the antenna length was added, and a full distance from the sand up to the VNA-antenna connector was assumed, refocusing the beamforming. After this assumption was taken into account in the proposed technique, Fig. 4.15 (e) was generated. This figure shows a significant

improvement, where the energy is being focused on the target. The filter value ΔM was set at 835, which improved the image target resolution significantly.

Object “Pipe”: In Fig. 4.16, the comparisons of all the different reconstructed pipe images are shown with respect the original picture.

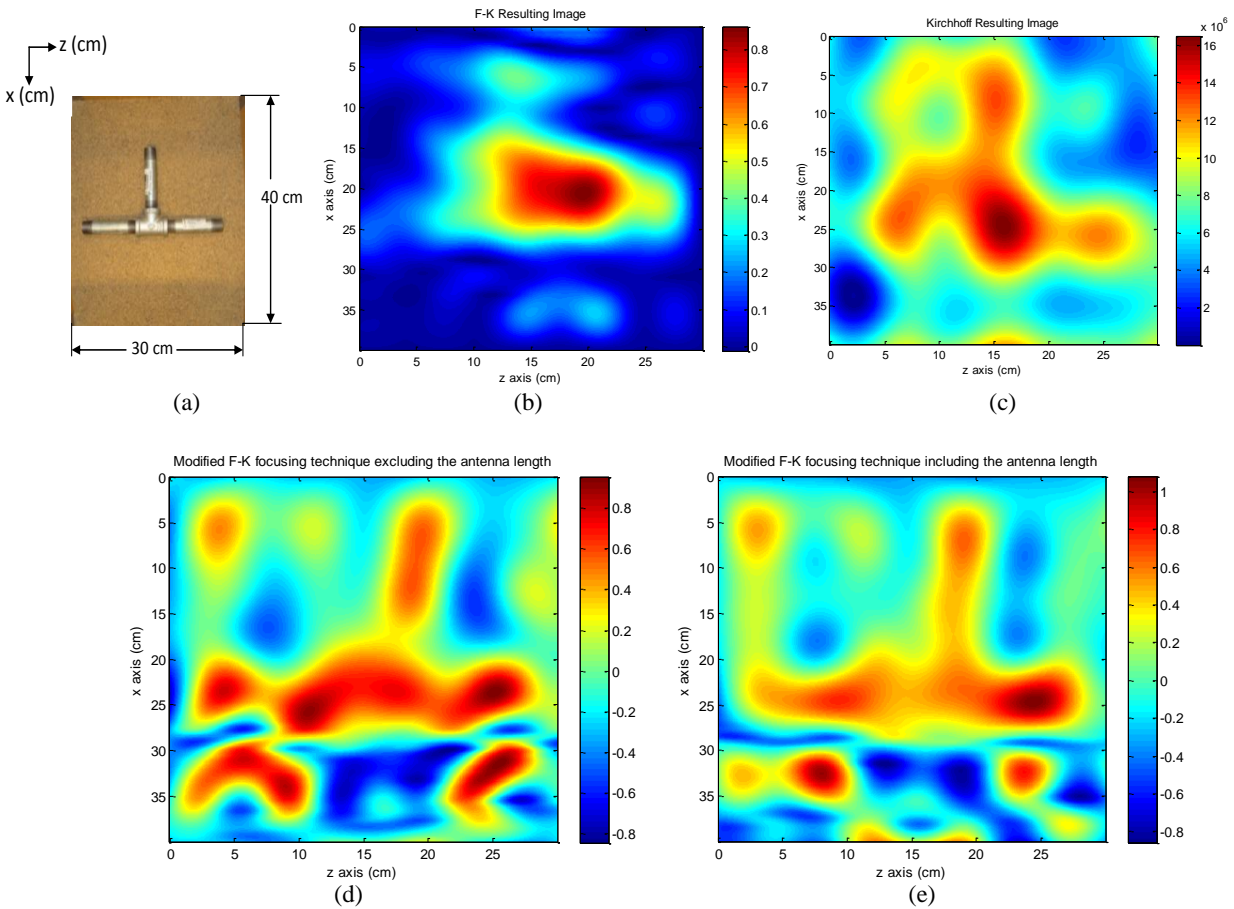


Figure 4.16: (a) Original pipe object. Pipe image obtained using (b) F-K migration, (c) Kirchhoff migration, (d) Modified F-K focusing technique excluding the antenna length, (e) Modified F-K focusing technique including the antenna length. Filter value was set with $\Delta M=450$, $M=673$ and $N=837$.

In Fig. 4.16 (c) it is possible to determine the pipe shape with respect Fig. 4.16 (b), where it is possible to determine only a reflection from the pipe lying along the z axis. In Fig. 4.16 (d), it is possible to see the pipe shape clearly, but some noise around the pipe lying along the z axis is

also evident. This noise can be caused because some of the measurements taken around the pipe can receive some reflections from it and can be interpreted as a strong reflection or due to some aliasing effects during the reconstruction process. Compared to Fig. 4.16 (d), Fig. 4.16 (e) shows an improvement when the distance from the sand up to the VNA-antenna connector is assumed. In Fig. 4.16 (e), the noise is reduced efficiently, and the focus is on the energy reflected from the pipe. The filter value ΔM for this experiment was set at 450.

Object “A”: Fig. 4.17 presents the obtained results for an A shape. This shape was chosen in order to verify the performance of each technique with a complex target shape, where the diagonal shape becomes an important feature to be identified.

In Fig. 4.17 (b), the triangular shape is identified, but the reflected energy is not as strong as that in Fig. 4.17 (c) and Fig. 4.17 (d). Fig. 4.17 (c) shows a strong reflection from the target, but the target features are not clearly visible. In Fig. 4.17 (d), the reflected energy is focused on the target, and the target shape is improved compared to that in Fig. 4.17 (c). This figure reveals a reflection around (25 cm, 35 cm) that could be due to a small peak in the original target. Fig. 4.17 (d) reveals an improvement in the target features when the antenna length is included. Fig. 4.17 (d) shows that the triangular shape of the target is obtained, and the reflection around (25cm, 35cm) is generated by the target peak and is focused closer to the main target shape. The filter value ΔM for this experiment was set at 850.

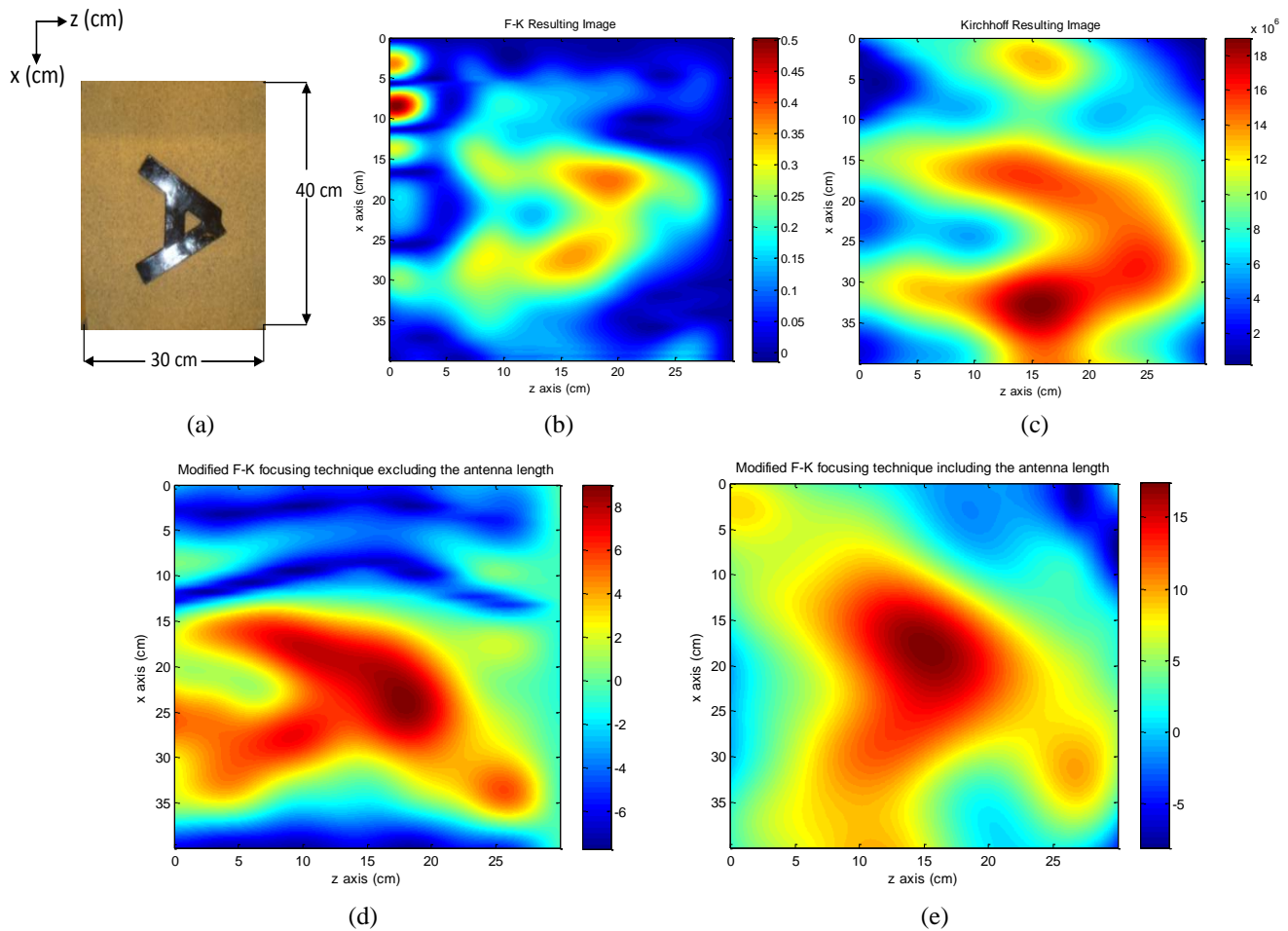


Figure 4.17: (a) Original A object. “A” image obtained using (b) F-K migration, (c) Kirchhoff migration, (d) Modified F-K focusing technique excluding the antenna length, (e) Modified F-K focusing technique including the antenna length. Filter value was set with $\Delta M=850$, $M=673$ and $N=837$.

Object “Bottle” : In Fig. 4.18, the scenario 2 results are shown. As mentioned in section 4.1, fewer measurement points were used than in scenario 1.

For processing purposes, an even number of antenna positions was assumed for each B-scan, and the measurements taken at $(z, 35 \text{ cm})$ locations were omitted, so that the x range in Fig. 4.18(b) to Fig. 4.18 (e) was reduced, from 40 cm to 36 cm.

Although the target used in scenario 2 is not metallic, strong energy is reflected from the target. In Fig. 4.18 (b) and 4.18 (c), the strongest energy is reflected from the bottle body, but the cap does not provide a strong reflection. In Fig. 4.18 (d), it is possible to identify the bottle including

the cap. Thus, this image shows a visible improvement over the previous F-K and Kirchhoff reconstructed images. However, although the bottle is reconstructed, some noise along (20cm, x axis) is visible. As Fig. 4.18 (e) shows, this noise is eliminated after the antenna length is included. In this figure, the image noise or aliasing effects are eliminated, and the energy is focused on the target. The curved shape on the right-side of the bottle is pronounced, but in general, the bottle shape is conserved. The filter value ΔM for this experiment was set at 107.

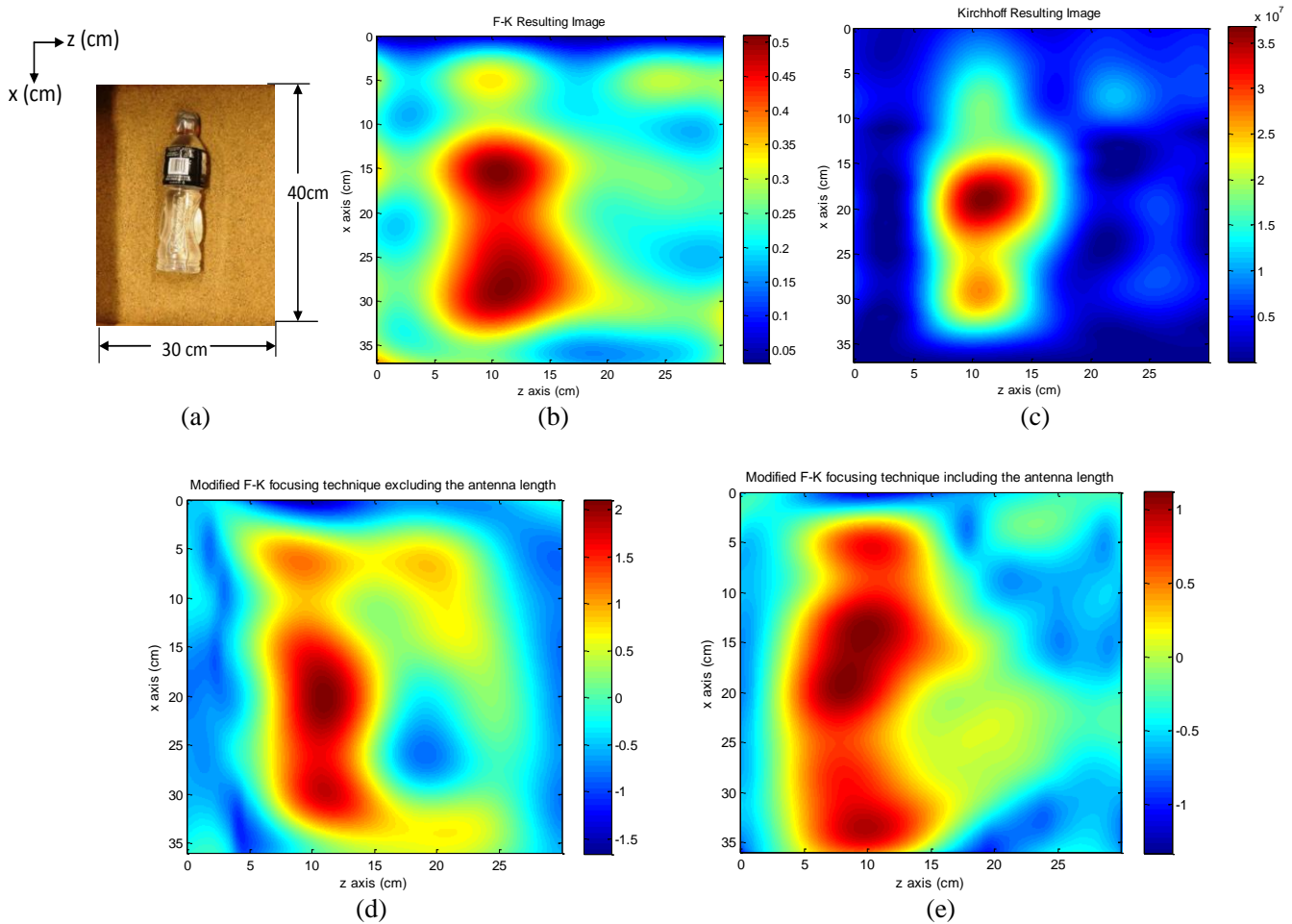


Figure 4.18: (a) Original bottle object. Bottle image obtained using (b) F-K migration, (c) Kirchhoff migration, (d) Modified F-K focusing technique excluding the antenna length, (e) Modified F-K focusing technique including the antenna length. Filter value was set at $\Delta M=550$, $M=406$ and $N=837$.

4.5 Evaluation of the Proposed Technique

As was presented in section 4.3 and 4.4, a subjective analysis in all the reconstructed images can be done by comparing the reconstructed image with respect the original scenario image. In all four different scenarios, it is possible to obtain a better reconstructed image by using the proposed technique. Targets are clearly identified compared to other techniques, which shows a target reconstruction, but the target shape is not clearly visible. The fact of assuming two different distances in our processing allowed us to see that it is possible to obtain an improved image reconstruction when the beamforming is reconstructed further form the target (e.g., including antenna length).

The proposed technique and the migration techniques were run for 100 antenna locations generating a reconstructed image as described in section 3.5. The elapsed times for each technique are shown in the following table:

Table 4.2: Elapsed time per code

Program	Time
F-K	2.4 min
Kirchhoff	1.8 min
MFK	3.45 min

As was expected, the proposed technique increased the elapsed time in approximately one minute due to the focusing and filtering modules.

4.6 Summary

This chapter began by providing a general experiment description, which includes the signal used during the experiments, and the different set-ups implemented for our research. Section 4.2

showed a description of each implemented Matlab function. Section 4.3 presented the filtering effects in our proposed technique followed by section 4.4, where the final reconstructed images, implementing the two common migration techniques (F-K and Kirchhoff) and the proposed technique were shown. In section 4.5 a subjective evaluation of the proposed technique was given according to the presented results in sections 4.2 and 4.3.

Chapter 5

Conclusions and Future Work

Through-wall radar imaging and ground-penetrating radar imaging require efficient techniques to locate and identify targets efficiently. Many experiments have been designed to take undefined and accurate measurements simulating real-life scenarios. In this thesis, the 2-D scanning was done manually, whereas in other studies, the scanning was done by using a 1-D or a 2-D scanning machine. This fact limited the accuracy and number of the measurements in our experiment.

In this thesis, all the measurements were processed by using two common migration techniques and the proposed modified F-K focusing technique excluding and including the antenna length. Migration techniques have been shown to be efficient techniques for GPR purposes, but so far, Kirchhoff migration has provided the best results.

The main interest in this thesis was to improve the performance of an existing migration technique, such as F-K migration, to obtain better results than those from Kirchhoff migration, and to adapt the existing technique from a one-medium environment to a two-media environment application.

The proposed technique, the Modified F-K Focusing technique, was shown to be an efficient technique for improving the reconstructed target image compared to the two existing migration techniques. After we include the antenna length in our processing, the proposed technique

showed an improvement in the target shape and obtained an image similar to the original target. The reconstructed target dimensions were compared subjectively with respect the original target dimensions. When the antenna length was taken into account, the dimensions increased due to the overall image resolution improvement.

The proposed technique showed improvements in the imaging area, but still has several issues that need to be solved in future work. Some suggestions are listed below:

- 1.** It was demonstrated that the proposed technique provides efficient results in target imaging, but the target location is not accurate. Further studies could potentially solve this problem.
- 2.** The proposed technique was developed by using multiple B-scan processing. This work can be extended into a C-scan or 3-D imaging to improve the signal-processing time.
- 3.** More research needs to be done to make the technique real-time.

References

- [1] E.J. Baranoski, “Through-wall imaging: Historical perspective and future directions”, *Journal of the Franklin Institute*, vol 345, pp. 556–569, January 2008.
- [2] M. Farwell, J. Ross, R. Luttrell, D. Cohen, “Sense through the wall system development and design considerations”. *Journal of the Franklin Institute*, vol. 345, pp. 570–591, January 2008.
- [3] L. B. Conyers, *Ground penetrating radar for archaeology*, Altamira Press, 2004.
- [4] The United Nations Children's Fund. “Land-mines: A deadly inheritance”. <http://www.unicef.org/graca/mines.htm>. August 31, 2011
- [5] W. C. Overton, Jr. and D. B. van Hulsteyn. “Superconductor Imaging Surface Magnetometry: Principles And Applications”. *Annual Intemational Conference of the IEEE Engineering in Medicine and Biology Society*, vol. 12, No. 3, 1990.
- [6] Z. H. Adli, M. H. Musa, M. N. K. Arifin. “Electrical Resistivity Of Subsurface: Field And Laboratory Assessment”. *World Academy of Science, Engineering and Technology*, vol 69, 2010.
- [7] W. Yang, C. T. Verdi, J. Hou and Z. Zhang, “1D Subsurface electromagnetic fields excited by energized steel casing”. *Geophysics*, Vol. 74, No.4. pp.E159-E180, July-August 2009.
- [8] M. G. Eraslan, A. N. Vamivakas, S. B. Ippolito, M. S. Unlu, and B. B. Goldberg. “High Resolution Subsurface Thermal Imaging Using A Numerical Aperture Increasing Lens”. *Quantum Electronics and Laser Science Conference (QELS)*, 2005.
- [9] D. J. Daniels, D. J. Gunton, H. F. Scott. “Introduction To Subsurface Radar”. *IEE proceedings*, vol. 135, No. 4, August 1988.
- [10] E. Yigit, S. Demirci and C. Ozdemir. “Ground Penetrating Radar Image Focusing using Frequency-Wavenumber based Synthetic Aperture Radar Technique”. *Electromagnetics in Advanced Applications. International Conference on*, pp 344-347, 2007.
- [11] D. D. Ferris, Jr. and N. C. Currie, “A survey of current technologies for through-the-wall surveillance (TWS),” *SPIE Conference on Sensors*, vol. 3577, pp 62-72. Boston, MA, November. 1998.
- [12] J. Callerame. “x-ray backscatter imaging: Photography through barriers”. *JCPDS-International Centre for Diffraction Data*, vol. 21, 2006.
- [13] G. Wang and M. G. Amin. “Imaging Through Unknown Walls Using Different Standoff Distances”. *IEEE transactions on signal processing*, vol. 54, no. 10, October 2006.

- [14] M. I. Skolnik, *Radar Handbook*, McGraw-Hill Professional, 3 edition, 2008.
- [15] J. D. Woll. “Monopulse Doppler radar for vehicle applications”. *Intelligent Vehicles' 95 Symposium, proceedings of the*, pp. 42-47, 1995
- [16] P. Berens. “Introduction to Synthetic Aperture Radar (SAR)”. In *Advanced Radar Systems, Signal and Data Processing*, paper 3, pp. 3-1 – 3-16. Neuilly-sur-Seine, France, 2007
- [17] O. Sisma, A. Gaugue, C. Liebe, J. M. Ogier. “UWB Radar: Vision through a wall”. *Personal Wireless Communications, IFIP International Federation for Information Processing*, vol. 245, pp.241-251. Springer, 2007.
- [18] L.E Miller, “Why UWB? a review of ultrawideband technology”, *National Institute of Standards and Technology*, 2003.
- [19] B. D. V. Veen and K. Buckley, “Beamforming: A Versatile Approach to Spatial Filtering”, *IEEE ASSP Magazine*, pp.4-24, April 1988.
- [20] R.H. Stolt and A.K. Benson, *Seismic Migration: Theory and Practice*, Geophysical press, Vol. 5, P.P. 87-88, 1986.
- [21] E. A. Avallone, P. Barry, G. S. Bonn and W. G. Bowman, *McGraw-Hill Dictionary of Scientific and Technical Terms*, The McGraw-Hill Companies, Inc, 6th edition, 2002.
- [22] J. Zheng, *Optical frequency-modulated continuous wave (FMCW) interferometry*, Springer Verlag, 2005.
- [23] Agilent Technologies, *Network Analyzer Basics*, August 31, 2004.
- [24] Agilent Technologies, *Understanding the Fundamental Principles of Vector Network a analysis*, Application Note 1287-1
- [25] MI. Skolnik, *Radar Handbook*, McGraw Hill Press, pp. 21.30, 2008.
- [26] S. Muhammad, *Computer-aided intelligent recognition techniques and applications*, John Wiley and Sons, pp. 321, 2005
- [27] R. H. Stolt, “Migration by Fourier Transform”, *Geophysics*, Vol. 43, 1978.
- [28] C. G. Gilmore, *A Comparison of Imaging Methods using GPR for Landmine Detection And A Preliminary Investigation into the SEM for Identification of Buried Objects*, MSc. Dissertation, University of Manitoba, Winnipeg, Manitoba, Canada, December 2004.

- [29] J. H. Chun and C. A. Jacewitz, “*Fundamentals of frequency domain migration*”, *Geophysics*, Vol. 46, no. 5, P.P. 717-733, may 1981.
- [30] O. Yilmaz, *Seismic Data Analysis: Processing, Inversion and Interpretation of Seismic Data*, Society of Exploration Geophysicists, Vol. 1, 2001.
- [31] W. A. Schneider, “Integral formulation for migration in two and three dimensions,” *Geophysics*, vol. 43, no. 1, pp. 49–76, Feb. 1978.
- [32] N.T. Thành , L. V. Kempen , T.G. Savelyev , X. Zhuge , M. Aftanas , E. Zaikov , M. Drutarovský, H. Sahli. “Comparison of Basic Inversion Techniques for Through-Wall Imaging Using UWB Radar”. *IEEE Radar Conference*, pp. 140-143, 2008.
- [33] X.Zhuge, T.G. Savelyev, A.G. Yarovoy, and L.P. Ligthart, “UWB Array-Based Radar Imaging Using Modified Kirchhoff Migration”. *Proceedings Of The 2008 IEEE International Conference On Ultra-Wideband*, Vol. 3, 2008.
- [34] M. Aftanas. *Through Wall Imaging With UWB Radar System*, Ph.D. dissertation, Technical University Of Košice, Faculty of Electrical Engineering and Informatics, Slovakia, August 2009.
- [35] J. A. Scales, *Theory of Seismic Imaging*, P.P. 101-108, Springer-Verlag, 1995.
- [36] E. Yigit, S. Demirci, C. Ozdemir and A. Kavak, “A synthetic aperture radar-based focusing algorithm for B-scan ground penetrating radar imagery”, *Microwave and Optical Technology Letters*, V. 49, P.P. 2534-2540, 2007.
- [37] G. Garza, J.X. Lopez and Z. Qiao, “Cross-Range Imaging of Synthetic Aperture Radar Data”, *Pacific Journal of Applied Mathematics*, V. 2, P.P. 65-81, 2009.
- [38] E. M. Johansson and J. E. Mast, “Three-dimensional ground penetrating radar imaging using synthetic aperture time-domain focusing”, *SPIE* Vol. 2275/205. 1994.
- [39] D. C. Swanson, *Signal processing for intelligent sensor systems*, Marcel Dekker, Inc., New York, 2000.
- [40] G. F. Margrave, *Numerical Methods of Exploration Seismology with algorithms in MATLAB*, Department of Geology and Geophysics, University of Calgary, July 11, 2003.
- [41] O. Yilmaz, *Seismic data analysis processing, inversion and interpretation of seismic data*, Society of exploration geophysics, Volume I, 2001.
- [42] R.C. González and R. E. Woods, *Digital image processing*, 3rd Edition, Prentice Hall, 2008.

- [43] X.M.Qing and Z.N. Chen, “Antipodal Vivaldi antenna for UWB applications”, in Proc. Euro Electromag.-UWB SP7, Magdeburg, Germany, July 12–16, 2004.
- [44] X. Zhuge, T.G. Savelyev, A. G. Yarovoy, L. P. Ligthart and B. Levitas, “Comparison of Different Migration Techniques for UWB short-range Imaging”, European radar conference, P.P. 184-187, 2009.

Appendix A- Matlab Codes

This appendix includes the developed codes shown in table 4.1. Some functions such as `delayandsumGPR` are implicit functions that were implemented inside existing codes. In the case of `delayandsumGPR`, it was implemented inside the F-K code, focusing the collected data at each B-scan antenna location. Each developed function is explained through this appendix.

A.1 Main Function

This main function calls all the focused and windowed B-scans using the `fk1` to `fk10` functions and generates the sectional image at certain depth `p`, as explained in section 3.5. The sectional image is then filtered generating the final output image.

```
%This program calls the F-K migration code and generates 10 different B-scans
% along the grid. This image is filtered generating the final
% reconstructed image. This code was developed by Jorge Morales and
% optimized by Jorge Morales and Rajagopalan Ramaswamy.

[S1 S]=call_b_scan_data(1); %complex expression collected B-scan data 1
[d1]=fk(S); % migrated B-scan data 1
[S1 S]=call_b_scan_data(2); % complex expression collected B-scan data 2
[d2]=fk(S); % migrated B-scan data 2
[S1 S]=call_b_scan_data(3); % complex expression collected B-scan data 3
[d3]=fk(S); % migrated B-scan data 3
[S1 S]=call_b_scan_data(4); % complex expression collected B-scan data 4
[d4]=fk(S); % migrated B-scan data 4
[S1 S]=call_b_scan_data(5); % complex expression collected B-scan data 5
[d5]=fk(S); % migrated B-scan data 5
[S1 S]=call_b_scan_data(6); % complex expression collected B-scan data 6
[d6]=fk(S); % migrated B-scan data 6
[S1 S]=call_b_scan_data(7); % complex expression collected B-scan data 7
[d7]=fk(S); % migrated B-scan data 7
[S1 S]=call_b_scan_data(8); % complex expression collected B-scan data 8
[d8]=fk(S); % migrated B-scan data 8
[S1 S]=call_b_scan_data(9); % complex expression collected B-scan data 9
[d9]=fk(S); % migrated B-scan data 9
[S1 S]=call_b_scan_data(10); %complex expression collected B-scan data 10
[d10]=fk(S); % migrated B-scan data 10
p=98; %desired depth y
```

```

mat=[transpose(d10(p,:)) transpose(d9(p,:)) transpose(d8(p,:))
transpose(d7(p,:)) transpose(d6(p,:)) transpose(d5(p,:)) transpose(d4(p,:))
transpose(d3(p,:)) transpose(d2(p,:)) transpose(d1(p,:))];
mat2=abs(abs(mat));
[N M]=size(mat2);
for kl=1:N
    new(kl,:)=resample(mat2(kl,:),673,10);
end
[N1 M1]=size(new);
for kl=1:M1
    new3(:,kl)=resample(new(:,kl),673,74);
end
new2=(new3);
[N2 M2]=size(new2);
for kl=1:M1
    new4(:,kl)=new2(:,674-kl);
end
[N2 M2]=size(new4);
for kl=1:N2
    new5(kl,:)=new4(838-kl,:);
end

[j1 k1]=size(new3);
wide=40;
width=30;
ancho=width/j1;
largo=wide/k1;
temp3=0;
temp4=0;
ancho2(1)=0;
largo2(1)=0;
for hk=2:1:j1
    ancho2(hk)=temp3+ancho;
    temp3=ancho2(hk);
end
for hk=2:1:k1
    largo2(hk)=temp4+largo;
    temp4=largo2(hk);
end

    for kk=35:613                                %x axis
        for uu=13:645                             %y axis
            leim6(uu-12, kk-34)=new5(uu, kk);
        end
    end

figure(1);
colormap((jet));
imagesc(ancho2,largo2,leim6);
title('Pipe image before filtering including antenna length');
ylabel('x axis (cm)');
xlabel('z axis (cm)');

%Filtering process
[N M] = size(new5);

```

```

deltam=450; %Filter scaling factor value

F_x_u2 = fft2(new5);
for i=1:N
    for j=1:M
        out1(i,j)=sqrt((j/(M-(deltam)))^2+(i/(N-(deltam)))^2)*F_x_u2(i,j);
    end
end
a1=ifft2(out1);
final=(real(a1));
%Reconstructed image generation

for kk=35:613
    for uu=13:645
        leim2(uu-12, kk-34)=final(uu, kk);
    end
end
figure(3);
sec_img=leim2;
colormap((jet));
imagesc(ancho2, largo2, (sec_img));
title('Modified F-K focusing technique including the antenna length');
ylabel('x axis (cm)');
xlabel('z axis (cm)');

```

A.2 delayandsumGPR

This function is used as the focusing module explained in chapter 3. This function takes as an input *magn* which is the magnitude of our collected data, *freqvec* which is the frequency vector defined between f_{min} and f_{max} , *xapos* is the antenna location with respect the x axis, *yapos* is the antenna distance from the sand, *zapos* is the antenna location with respect the z axis and *pha* is phase of the collected data. It returns *y* which is the focused data at each antenna position with respect a assumed target position (*Xtargetpos*, *Ytargetpos*, *Ztargetpos*).

```

function [y]=delayandsumGPR(magn, freqvec, xapos, yapos, zapos, pha)
numtxrx=1; %Number of antennas
numtargets=5; %number of targets
minvalfreq=1e9; %Minimum frequency
value
maxvalfreq=10e9; %Maximum frequency
value
dfreq=(freqvec(2)-freqvec(1)); %frequency step size
fvec=freqvec; %Frequency vector

```

```

freqsize=size(fvec,2); %Frequency vector
size
Xtargetpos=[0.18 0.18 0.18 0.252 0.288];
Ytargetpos=[0.06 0.06 0.06 0.06 0.06];
Ztargetpos=[0.224 0.056 0.14 0.14 0.14];
Xantenapos=xapos; %X antenna position in cm
Zantenapos=zapos;
Yantenapos=yapos;

y=zeros(numtxrx,freqsize);

for n=1:numtxrx
    for m=1:freqsize
        for P=1:numtargets

td=tdelayGPR(Xantenapos,Yantenapos,Zantenapos,Xtargetpos(P),Ztargetpos(P),Ytargetpos(P),numtargets);
            y(n,m)= y(n,m)+(magn(m)*exp(-j*(2*pi*fvec(m)*td+pha(m))));
%tdelay1 is the time delay between each antenna position and target position
        end
    end
end
end

```

A.3 tdelay

This function calculates the respective time delay between an specific antenna location and a possible target position. This function takes as an input X_r , Y_r , and Z_r , which are the antenna location with respect x, y and z axis, respectively. $TargX$, $TargZ$ and $TargY$ are the possible target location with respect x, z and y axis respectively. The *numtarg* input variable refers to the assumed number of targets. It returns *timedelay* which is the one way time delay from the antenna to the target.

```

function [timedelay]=tdelay(Xr,Yr,Zr,TargX,TargZ,TargY,numtarg)

targnum=numtarg;
Xi=TargX; %x target position
Zi=TargZ;
Yi=TargY ; %y target position
Xtm=Xr; %x receiver position
Ztm2=Zr;
Ztm=Yr ; %Y receiver position from the wall
d=0.5; % wall tickness
% Ami=100; % theta m,i angle
E1=1;

```

```

E2=3.5;      %dielectric constant
iter=0;
qq9=0;
rmiair1=0;
c=3e8;      %SPEED OF PROPAGATION IN THE AIR
v=c/sqrt(E2); %SPEED OF PROPAGATION IN THE media
aa=abs(Xi-Xtm);
bb=abs(Ztm)+Yi;
b2=abs(Xi-Xtm);
a2=abs(Ztm)+Yi;
angle=(atan(a2/b2))*180/pi;
b3=Ztm/(tand(angle)); %find the distance to x1
if (Xtm<=Xi)
    X1=Xtm+b3;
else
    X1=Xtm-b3;
end
xb=Xi+sqrt(E1/E2)*(X1-Xi);
if(Xtm<=xb)
    b4=Xtm+xb;
else
    b4=Xtm-xb;
end
angle2=(atan(Ztm/b4))*180/pi;
rmiair1=Ztm/sind(angle2);
alpha=90-angle2;
alpha2=asind(E1*(sind(alpha)/E2));
qq9=Yi/cosd(alpha2);
timedelay=(rmiair1)/c+((qq9)/v);

```

A.4 call_b_scan_data

This function takes as an input the B-scan (*val1*) to be processed. It calls the collected data along that B-scan and returns the collected data as a matrix *S1* and the focused data as *aga1*

```

function [S1 aga1]=call_b_scan_data(val1)

bscan=val1;

if bscan==1
    for ant=1:10
        [c1 dataini1 aga1]=bscan_data(bscan,ant);
        S1(:,ant)=c1;
        S2(:,ant)=dataini1;
        S(:,ant)=aga1;
    end
elseif bscan==2
    for ant=11:20
        [c1 dataini1 aga1]=bscan_data(bscan,ant);

```

```

        S1(:,ant-10)=c1;
        S2(:,ant-10)=datainil;
        S(:,ant-10)=agal;

    end
elseif bscan==3
    for ant=21:30
        [c1 datainil agal]=bscan_data(bscan,ant);
        S1(:,ant-20)=c1;
        S2(:,ant-20)=datainil;
        S(:,ant-20)=agal;
    end
elseif bscan==4
    for ant=31:40
        [c1 datainil agal]=bscan_data(bscan,ant);
        S1(:,ant-30)=c1;
        S2(:,ant-30)=datainil;
        S(:,ant-30)=agal;

    end
elseif bscan==5
    for ant=41:50
        [c1 datainil agal]=bscan_data(bscan,ant);
        S1(:,ant-40)=c1;
        S2(:,ant-40)=datainil;
        S(:,ant-40)=agal;

    end
elseif bscan==6
    for ant=51:60
        [c1 datainil agal]=bscan_data(bscan,ant);
        S1(:,ant-50)=c1;
        S2(:,ant-50)=datainil;
        S(:,ant-50)=agal;

    end

elseif bscan==7
    for ant=61:70
        [c1 datainil agal]=bscan_data(bscan,ant);
        S1(:,ant-60)=c1;
        S2(:,ant-60)=datainil;
        S(:,ant-60)=agal;

    end
elseif bscan==8
    for ant=71:80
        [c1 datainil agal]=bscan_data(bscan,ant);
        S1(:,ant-70)=c1;
        S2(:,ant-70)=datainil;
        S(:,ant-70)=agal;

    end
end

```

```

elseif bscan==9
    for ant=81:90
        [c1 dataini1 aga1]=bscan_data(bscan,ant);
        S1(:,ant-80)=c1;
        S2(:,ant-80)=dataini1;
        S(:,ant-80)=aga1;
    end
elseif bscan==10
    for ant=91:100
        [c1 dataini1 aga1]=bscan_data(bscan,ant);
        S1(:,ant-90)=c1;
        S2(:,ant-90)=dataini1;
    end
else
    disp('selected B-scan out of range');
end

```

A.5 bscan_data

This function takes as a input the b-scan number *b-scan* and the antenna location number *ant*. It returns the complex expression of the data with target *c1* and the data without target *dataini1* and returns the focused data *aga1* to be windowed and migrated using F-K migration.

```

function [c1 dataini1 aga1]=bscan_data(bscan,ant)
load('L:\matlab (september 16-2011)\measurements pipe\fulldata.mat');
load('L:\matlab (july 28-2011)\Measurements_square_excel_files\notarget\fulldatanotarget.mat');
in1=fulldatanotarget(:,4,ant);
in2=fulldatanotarget(:,5,ant);
in3=fulldata(:,4,ant);
in4=fulldata(:,5,ant);
freqvec=fulldata(:,1,1);
freqvec=freqvec';
deltax=0.036; %antenna spacing along the x axis
deltaz=0.036; %antenna spacing along the z axis
xapos=deltax*bscan;
zapos=deltaz*bscan;
yapos=0.35;
for kk=1:901
    dat1(kk)=10.^(in1(kk)/10)*exp(j*in2(kk)*(pi/180));
    dat2(kk)=10.^(in3(kk)/10)*exp(j*in4(kk)*(pi/180));
end
for kk=1:901
    ret1(kk)=(1/2)*(dat1(kk)+conj(dat1(kk)));
    imt1(kk)=(1/(2*j))*(dat1(kk)-conj(dat1(kk)));
    ret2(kk)=(1/2)*(dat2(kk)+conj(dat2(kk)));
    imt2(kk)=(1/(2*j))*(dat2(kk)-conj(dat2(kk)));
end

```



```

comp1=ret1+(imt1*j);
comp2=ret2+(imt2*j);
c1=transpose(comp2);           %DATA WITH TARGET
dataini1=transpose(comp1); %DATA WITHOUT TARGET
temp1=transpose(phase(comp2)); %DATA phase
magg1=sqrt(real(c1).^2+imag(c1).^2);
aga1=delayandsumGPR(magg1,freqvec,xapos,yapos,zapos,temp1);
aga1=aga1';

```

A.6 Kirch_im_gen

This function is the main function which calls all the B-scans using the *call_b_scan_data* function and processes them using the *kirchhoffmigration* function and generates the image at certain depth *p*.

```

function see_img=kirch_im_gen()
clear all;
close all;
tic
[S1]=call_b_scan_data(1);
[k1]=kirchhoffmigration(S1);
[S2]=call_b_scan_data(2);
[k2]=kirchhoffmigration(S2);
[S3]=call_b_scan_data(3);
[k3]=kirchhoffmigration(S3);
[S4]=call_b_scan_data(4);
[k4]=kirchhoffmigration(S4);
[S5]=call_b_scan_data(5);
[k5]=kirchhoffmigration(S5);
[S6]=call_b_scan_data(6);
[k6]=kirchhoffmigration(S6);
[S7]=call_b_scan_data(7);
[k7]=kirchhoffmigration(S7);
[S8]=call_b_scan_data(8);
[k8]=kirchhoffmigration(S8);
[S9]=call_b_scan_data(9);
[k9]=kirchhoffmigration(S9);
[S10]=call_b_scan_data(10);
[k10 y11]=kirchhoffmigration(S10);

p=290; %183
mat=[transpose(k10(p,:)) transpose(k9(p,:)) transpose(k8(p,:))
transpose(k7(p,:)) transpose(k6(p,:)) transpose(k5(p,:)) transpose(k4(p,:))
transpose(k3(p,:)) transpose(k2(p,:)) transpose(k1(p,:))];
mat2=abs(abs(mat));
[N M]=size(mat2);
for kl=1:N
    new(kl,:)=resample(mat2(kl,:),673,10);
end

```

```

[N2 M2]=size(new);
for kl=1:N2
    new4(kl,:)=new(601-kl,:);
end
%
for kk=40:560                                     %x axis
    for uu=100:415                                 %y axis
        leim(uu-99, kk-39)=new4(uu, kk);
    end
end

[N2 M2]=size(leim);
for kl=1:M2
    leim2(:,kl)=leim(:,522-kl);
end
[j1 kk20]=size(leim2);
    wide=40;
width=30;
ancho=width/j1;
largo=wide/kk20;
temp3=0;
temp4=0;
ancho2(1)=0;
largo2(1)=0;
for hk=2:1:j1
    ancho2(hk)=temp3+ancho;
    temp3=ancho2(hk);
end
for hk=2:1:kk20
    largo2(hk)=temp4+largo;
    temp4=largo2(hk);
end

figure(1);
    colormap((jet));
see_img=(abs(abs(leim2)));
imagesc(ancho2,largo2, see_img);
ylabel('x axis (cm)');
xlabel('z axis (cm)');
title('Kirchhoff Resulting Image');
toc

```